Highly charged ions as a tool for fundamental physics and tests of the Standard Model

Von der Fakultät für Mathematik und Physik
der Gottfried Wilhelm Leibniz Universität Hannover

zur Erlangung des akademischen Grades
Doktor der Naturwissenschaften
Dr. rer. nat.

genehmigte Dissertation von

M.Sc. Jan Richter

2026

Referentin:	Prof. Dr. Elina Fuchs
Korreferent:	Prof. Dr. Andrey Surzhykov
Korreferent:	Prof. Dr. Dmitry Budker

Tag der Promotion: 10.12.2025

ABSTRACT

For decades, highly charged ions (HCIs) have been the focus of extensive research because of their importance for plasma and astrophysics, tests of quantum electrodynamics, searches of new physics, and many other applications. This theoretical thesis investigates the potential of HCI spectroscopy for fundamental physics across different experimental scenarios. These range from precision spectroscopy of ions in Paul traps, to the interaction of synchrotron radiation with ions confined in electron beam ion traps (EBITs), up to the spectroscopy of HCIs stored in the Large Hadron Collider at CERN. In particular, a King plot analysis is performed, including isotope shift data from highly charged Ca^{14+}. This analysis provides insights into nuclear polarization effects on the electronic structure of ions and yields constraints on the coupling of a hypothetical new boson to neutrons and electrons. Moreover, the prospects of using the magnetic field in an EBIT to determine lifetimes of excited states in HCIs via the Hanle effect are investigated. Such data are especially valuable for diagnostics of laboratory and astrophysical plasmas. Finally, the spectroscopy of HCIs stored at the Large Hadron Collider is explored within the framework of the Gamma Factory project, which offers a wide range of applications in atomic, nuclear, and particle physics. This thesis analyzes the case where a magnetic field is applied in the collision zone, resulting in strong fields in the rest frame of the ion. Such fields are particularly important for future studies, for instance, in atomic parity violation and for measurements of polarizabilities in HCIs. The impact of these fields on the scattering process offers additional applications for the Gamma Factory project, such as resonance condition tuning, beam cooling and polarization control.

Keywords: Highly charged ions, Isotope shifts, Resonant photon scattering

ZUSAMMENFASSUNG

Hochgeladene Ionen stehen seit Jahrzehnten im Fokus intensiver Forschung, unter anderem aufgrund ihrer essentiellen Bedeutung für Plasma- und Astrophysik als auch für Tests der Quantenelektrodynamik und für die Suche nach neuer Physik. Diese theoretische Arbeit untersucht das Potenzial von Spektroskopie hochgeladener Ionen für Fragestellungen der fundamentalen Physik in verschiedenen experimentellen Szenarien. Diese reichen von Präzisionsspektroskopie von optischen Übergängen in Ionen über die Wechselwirkung von Synchrotronstrahlung mit in einer Electron Beam Ion Trap (EBIT) gespeicherten Ionen bis hin zur Spektroskopie hochgeladener Ionen im Large Hadron Collider am CERN. Im Rahmen der Arbeit wird eine King-Plot-Analyse von Isotopenverschiebungen in einfach geladenen Ca^{+}- und hochgeladenen Ca^{14+}-Ionen durchgeführt. Diese Analyse ermöglicht Einblicke in Kernpolarisationseffekte auf die elektronische Struktur der Ionen und erlaubt es, die mögliche Kopplung eines hypothetischen neuen Bosons an Neutronen und Elektronen einzuschränken. Im zweiten Abschnitt dieser Arbeit wird der Einfluss von externen elektrischen und magnetischen Feldern auf die resonante Streuung von Photonen an hochgeladenen Ionen untersucht. Insbesondere wird die Möglichkeit untersucht, das Magnetfeld in einer EBIT zur Bestimmung von Lebensdauern angeregter Zustände in hochgeladenen Ionen über den Hanle-Effekt zu nutzen. Solche Daten sind essentiell für die Diagnostik von Labor- und astrophysikalischen Plasmen. Schließlich wird die Spektroskopie hochgeladener Ionen im Large Hadron Collider im Rahmen des Gamma-Factory-Projekts betrachtet. Diese Arbeit beschäftigt sich mit dem Szenario, in dem die Ionen einem Magnetfeld im Kollisionsbereich ausgesetzt werden. Durch die relativistischen Geschwindigkeiten der Ionen führt dies zu starken magnetischen und elektrischen Feldern im Ruhesystem des Ions. Die Auswirkungen dieser Felder auf den Streuprozess eröffnen Anwendungsmöglichkeiten im Kontext der Gamma Factory, beispielsweise zur Feinjustierung der Resonanzbedingung, zur Kühlung des Ionenstrahls sowie zur Kontrolle der Polarisation der gestreuten Photonen.

Schlagwörter: Hochgeladene Ionen, Isotopenverschiebung, Resonante Photonenstreuung

CONTENTS

1

INTRODUCTION

The starting point in the history of highly charged ions dates back to the 19th century, when spectral lines from the solar corona were observed that did not match the spectra of any known element. However, it was only much later in the 20th century that the source of these mysterious lines was correctly identified as highly charged ions [1–3]. Since then, highly charged ions have been in the focus of numerous studies to understand their structure and dynamics, which is crucial for the interpretation of astrophysical observations as well as for several applications like ion-based atomic clocks, lithography or plasma diagnostics in nuclear fusion research [4–8]. Moreover, highly charged ions have also emerged as promising systems for testing the Standard Model. For example, they enable studies of quantum electrodynamics in strong electric fields and serve as sensitive probes for variations of fundamental constants [9,10]. This thesis investigates the potential of highly charged ion spectroscopy for fundamental physics across different experimental scenarios, ranging from precision spectroscopy of optical transitions, to the interaction of synchrotron radiation with ions confined in electron beam ion traps, up to the spectroscopy of highly charged ions stored in the Large Hadron Collider at CERN.

This introductory chapter begins with general remarks about highly charged ions and their basic properties. Afterwards, we briefly review the Standard Model of particle physics, its most famous limitations and some proposed extensions. Finally, we provide an overview of different experimental approaches within atomic, molecular and optical physics that aim to search for or constrain physics beyond the Standard Model. The main part of this thesis is divided into two chapters. First, we focus on the topic of isotope shifts and the so-called King plot analysis, which allows us to use experimental isotope shift data to probe possible couplings of a hypothetical new boson to neutrons and electrons. In particular, we perform a theoretical analysis of new isotope shift data in singly charged and highly charged calcium ions, leading to the most stringent King-plot-based bounds on new physics to date. While the first part focuses on ion spectroscopy in the optical regime, the second main chapter will explore the interaction of highly charged ions with x-ray photons. We investigate the process of resonant photon scattering by highly charged ions, with a particular emphasis on the influence of static external electric and magnetic fields. In this context, we consider two experimental scenarios. First, we focus on scattering experiments with highly charged ions confined in electron beam ion traps and discuss how the magnetic field of the ion trap can be used to determine lifetimes of excited ionic states. Such data are particularly important for diagnostics of both astrophysical and laboratory plasmas. Second, we turn to the novel proposal of the Gamma Factory project at CERN. The aim of this proposal is to use the process of resonant photon scattering by ultra-relativistic beams of highly charged ions to generate high intensity γ-rays [11]. This facility could offer promising applications in atomic and nuclear physics and would provide a tool for various tests of the Standard Model or searches for physics beyond it [12–15]. We show that applying static external fields in the collision zone of photons and ions offers different applications for the Gamma Factory setup like resonance condition tuning, beam cooling and polarization control. Finally, in Chapter 4, we summarize the main results of this thesis and provide a brief outlook for future studies.

Throughout this thesis, relativistic units ($\hbar = c = m_e = 1$) and the Heaviside charge unit ($\alpha = e^2/4\pi$, $e < 0$) are used unless stated otherwise. Here, α denotes the fine structure constant.

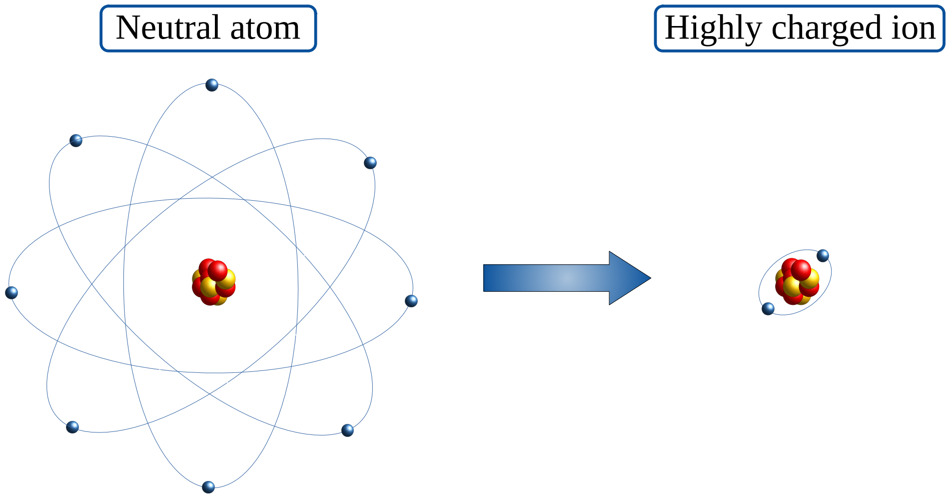

Figure 1.1: Highly charged ions are atomic systems with multiple electrons stripped away. The remaining electrons experience a very strong electric field and are closely bound, leading to a large overlap of the electronic wave functions with the nucleus.

1.1 HIGHLY CHARGED IONS

Highly charged ions (HCIs) are atomic systems in which multiple electrons have been stripped away, leaving behind a positively charged core with only a few bound electrons or, in the extreme case of hydrogen-like ions, just one single electron, see Fig. 1.1. Such ions naturally occur in hot and dense astrophysical plasmas, whose diagnostics rely on the rich spectroscopic data from x-ray observatories like Chandra, XMM-Newton and XRISM. Interpreting these complex spectra requires a detailed understanding of the structure and dynamics of HCIs [1,4,16–18]. Therefore, precise laboratory data are essential to support and improve theoretical models. There are different methods available to generate HCIs for experiments. One option is the electron cyclotron resonance ion source (ECRIS), in which electrons in a magnetically confined plasma are heated by microwave radiation and highly charged ions are produced due to electron impact ionization. Another option to achieve very high charge states is to accelerate singly charged or moderately charged ions in storage rings and collide them with thin stripping foils to remove more electrons. An opposite approach is used in electron beam ion traps (EBITs), where, instead of accelerating ions to high energies, the ions remain almost at rest in the laboratory frame, while they get hit by highly energetic electron beams. It is possible to directly study HCIs

Transition energy $\Delta E_{n\to n'}$	$\propto Z^2$
Fine structure splitting $\Delta E_{p_{1/2}-p_{3/2}}$	$\propto Z^4$
Bohr radius a_0	$\propto Z^{-1}$
Electric field strength $\langle\mathcal{E}\rangle$	$\propto Z^3$

Table 1.1: The approximate Z-scalings in H-like ions for the transition energy between states with different principal quantum number n, the fine structure splitting between $p_{1/2}$ and $p_{3/2}$ states, the Bohr radius a_0, and the expectation value of the electric field strength experienced by an electron in the ground state $\langle\mathcal{E}\rangle$.

in a storage ring or trapped in an EBIT. However, for high precision measurements, such as g-factor determinations or spectroscopy for ion clocks, the ions can be decelerated, cooled and transferred to a Paul or Penning trap, where the ions can be confined under highly controlled conditions [1, 4, 19–23]. In this thesis, we explore HCI spectroscopy across different of these experimental setups, including precision spectroscopy of ions in Paul traps as well as the interaction of x-ray photons with HCIs confined in an EBIT or stored in the Large Hadron Collider.

Laboratory studies of HCIs are not only essential for the analysis of astrophysical data, but also offer valuable applications for fundamental physics. To highlight this potential, it is helpful to discuss some general properties of HCIs in the following, see Tab. 1.1. One characteristic of HCIs is their much smaller spatial extent compared to neutral atoms. The remaining bound electrons in an HCI are very closely bound to the nucleus. While the Bohr radius for a neutral hydrogen atom is $a_0^{(Z=1)} \approx 5 \times 10^{-11}$ m, the Z-scaling of hydrogen-like systems reduces the analogous radius to $a_0^{(Z=92)} \approx 5 \times 10^{-13}$ m for hydrogen-like uranium [4], as shown in the left panel of Fig. 1.2. Moreover, in the extreme case of hydrogen-like ions, the bound electron experiences the full unscreened Coulomb potential of the nucleus. This results in an approximate Z^3-scaling of the electric field strength at the electron's position. Consequently, the bound electrons in heavy highly charged ions are exposed to extremely strong electric fields. For example, while the expectation value of the electric field strength for an electron in the ground state of a neutral hydrogen atom is $\langle\mathcal{E}^{(Z=1)}\rangle \sim 10^{12}$ Vm^{-1}, this increases to $\langle\mathcal{E}^{(Z=20)}\rangle \sim 10^{16}$ Vm^{-1} in hydrogen-like calcium and reaches even higher values for hydrogen-like uranium, $\langle\mathcal{E}^{(Z=92)}\rangle \sim 10^{18}$ Vm^{-1} [24] [Ric5], as illustrated in the right panel of Fig. 1.2. Due to these strong

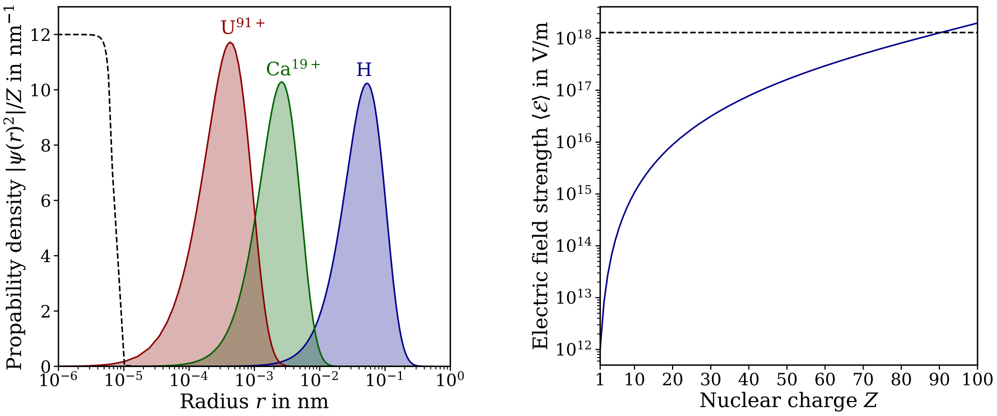

Figure 1.2: The probability density $|\psi(r)|^2/Z$ (left) for an electron in the $1s_{1/2}$ ground state in neutral hydrogen and hydrogen-like calcium and uranium. The density is normalized by the nuclear charge number Z for better visibility. The expectation value of the electric field strength (right) for an electron in the ground state in hydrogen-like ions scales approximately with Z^3.

electric fields and their comparatively simpler electronic structure, HCIs provide a tremendous potential for testing quantum electrodynamics (QED) beyond leading order corrections [9, 25, 26]. Moreover, HCIs are more resistant to external perturbations due to the tight binding of the electrons, making them promising candidates for atomic clocks. Indeed, an optical atomic clock based on the highly charged ion Ar^{13+} has been realized, achieving a relative uncertainty of 10^{-17} [5]. Additionally, the significant overlap between the bound electron's wave function and the nucleus makes HCIs a sensitive probe of nuclear properties, such as nuclear deformations [27, 28]. Furthermore, HCIs are valuable systems for searches of new physics beyond the Standard Model, which we will highlight more in Sec 1.2.4.

Most electronic transitions in HCIs have very high energies, often reaching into the x-ray domain. Returning once more to the example of hydrogenic systems, the $1s_{1/2} \to 2s_{1/2}$ transition energy scales approximately as Z^2. This results in transition energies of $E^{(Z=20)}_{1s_{1/2}\to 2s_{1/2}} \approx 4\,\mathrm{keV}$ for hydrogen-like calcium and $E^{(Z=92)}_{1s_{1/2}\to 2s_{1/2}} \approx 100\,\mathrm{keV}$ for hydrogen-like uranium, compared to $E^{(Z=1)}_{1s_{1/2}\to 2s_{1/2}} \approx 10\,\mathrm{eV}$ for neutral hydrogen [29], see the left panel of Fig. 1.3. Such photon energies can be achieved, for example, with free electron lasers or synchrotron photon sources [30, 31]. Moreover, such transitions are accessible by making use of the Doppler effect and ultra-relativistic ion beams, as it is proposed in the Gamma Factory project at CERN. In fact, the

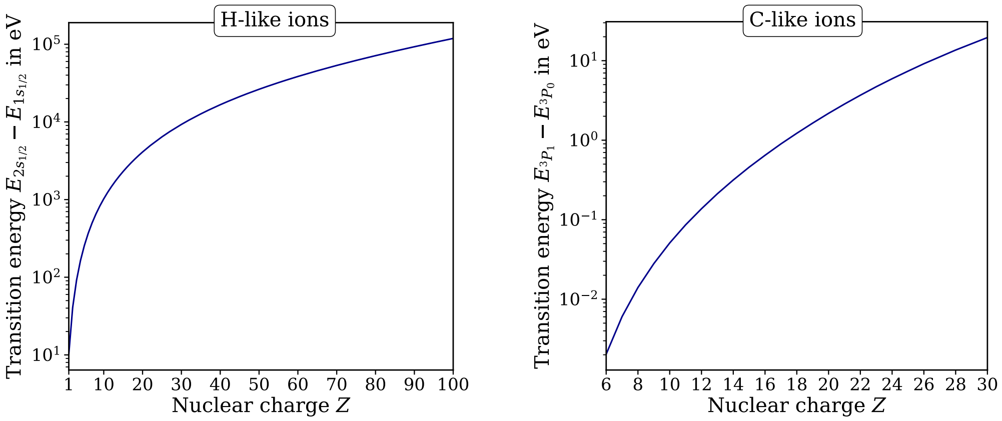

Figure 1.3: The transition energy from the $1s_{1/2}$ groundstate to the excited $2s_{1/2}$ state in hydrogen-like ions from Ref. [29] (left) and the transition energy from the $^3P_0$ groundstate to the excited $^3P_1$ state in carbonlike ions [35] (right)

high transition energies of HCIs are essential to the Gamma Factory concept, which aims to generate high-intensity γ-rays via resonant photon scattering between laser photons and counter-propagating ion beams [11]. We will discuss the Gamma Factory project in more detail in Section 3. However, since such high transition energies are not achievable with conventional lasers, these transitions are not suitable for high-precision spectroscopy as for optical atomic clocks. Nevertheless, HCIs can also exhibit transitions in the optical frequency domain. For instance, fine- or hyperfine-structure transitions, which would typically be in the microwave regime for neutral atoms, can reach the optical frequency domain in HCIs. This is, for instance, the case for the $^3P_0 \rightarrow {}^3P_1$ transition in the carbon isoelectronic sequence, see the right panel of Fig. 1.3. Moreover, level crossing of states with different electronic configurations can occur along an isoelectronic sequence, driven by the competition of the Madelung ordering for neutral atoms and the Coulomb ordering in hydrogen-like ions. Such crossings can give rise to transitions that fall within the range of lasers [32]. Theoretical investigations have identified several narrow optical transitions in HCIs which are suitable for ion clocks with projected uncertainties smaller than 10^{-20} [33, 34].

1.2 THE STANDARD MODEL

A central theme of this thesis is the potential of HCIs to probe the Standard Model of particle physics and search for possible extensions beyond it. Therefore, this section provides a concise overview of the structure and key ingredients of the Standard Model, along with its most prominent shortcomings. We then briefly review some Standard Model extensions that aim to address these limitations. Finally, we give a short overview of different experimental approaches within atomic, molecular and optical physics that are used to test the Standard Model and explore possible new physics.

1.2.1 *Brief introduction to the Standard Model*

The Standard Model of particle physics describes three of the four known fundamental interactions, namely the electromagnetic, weak and strong forces, within the framework of relativistic quantum field theory. These forces are mediated by gauge bosons, which couple to different fermionic matter particles called leptons and quarks. Furthermore, the Higgs field, which was only discovered in 2012 [36, 37], causes the process of electroweak symmetry breaking, giving masses to the weak gauge bosons and the fermions. In this section, we briefly summarize the main components of the Standard Model, following Refs. [38–41].

Gauge fields and coupling to fermionic matter

To understand the structure of the Standard Model, we begin by introducing its underlying gauge symmetry, which dictates the types of interactions and the associated gauge fields. The symmetry group of the Standard Model is given by

$$\mathcal{G}_{\mathrm{SM}} = SU(3)_C \times SU(2)_L \times U(1)_Y, \tag{1.1}$$

where each factor corresponds to the gauge symmetry of one fundamental interaction. The $SU(3)_C$ group describes the strong interaction, which is the main building block of quantum chromodynamics (QCD), while the electroweak interaction is governed by the product group $SU(2)_L \times U(1)_Y$. Each of these gauge symmetries introduces a set of gauge bosons as mediators of the force. The $SU(3)_C$ color gauge group corresponds to the eight massless gluons G^a_μ (with $a = 1, \ldots, 8$), which mediate the strong force between quarks. The electroweak symmetry is governed by the $SU(2)_L \times U(1)_Y$, with the gauge fields W^i_μ (for $i = 1, 2, 3$) from the $SU(2)_L$ and B_μ from $U(1)_Y$. Indeed, $U(1)_Y$ corresponds to the hypercharge interaction and is not associated to the photon. In fact, electromagnetism, the most relevant interaction for atomic physics, is still hidden within the electroweak group $SU(2)_L \times U(1)_Y$. Only after the electroweak symmetry breaking, the photon emerges as a specific linear combination of the W_μ^3 and B_μ gauge fields, as we will discuss in Section 1.2.1. The Lagrangian for the kinetic part of the gauge sector is given by

$$\mathcal{L}_{\text{gauge}} = -\frac{1}{4} G^a_{\mu\nu} G^{a\,\mu\nu} - \frac{1}{4} W^i_{\mu\nu} W^{i\,\mu\nu} - \frac{1}{4} B_{\mu\nu} B^{\mu\nu}, \tag{1.2}$$

where the corresponding field strength tensors are defined as

$$G^a_{\mu\nu} = \partial_\mu G^a_\nu - \partial_\nu G^a_\mu + g_s f^{abc} G^b_\mu G^c_\nu, \tag{1.3a}$$

$$W^i_{\mu\nu} = \partial_\mu W^i_\nu - \partial_\nu W^i_\mu + g \epsilon^{ijk} W^j_\mu W^k_\nu, \tag{1.3b}$$

$$B_{\mu\nu} = \partial_\mu B_\nu - \partial_\nu B_\mu. \tag{1.3c}$$

Here, g_s and g are the coupling constants for the $SU(3)_C$ and $SU(2)_L$ groups, respectively. Moreover, the coupling of the $U(1)_Y$ group is denoted by g' and will appear later.

These different gauge fields couple to different fermionic matter particles, which are distinguished by their charges under the corresponding gauge groups. All of the Standard Model fermions carry a hypercharge, which again should not be confused with the electric charge. The relation between the hypercharge and the electric charge will be discussed later. As indicated by the index L, the weak interaction couples only to left-handed fermions. These transform in the fundamental representation of the $SU(2)_L$ group and hence are written as doublets. In contrast, the right-handed fermions are singlets under the $SU(2)_L$. Finally, the strong interaction couples to fermions which carry a color charge C. This is the case for the quarks, which transform in the fundamental representation of $SU(3)_C$, while the leptons do not carry color charge and thus transform as singlets under $SU(3)_C$. The left-handed quark doublet consists of the left-handed up- and down-type quarks:

$$Q_L = \begin{pmatrix} u_L \\ d_L \end{pmatrix} \sim (3, 2, \tfrac{1}{6}), \tag{1.4}$$

where we use the shorthand notation $(SU(3)_C, SU(2)_L, U(1)_Y)$ to denote the representation under the gauge symmetry groups. Here, "3" and "2" refer to the fundamental representation of $SU(3)_C$ and $SU(2)_L$, respectively, while "1" denotes the singlet representation. The last entry gives the hypercharge of the particle. The right-handed up- and down-type quarks are in this notation:

$$u_R \sim (3, 1, \tfrac{2}{3}), \quad d_R \sim (3, 1, -\tfrac{1}{3}). \tag{1.5}$$

Similarly, there is a left-handed lepton doublet, which consists of the left-handed electron and electron-neutrino:

$$L_L = \begin{pmatrix} \nu_L \\ e_L \end{pmatrix} \sim (1, 2, -\frac{1}{2}). \tag{1.6}$$

However, there is only a right-handed electron:

$$e_R \sim (1, 1, -1), \tag{1.7}$$

but the Standard Model does not include a right-handed neutrino. However, motivated by the discovery of neutrino oscillations, many extensions include right-handed neutrinos $\nu_R \sim (1, 1, 0)$. In fact, the fermionic sector of the Standard Model consists of three generations, such that each of the particles introduced above has two heavier siblings. These are: the charm and top quarks, as heavier counterparts of the up quark, the strange and bottom quarks for the down quark, and the muon and tau for the electron as well as their corresponding neutrinos. Nevertheless, since all three generations of fermions couple identically to the gauge fields, we restrict our discussion to a single generation for simplicity.

To combine the fermionic matter fields with the gauge sector, it is necessary to introduce the covariant derivative. This ensures that the full Lagrangian remains invariant under the different gauge transformations of the Standard Model. The covariant derivative acting on a generic fermion field ψ takes the form

$$D_\mu \psi = \left(\partial_\mu + i g_s \tau^a G^a_\mu + i g \tau^i W^i_\mu + i g' Y B_\mu \right) \psi, \tag{1.8}$$

where τ^a and τ^i are the generators of the respective gauge groups in the representation of ψ, while Y denotes the hypercharge. Using this definition, the kinetic Lagrangian for the Standard Model fermions can be written as

$$\begin{aligned} \mathcal{L}_{\text{Fermi}} =& i \bar{u}_R \sigma^\mu D_\mu u_R + i \bar{d}_R \sigma^\mu D_\mu d_R + i \bar{e}_R \sigma^\mu D_\mu e_R \\ & + i \bar{Q}_L \bar{\sigma}^\mu D_\mu Q_L + i \bar{L}_L \bar{\sigma}^\mu D_\mu L_L. \end{aligned} \tag{1.9}$$

At this point, there is only one Standard Model field missing, which is the infamous Higgs boson. We will explore the impact of this field on the gauge fields in the following.

Electroweak symmetry breaking

So far, all gauge bosons in the Standard Model were introduced as massless, even so experiments clearly show that the weak interaction is mediated by massive vector bosons, which are the $W^\pm$ and Z bosons. Moreover, the photon, the massless mediator of electromagnetism, has not yet emerged in our formulation. These phenomena are explained by the mechanism known as electroweak symmetry breaking.

The last ingredient, which is responsible for this symmetry breaking, is the only scalar boson in the Standard Model, known as the Higgs field:

$$H \sim (1, 2, +\tfrac{1}{2}). \tag{1.10}$$

The Lagrangian describing the dynamics of this field is given by the kinetic term and the symmetry-breaking Higgs potential:

$$\mathcal{L}_{\text{Higgs}} = D_\mu H^\dagger D^\mu H + \lambda \left(H^\dagger H - \frac{v^2}{2} \right)^2 , \tag{1.11}$$

where v denotes the vacuum expectation value (VEV) of the Higgs field. The potential in Eq. (1.11) is constructed such that the Higgs field acquires a non-zero VEV, spontaneously breaking the $SU(2)_L \times U(1)_Y$ gauge symmetry down to a residual $U(1)_{\text{EM}}$ symmetry, which we will identify with electromagnetism. Usually, one might expect from Goldstone's theorem that the spontaneous symmetry breaking would lead to three massless Goldstone bosons. However, such massless scalar particles are not observed in nature, but instead there are massive gauge bosons mediating the weak force. To understand this we investigate the full Lagrangian of the $SU(2)_L \times U(1)_Y$ gauge fields with the Higgs field:

$$\mathcal{L} = -\frac{1}{4} W^i_{\mu\nu} W^{i\,\mu\nu} - \frac{1}{4} B_{\mu\nu} B^{\mu\nu} + D_\mu H^\dagger D^\mu H + \lambda \left(H^\dagger H - \frac{v^2}{2} \right)^2 \tag{1.12}$$

We can choose the ground state of the Higgs field as

$$\langle H \rangle = \frac{1}{\sqrt{2}} \begin{pmatrix} 0 \\ v \end{pmatrix} , \tag{1.13}$$

and then parametrize fluctuations around this vacuum configuration as

$$H = \frac{1}{\sqrt{2}} e^{-i\xi^a T^a} \begin{pmatrix} 0 \\ v + h \end{pmatrix} . \tag{1.14}$$

Here, the three real fields ξ^a and the field h represent the original four degrees of freedom of the Higgs doublet, where the ξ^a correspond to the Goldstone modes. Indeed, plugging this expression into the Lagrangian (1.12), the three Goldstone modes can be absorbed by a suitable gauge transformation. Thus, we can rewrite the Lagrangian (1.12) in the unitary gauge and obtain

$$\mathcal{L} = -\frac{1}{4}W^i_{\mu\nu}W^{i\,\mu\nu} - \frac{1}{4}B_{\mu\nu}B^{\mu\nu} + D_\mu h D^\mu h - \lambda h^2\left(v + \frac{h}{2}\right)^2 \tag{1.15}$$

$$+\frac{1}{8}(v+h)^2\left(g^2\left(W^1_\mu\right)^2 + g^2\left(W^2_\mu\right)^2 + \left(gW^3_\mu - g'B_\mu\right)^2\right). \tag{1.16}$$

We see that only one of the four degrees of freedom of the Higgs doublet remains, which is the physical Higgs boson h. From the Lagrangian (1.16) we can read off its mass as $M_h = \sqrt{2\lambda}v$. The three Goldstone modes were absorbed by the gauge bosons giving rise to their masses. For W^1_μ and W^2_μ, the masses can be read off as $M_W = gv/2$. One can combine these two as $W^\pm = 1/\sqrt{2}\left(W^1_\mu \mp iW^2_\mu\right)$ to obtain the physical $W^\pm$ bosons with electric charge ± 1. The situation is more interesting for W^3_μ and B_μ, which are mixed in the Lagrangian (1.12). The mass matrix can be diagonalized by defining

$$Z_\mu = \cos\theta_W W^3_\mu - \sin\theta_W B_\mu, \tag{1.17a}$$

$$A_\mu = \sin\theta_W W^3_\mu + \cos\theta_W B_\mu, \tag{1.17b}$$

where the weak mixing angle or Weinberg angle is defined as

$$\cos\theta_W = \frac{g}{\sqrt{g^2+g'^2}} \quad \text{or} \quad \sin\theta_W = \frac{g'}{\sqrt{g^2+g'^2}}. \tag{1.18}$$

Using these definitions, Z_μ obtains the mass $M_Z = M_W/\cos\theta_W$ while A_μ remains massless. Finally, we can identify A_μ as the photon field, the mediator of the electromagnetic interaction, which forms the foundation of atomic physics.

The electric charge Q of a particle is related to its hypercharge Y by

$$Q = \tau^3 + Y, \tag{1.19}$$

where, in the fundamental representation of the $SU(2)$, τ^3 can be written as

$$\tau^3 = \frac{1}{2}\begin{pmatrix}1 & 0\\ 0 & -1\end{pmatrix}. \tag{1.20}$$

Therefore, τ^3 yields $\pm 1/2$ when acting on the upper or lower components of a left-handed state and 0 when it acts on a right-handed state. Combining these values with the hypercharges, we obtain for up-type quarks $Q_u = 2/3$, for down-type quarks $Q_d = -1/3$, for neutrinos $Q_\nu = 0$ and finally for the electron and its heavier siblings $Q_e = -1$.

Yukawa couplings and fermion masses

Inspecting $\mathcal{L}_{\text{Fermi}}$, one notices also for the fermions that mass terms are absent in the Lagrangian. In fact, direct mass terms like $m\bar{\psi}\psi$ would break the $SU(2)_L$ gauge symmetry, since left- and right-handed fermions transform differently under it. Similar as in the gauge sector, this issue is resolved by the Higgs field. Again restricting ourselves to a single generation of fermions, the coupling of the fermions to the Higgs field is given by

$$\mathcal{L}_{\text{Yuk}} = -y_e \bar{L}_L H e_R - y_d \bar{Q}_L H d_R - y_u \bar{Q}_L \tilde{H} u_R + h.c., \tag{1.21}$$

where we define $\tilde{H} = i\sigma_2 H^*$ and the y_i are the Yukawa couplings. After the Higgs field aquires a VEV and the spontaneous symmetry breaking, we obtain

$$\mathcal{L}_{\text{mass}} = -\frac{v}{\sqrt{2}} \left(y_e \bar{e}_L e_R + y_d \bar{d}_L d_R + y_u \bar{u}_L u_R \right). \tag{1.22}$$

From this Lagrangian one can directly read off the masses for all the fermions as $m_i = v y_i / \sqrt{2}$, depending on the Higgs VEV and the respective Yukawa coupling. Indeed, the situation becomes a bit more complicated, considering all three generations of fermions. In this case, we can write, for example, the left-handed quarks as:

$$Q_L^i = \begin{pmatrix} u_L^i \\ d_L^i \end{pmatrix} = \left(\begin{pmatrix} u_L \\ d_L \end{pmatrix}, \begin{pmatrix} c_L \\ s_L \end{pmatrix}, \begin{pmatrix} t_L \\ b_L \end{pmatrix} \right) \tag{1.23}$$

and analogous for the right-handed quarks and the left- and right-handed leptons. Plugging these vectors into $\mathcal{L}_{\text{mass}}$, the Yukawa couplings become 3×3 matrices. Diagonalizing these Yukawa coupling matrices for the up and down quarks y_{ij}^u and y_{ij}^d, we would naturally end up with discussing the so-called CKM-matrix and enter the field of flavour physics. However, this goes beyond the scope of this brief overview. More details can be found, for example, in Refs. [38, 41–43]

Putting everything together, the full Lagrangian of the Standard Model is built from the gauge, fermion , Yukawa and Higgs parts discussed above:

$$\mathcal{L}_{\text{SM}} = \mathcal{L}_{\text{gauge}} + \mathcal{L}_{\text{fermi}} + \mathcal{L}_{\text{Yuk}} + \mathcal{L}_{\text{Higgs}}. \tag{1.24}$$

Discrete symmetries: C, P and T

Finally, we briefly introduce three discrete symmetries, which are particularly important in the Standard Model: charge conjugation (C), parity (P) and time reversal (T).

The parity transformation describes the inversion of the spatial coordinates:

$$P : (t, \boldsymbol{r}) \rightarrow (t, -\boldsymbol{r}). \tag{1.25}$$

In contrast, time reversal flips the sign of the time coordinate and leaves the spatial coordinates unchanged:

$$T : (t, \boldsymbol{r}) \rightarrow (-t, \boldsymbol{r}). \tag{1.26}$$

The explicit action of these transformations on the different fields in the Standard Model is discussed in detail in Refs. [38, 41].

Finally, charge conjugation can be understood as the exchange of a particle with its anti particle. Its action on a Dirac spinor ψ is given by

$$C : \psi \rightarrow -i\gamma^2\psi^*. \tag{1.27}$$

While each of these symmetries can be violated individually in the Standard Model, as it is the case for P and C as well as for their combination CP, due to the weak interaction, the combination of all three discrete symmetries, CPT, is preserved. Indeed, the CPT theorem states that this is the case for all unitary, local, Lorentz-covariant quantum field theories of point particles in flat Minkowski space [44, 45].

1.2.2 *Limitations of the Standard Model*

The Standard Model has been thoroughly tested over the past decades and shows remarkable agreement with experimental observations. Perhaps the most astonishing example is the electron's magnetic moment, for which experiment and theory deviate by only about one part per trillion [46]. Despite its tremendous success, the Standard Model is widely regarded as an incomplete theory. While it provides an accurate description of particle interactions at currently accessible energies, it leaves several theoretical questions unresolved. Notably, it does not include gravity within a quantum framework, and the observed smallness of the Higgs boson mass compared to the Planck scale gives rise to the so-called hierarchy problem. Loop corrections to the Higgs mass depend quadratically on the cutoff scale Λ of the theory:

$$m_H = m_H^{(\text{bare})} + \delta m_H, \quad \text{with} \quad \delta m_H \propto \Lambda^2. \tag{1.28}$$

Therefore, keeping the physical Higgs mass light requires a precise cancellation between the bare mass and the corrections, which might be considered as an apparent fine-tuning [41, 47, 48]. Another issue that is often regarded as a fine-tuning problem is the strong CP problem. The Standard Model allows for an additional term, the so-called θ-term, in the QCD Lagrangian,

$$\mathcal{L}_\theta = \theta \frac{g_s^2}{32\pi^2} \epsilon^{\mu\nu\rho\sigma} G_{\mu\nu} G_{\rho\sigma}, \tag{1.29}$$

which would lead to CP violation in the strong interaction. Experiments, such as measurements of the neutron electric dipole moment, constrain this term to be extremely small and consistent with zero. However, there is no fundamental reason within the Standard Model for it to vanish [49–51].

Moreover, the Standard Model fails to account for several well-established experimental observations. In the following, we briefly review some of the most prominent of these empirical shortcomings, namely, the existence of dark matter, the matter-antimatter asymmetry of the Universe, and the phenomenon of neutrino oscillations.

Dark Matter

One of the most striking indications of physics beyond the Standard Model, the seeming existence of dark matter, arises from astrophysical and cosmological observations.

Already in the 1930s, Fritz Zwicky proposed the presence of dark matter to explain his observations of the Coma cluster [52]. In particular, he compared the total mass inferred from the relative velocities of the galaxies in the Coma cluster with the mass estimated from the measured luminosity. The latter appeared to be about 400 times smaller, leading him to argue for the existence of a large amount of non-visible matter.

In the 1970s, further support for dark matter was delivered through studies of the rotation curves of spiral galaxies [53]. As a matter of fact, the measured rotational velocities of stars and gas in these galaxies do not match the dynamics expected from only the visible luminous matter. Indeed, the observed velocities do not decrease for large distances from the center of the galaxy, as one would expect from the visible matter, but instead they stabilize or even slightly increase. This discrepancy, illustrated in the left panel of Fig. 1.4, can be resolved by introducing a dark matter halo, which extends far beyond the visible matter.

Further evidence arises from the phenomenon of gravitational lensing. According to general relativity, massive objects bend the path of light and thus can act similarly to a lens when they are located between the light source and the observer. As a result, the observer sees the light on a ring or an arc around the massive object, depending on its mass distribution and the position of the light source, see right panel of Fig. 1.4. In many cases, the gravitational lensing effect reveals a mass distribution

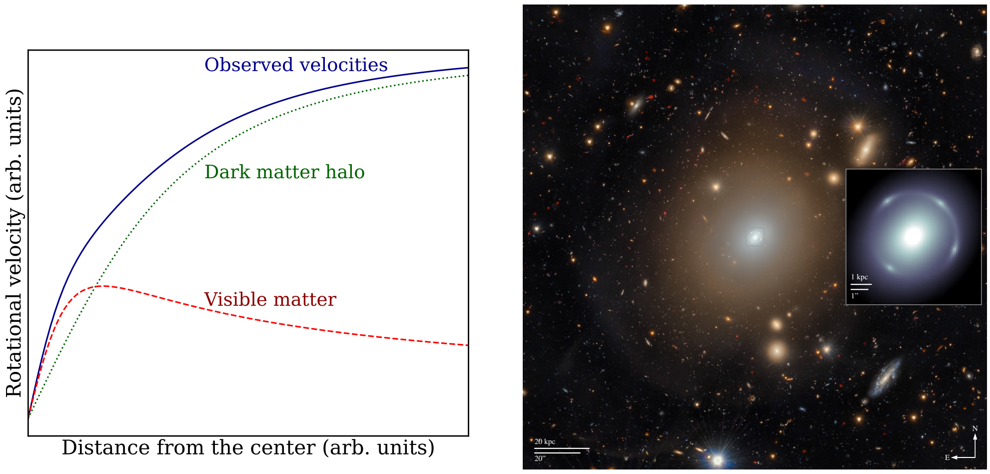

Figure 1.4: The left panel shows a schematic illustration of a rotation curve of spiral galaxy. The observed velocities do not match the prediction inferred from the visible matter and suggest the presence of a dark matter halo. The right panel shows the the gravitational lensing effect observed by the Euclid telescope around the galaxy NGC 6505 (figure taken from Ref. [59])

that significantly deviates from the luminous matter [54–57].
On even larger scales, the cosmic microwave background provides further support for dark matter. The small amplitude of its temperature fluctuations indicates that, if only ordinary luminous matter were present, the density perturbations would not have had enough time to grow into the structures observed today. Therefore, the existence of dark matter is crucial for the formation of galaxies and large-scale structures [58].

Matter-antimatter asymmetry

Another well-established observation pointing to physics beyond the Standard Model is the excess of matter over antimatter in the universe. The magnitude of this assymmetry is commonly quantified by the baryon-to-photon ratio η, which can be inferred from calculations of big bang nucleosynthesis. In these, η enters as an input parameter to estimate abundances of light elements in the early universe. Alternatively, η can be obtained from the power spectrum of temperature fluctuations in the cosmic microwave background. Indeed, both methods agree well and yield values of the order $\eta \sim 6 \times 10^{-10}$ [62,63].

To explain this baryon asymmetry, Andrey Sakharov formulated three conditions that any theory must satisfy [39, 60–64]:

(I) Baryon number violation: Necessary to generate an asymmetry between baryon and antibaryon numbers

(II) C and CP violation: Needed so that the rates of processes producing baryons and antibaryons are not identical.

(III) Out of thermal equilibrium: Otherwise any generated asymmetry would be erased by CPT-invariance.

As a matter of fact, all three conditions are fulfilled in the Standard Model. The Baryon number can be violated through so-called sphaleron processes. While both C and P are violated in the weak interaction, also the combination CP is violated through the CKM matrix. The third condition can be fulfilled during the electroweak phase transition, which refers to the time in the early universe when the electroweak symmetry was spontaneously broken due to the Higgs field acquiring a vacuum expectation value. However, calculations show that it is not possible to quantitatively account for the observed matter-antimatter asymmetry within the Standard Model. This is an indication that additional sources of CP violation are required, pointing once again to physics beyond the Standard Model.

Neutrino oscillations

As mentioned in Section 1.2.1, the Standard Model does not include right-handed neutrinos. As a consequence, we were not able to add a Yukawa term for the neutrinos in the Lagrangian (1.21), such that the neutrinos do not receive a mass through the Higgs mechanism. However, the observation of neutrino oscillations provides clear evidence that neutrinos do, in fact, have nonzero masses. Evidence for these neutrino oscillations can be obtained by the detection of solar neutrinos, which has been achieved already in 1968 [64, 65]. In this experiment, the measured flux of electron neutrinos was smaller than expected. Neutrino oscillations were suggested as an explanation of this finding. The idea was that the missing electron neutrinos were transformed into other flavours, which were not detected by the experiment. Further confirmation came from the Super-Kamiokande and the Sudbury Neutrino Observatory experiments, which are both sensitive to neutrinos of all three generations and were able to find the missing neutrinos [64, 66–68]. These results strongly support the idea of neutrino oscillations. Theoretically, this would require a non-diagonal mass matrix, which would lead to flavour-mixing analogous to the CKM matrix for the quark sector. However, the origin of neutrino masses still remains unknown. Possible solutions include the introduction of sterile right-handed neutrinos and the seesaw mechanism, which is explained, for example, in Refs. [69, 70].

1.2.3 *New physics beyond the Standard Model*

A wide range of extensions to the Standard Model have been proposed to address one or multiple of the shortcomings discussed above. These models cover a wide energy scale, as for example possible dark matter candidates range from ultralight particles with masses as small as 10^{-22} eV to primordial black holes with several solar masses, see Fig. 1.5.

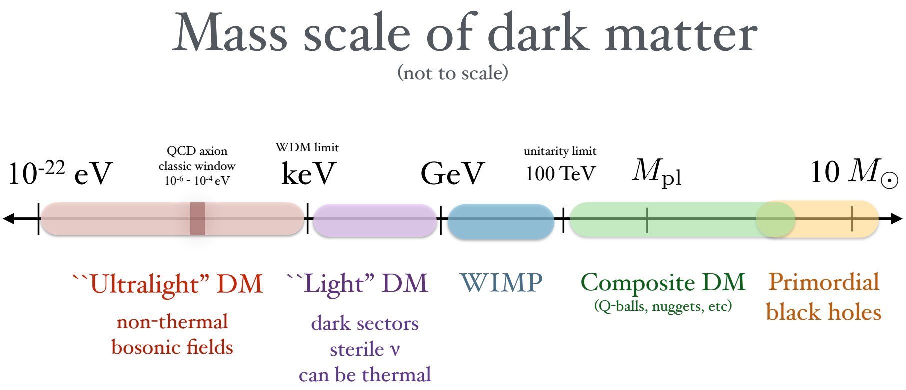

Figure 1.5: Schematic mass range of dark matter candidates, from ultralight bosons to primordial black holes. Figure taken from Ref. [71].

Atomic physics experiments are particularly sensitive probes for particles with smaller masses below the GeV scale. This offers a complementary strategy to high-energy collider experiments, which are more sensitive to heavier particles. Indeed, many extensions of the Standard Model introduce new light bosons with very weak couplings to Standard Model particles. Especially light scalar particles can naturally arise as pseudo-Goldstone bosons through the spontaneous breaking of approximate global symmetries.

One of the most prominent examples of such light particles is the pseudoscalar axion, originally introduced to resolve the strong CP problem. The Peccei–Quinn mechanism introduces a new global $U(1)$ symmetry that is spontaneously broken, giving rise to the axion. Hereby, the main idea is that the axion promotes the θ-parameter in the CP-violating term in the QCD Lagrangian to a dynamical variable by replacing it with $\theta_{\rm eff} = \theta + a(x)/f_a$, where a is the axion field and f_a is the axion decay constant. The axion potential is minimized at $a = -\theta f_a$ such that the CP-violating term is effectively canceled [72–75]. Moreover, the axion would be a viable dark matter candidate. As the original QCD axion has been increasingly constrained, more models emerged that introduce such light bosons which are usually summarized as axion-like particles. Another more recently proposed example of such a light pseudo-Goldstone boson is the scalar relaxion, which is also a dark matter candidate and simultaneously addresses the electroweak hierarchy problem. The dynamics of the relaxion are governed by a linear potential, along which it rolls down during the early universe. Due to its coupling to the Higgs field, the relaxion introduces an effective Higgs mass term that changes over time as the relaxion evolves. This scanning of the Higgs mass is stopped when the electroweak symmetry breaks and the Higgs acquires the observed VEV. The stopping occurs due to an additional periodic term in the relaxion potential which becomes significant at the electroweak energy scale. This term causes the relaxion to become trapped in a local minimum, causing the Higgs mass to stabilize near its observed value [76–79].

Another broad class of Standard Model extensions introduces new $U(1)$ gauge symmetries. One prominent example is the gauging of baryon minus lepton number $(B - L)$, which becomes anomaly-free through the introduction of right-handed neutrinos. Such a gauge symmetry would give rise to a new gauge boson A'_{B-L}, which could directly couple to the Standard Model fermions [80–82].

Moreover, there are considerations of hidden dark sectors, consisting of particles which are neutral under the Standard Model forces but might still interact with the Standard Model particles through so-called portal interactions [83–85]. For example, a scalar mediator ϕ can interact with the Standard Model through the so-called Higgs portal, where the new scalar mixes with the Higgs [83–85]

$$\mathcal{L}^{(H)}_{\text{portal}} = \left(\mu\phi + \lambda\phi^2\right) H^\dagger H. \tag{1.30}$$

Moreover, a fermionic mediator N might interact with the Standard Model through the neutrino portal via a Yukawa coupling to lepton doublets [83, 85]

$$\mathcal{L}^{(N)}_{\text{portal}} = y\bar{L}_L H N_R. \tag{1.31}$$

The vector portal yields another example for a new gauge boson, the dark photon, which could mediate between the Standard Model particles and a hidden dark sector. In this case the dark photon A' mixes in the kinetic term with the Standard Model hypercharge boson [83–85]

$$\mathcal{L}^{(A')}_{\text{portal}} \propto B_{\mu\nu} F'^{\mu\nu}, \tag{1.32}$$

with $F'_{\mu\nu} = \partial_\mu A'_\nu - \partial_\nu A'_\mu$. This would allow the dark photon to weakly interact with Standard Model particles, even though they are not directly charged under the new

$U(1)$ symmetry group [86]. Finally, also a pseudoscalar a could take the role of a mediator between the Standard Model and a Hidden sector through the axion portal. In this case, couplings to different fields would be possible. For example, the coupling to photons would take the form [83, 85]

$$\mathcal{L}^{(a)}_{\text{portal}} = \frac{a}{2f_a}\epsilon^{\mu\nu\rho\sigma}F_{\mu\nu}F_{\rho\sigma}. \tag{1.33}$$

In contrast to the other three portals, the axion portal is a dimension-5 operator and consequently has to be suppressed by a higher mass scale, which is given here by the axion decay constant f_a.

In the next section, we will explore how such Standard Model extensions can be probed by the means of atomic, molecular and optical physics.

1.2.4 *Precision tests of the Standard Model in atomic, molecular, and optical physics*

In the last decades, atomic, molecular, and optical physics emerged as a powerful tool in the search for new physics beyond the Standard Model. The exceptional precision achievable in such laboratory experiments enables the probing of even tiny effects from new physics, especially in the low-energy regime. This so-called precision frontier offers a complementary approach to high-energy collider experiments, enabling a wide range of Standard Model tests. The lack of newly discovered heavy particles at the LHC has further motivated the exploration of light new particles, such as weakly coupled bosons. As discussed in the previous section, these can naturally arise as pseudo-Goldstone bosons, such as the axion or the relaxion [87].

Atomic parity violation

One of the first applications of precise atomic physics experiments to particle physics was the study of atomic parity violation. It was first discussed already in the 1950s by Zel'dovich, shortly after the first experimental confirmation that the weak interaction violates parity [88–90]. In atoms, the weak interaction between the nucleus and bound electrons, mediated by the Z boson, leads to the mixing of opposite-parity atomic states. The measurement of such parity-violating effects in atoms allows the extraction of the Weinberg angle at low energies, far below the scales accessible by collider experiments. Furthermore, the comparison of the Standard Model prediction to the experimental results allows to set constraints on possible beyond Standard Model physics, such as additional new Z' gauge bosons. In the 1970s, atomic parity violation was reconsidered and eventually successfully observed via optical rotation of light propagating through bismuth vapor. Later experiments followed in thallium, lead, cesium and ytterbium [91–97]. Among these, atomic parity violation in cesium remains the most precise low-energy measurement of the Weinberg angle. Future experiments are discussed, for example, in dysprosium, francium as the heavier analogue to cesium or in single ion experiments with singly charged radium or barium ions [98–102]. Moreover, there is ongoing process in molecules as well as considerations for parity violation studies in highly charged ions and muonic atoms [103–108] [Ric1]. HCIs and muonic atoms are particularly attractive due to the large overlap between the electronic or muonic wavefunctions and the nucleus, which enhances the parity-violating signal. Additionally, the occurrence of level crossings in HCIs can lead to nearly degenerate opposite-parity states, which also amplifies the parity-violating effects. Moreover, their relatively simple electronic structure simplifies accurate atomic theory calculations, which are crucial for the interpretation of atomic parity violation measurements.

P and T violation: EDM searches

Not only P violation, but also T violation can be probed with atomic and molecular systems. If CPT symmetry holds, which has been tested experimentally to high precision [109–111], such breaking of T invariance directly implies CP violation. As discussed in the previous section, the search for additional CP violation beyond the Standard Model is especially important for the understanding of the matter-antimatter asymmetry. A powerful tool for such an investigation is the search for effects of permanent electric dipole moments in atoms and molecules. Such phenomena can arise, for instance, from T and P violating interactions between the nucleus and the bound electrons, from the existence of a non-zero electron electric dipole moment or from a nuclear Schiff moment. Precise experiments have been performed, for example, with Cs, Tl, Xe, Hg and Ra atoms or with polar molecules like TlF, YbF, ThO and HfF^+ [87, 112–115]. Additionally, there is progress in studies with molecules including nuclei with a strong octopole deformation, such as RaF, which can significantly enhance sensitivity to CP violating effects [116]. Moreover, there are considerations for storage ring experiments with HCIs, which again are attractive because of the large overlap of electronic wavefunctions with the nucleus and the occurrence of close-lying opposite-parity states [117].

Axion searches

While the previous examples focused on the violation of discrete symmetries, other experimental efforts explore specific couplings between new particles and Standard Model fields. In the case of the axion or axion-like particles, many experiments investigate their coupling to photons, as, for example, the HAYSTAC experiment, or so-called light-shining-through-a-wall setups [120–123]. The HAYSTACK experiment searches for signals from axion-photon conversion via the inverse Primakoff effect by placing a microwave cavity in an external magnetic field. In light-shining-through-a-wall experiments, an opaque barrier is placed between a photon source and a detector. While no photons could normally pass this barrier, the intermediate conversion of photons into axion-like particles could effectively allow light to shine through the wall. Especially, this latter approach can benefit from HCI physics, since HCIs may serve as a source of high-energy photons for similar experiments, as it is considered within the Gamma Factory project, to which we will return in Section 3.5. Moreover, such couplings to photons are explored in the ABRACADABRA experiment [118, 119]. In addition to the photon coupling, interactions with gluons or fermions are also studied, for example, in the CASPEr experiment [124–128].

Clock comparisons

Perhaps the most astonishing demonstration of the precision in atomic, molecular and optical physics are atomic clocks, which now reach relative uncertainties below 10^{-18} [129]. One major application of this extraordinary precision is the search for possible temporal or spatial variation of fundamental constants, like the proton to electron mass ratio m_p/m_e or the fine-structure constant α. As mentioned earlier, the first optical atomic clock based on a HCI has already been realized, and theoretical investigations identified various suitable clock transitions in HCIs [5, 33, 34]. These systems are particularly promising for such studies, as they can exhibit high sensitivity to variations of α [10]. Such variations would manifest as differential frequency shifts in clocks based on different atomic species or transitions and hence can be probed with clock comparison experiments [87, 130–132]. Recently, the successful laser excitation of the Th-229 nucleus presented a huge step towards the development of the first nuclear clock [133–137]. Such a nuclear clock holds immense potential for future clock comparison experiments, as it would also be sensitive to variations of the QCD scale.

Isotope shifts

Another example of the use of precision spectroscopy is the analysis of isotope shifts, which are the energy differences of a given electronic transition across different isotopes of the same element. Such measurements have long been used to extract nuclear parameters, such as the nuclear charge radius [138–141]. Recently, also their potential for the search of new physics have been in the focus, as isotope shifts are sensitive to interactions between bound electrons and neutrons mediated by beyond Standard Model bosons [142, 143]. In particular, isotope shift measurements in calcium and ytterbium have been proven to be valuable tools to constrain such new boson couplings [144–150]. Such studies generally require precise isotope shift measurements across multiple transitions. Therefore, including HCIs in the analysis provides a notable advantage, as the variation of the ionic charge state can be used to enlarge the set of available transitions [152]. In the next chapter, we will discuss the theory of isotope shifts in more detail and present the results of an analysis that makes use of a highly charged calcium ion.

2

ISOTOPE SHIFTS AS A PROBE FOR NEW PHYSICS

This chapter focuses on a powerful application of the extraordinary precision achieved in modern atomic spectroscopy: the analysis of isotope shifts. Traditionally, isotope shifts have been used to extract nuclear charge radii across different isotopes. However, more recently they have emerged as a valuable tool in the search for physics beyond the Standard Model [142, 143]. A key advantage of isotope shifts is that they present a differential measurement, such that a large part of the Standard Model background cancels in the measurement and does not need to be addressed theoretically. This allows for the use of many-electron atomic systems, which are otherwise difficult to treat with high theoretical accuracy, to probe new physics. In contrast, the direct comparison of transition frequencies between theory and experiment requires extremely precise theoretical calculations and is thus only possible in few-electron systems [26, 153–155]. In particular, isotope shifts are sensitive to new bosons in the mass range from eV to MeV that couple to electrons and neutrons. Such particles are predicted in a wide variety of extensions to the Standard Model [156]. These include the ones discussed in the previous chapter, such as the relaxion, new gauge bosons associated with a $U(1)_{B-L}$ symmetry or vector bosons mediating interactions with hidden sectors via portal couplings, such as the dark photon. Additional interest in such searches has arisen from the so-called beryllium anomaly, observed as an unexpected feature in the angular distribution of e^+e^- pairs produced in a nuclear transition of ^{8}Be, which has been interpreted as an indication of a possible new boson [157]. In particular, this observation can be explained by the introduction of a protophobic vector gauge boson with a mass around 17 MeV. Protophobic refers to the property that its coupling to protons is strongly suppressed relative to its coupling to neutrons, making it an especially interesting candidate for isotope shift studies [158, 159]. Follow-up studies by the same group revealed similar anomalies for ^{12}C and ^{4}He nuclei, supporting the existence of a new 17 MeV boson [160, 161]. However, a more recent experiment using the MEG II detector at PSI did not reproduce such an anomaly for the ^{8}Be nucleus [162]. Interestingly, in Ref. [163] the resonance of the new boson was searched via e^+e^- annihilation with the PADME experiment, finding a 2σ deviation from the null hypothesis at an energy of approximately 16.9 MeV.

Within the Standard Model, the leading-order contributions to isotope shifts predict a linear relation between the isotope shifts of two transitions. This can be illustrated in a so-called King plot, where the isotope shifts of the two transitions are plotted against each other. However, a new boson coupling to electrons and neutrons could lead to deviations from this linear behavior. Consequently, if the King plot remains linear within experimental uncertainties, bounds can be placed on the allowed coupling strength of the hypothetical new boson [143]. This motivated a number of precision isotope shift measurements, most notably in calcium and ytterbium [144–150]. While the calcium King plots remained linear, indeed the studies in ytterbium revealed a notable nonlinearity [147–151]. However, nonlinearities in King plots can also arise from higher-order Standard Model effects, such as nuclear deformations, higher-order field and mass shift terms, or nuclear polarization [164]. Hence, the interpretation of a nonlinear King plot is not easy and possible Standard Model sources have to be evaluated. In fact, the observed nonlinearities in ytterbium were attributed to effects of the nuclear shape, rather than to new physics. However, the possibility of a new physics contribution in addition to the nuclear shape effects remains. This also highlights the dual use of the search for King plot nonlinearities, as they can also serve as sensitive probes of nuclear effects.

In Section 2.1, we begin this chapter by reviewing the leading contributions to isotope shifts, the mass shift and the field shift. We then summarize several higher-order Standard Model effects that can give rise to King plot nonlinearities. Moreover, we discuss how a hypothetical new boson would contribute to the isotope shift. Afterwards, we focus on the King plot formalism in Section 2.2. Here, we explain how linear King plots can be used to place constraints on new bosons. However, as mentioned above, the presence of Standard Model nonlinearities requires additional effort. Therefore, we will describe the so-called generalized King plot, which allows us to set limits on new physics even in the presence of Standard Model nonlinearities, and the decomposition plot, which allows to distinguish between different sources of nonlinearity. Finally, in Section 2.3, we present the results of a recent King plot analysis that combines newly measured isotope shifts in singly charged calcium and highly charged Ca^{14+}. As we will see, this combination yields the most stringent isotope-shift-based bounds on new physics to date.

2.1 ISOTOPE SHIFT THEORY

The term isotope shift refers to the difference in atomic energy levels between isotopes of the same element. Since different electronic states respond differently to small changes in the nuclear properties, this leads to measurable shifts in atomic transition frequencies. In this section, we review the different contributions to the isotope shift, illustrated in Fig. 2.1. We begin with the leading-order effects, which are the first-order mass and field shifts, and then provide an overview of some higher-order contributions. Finally, we will explore how a new boson interaction might contribute.

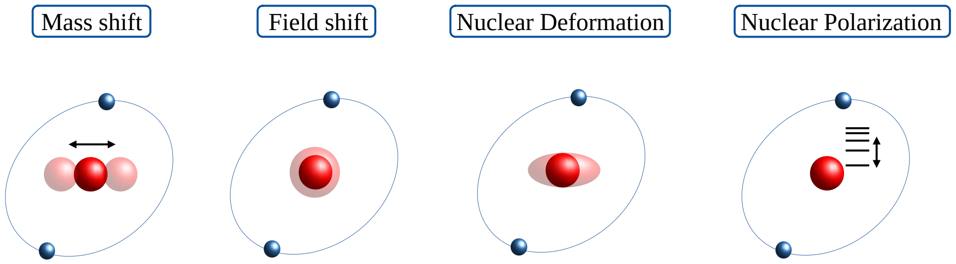

Figure 2.1: Schematic illustration of different isotope shift contributions. The mass shift describes the recoil correction to the kinetic energy part due to the finite mass of the nucleus. The field shift describes the correction due to changes of the nuclear radius. Nuclear deformation effects arise due to changes in the nuclear shape and nuclear polarization takes the internal dynamic structure of the nucleus into account.

2.1.1 *Leading order effects*

In first-order perturbation theory, there are two main contributions to the isotope shift, namely the first-order field shift and mass shift. The field shift arises from the finite size of the nucleus and accounts for the change in the nuclear charge radius between isotopes. This effect becomes dominant in heavy atoms, where the electron wave functions have significant overlap with the nucleus. In contrast, for lighter systems the mass shift is the leading contribution. It originates from the change in the recoil correction to the atomic energy levels due to the difference in nuclear mass between isotopes [165].

Mass shift

We begin our discussion with the recoil correction in the nonrelativistic hydrogen atom. Although we use relativistic units throughout this thesis, in this section, we keep the electron mass m_e explicitly, as it is essential for recoil corrections and the resulting mass shift. The total Hamiltonian of a hydrogen-like system with a finite nuclear mass is given by

$$H = \frac{\boldsymbol{P}^2}{2M} + \frac{\boldsymbol{p}^2}{2m_e} - \frac{Z\alpha}{|\boldsymbol{r} - \boldsymbol{R}|} \tag{2.1}$$

where $\boldsymbol{p}$, $\boldsymbol{r}$ and m_e denote the electron's momentum, position and mass, while $\boldsymbol{P}$, $\boldsymbol{R}$ and M refer to the momentum, position and mass of the nucleus. To analyze the system in the center-of-mass frame, we define the center-of-mass coordinate

$$\boldsymbol{R}_{\text{CM}} = \frac{M\boldsymbol{R} + m_e\boldsymbol{r}}{M + m_e}, \tag{2.2}$$

and the location of the electron relative to the nucleus

$$\rho = \boldsymbol{r} - \boldsymbol{R}. \tag{2.3}$$

Using these definitions, the momenta in Eq. (2.1) transform as:

$$\boldsymbol{p} = -i\hbar\nabla_{\boldsymbol{r}} = -i\hbar\left(\frac{m_e}{M + m_e}\nabla_{\boldsymbol{R}_{\text{CM}}} + \nabla_{\boldsymbol{\rho}}\right) = \frac{m_e}{M + m_e}\boldsymbol{P}_{\text{CM}} + \boldsymbol{\pi}, \tag{2.4a}$$

$$\boldsymbol{P} = -i\hbar\nabla_{\boldsymbol{R}} = -i\hbar\left(\frac{M}{M + m_e}\nabla_{\boldsymbol{R}_{\text{CM}}} - \nabla_{\boldsymbol{\rho}}\right) = \frac{M}{M + m_e}\boldsymbol{P}_{\text{CM}} - \boldsymbol{\pi}, \tag{2.4b}$$

where $\boldsymbol{P}_{\text{CM}} = -i\hbar\nabla_{\boldsymbol{R}_{\text{CM}}}$ denotes the momentum of the center of mass and $\boldsymbol{\pi} = -i\hbar\nabla_{\boldsymbol{\rho}}$ corresponds to the conjugated momentum of the relative coordinate $\boldsymbol{\rho}$. Plugging these expressions into the Hamiltonian (2.1), we obtain the expression

$$H = \frac{\boldsymbol{P}_{\text{CM}}^2}{2\left(M + m_e\right)} + \frac{\boldsymbol{\pi}^2}{2\mu} - \frac{Z\alpha}{|\boldsymbol{\rho}|}, \tag{2.5}$$

with the reduced mass

$$\mu = \frac{m_e M}{m_e + M}. \tag{2.6}$$

The first term in Eq. (2.5) describes the motion of the center of mass, which is irrelevant for our analysis of the internal atomic structure. In the rest frame of the center of mass, where $\boldsymbol{P}_{\text{CM}} = 0$, the Hamiltonian simplifies to [166–169]

$$H_{\text{CM}} = \frac{\boldsymbol{\pi}^2}{2\mu} - \frac{Z\alpha}{\rho}. \tag{2.7}$$

This expression is identical to the well-known hydrogenic Hamiltonian for a nucleus with infinite mass, except that the electron mass is replaced by the reduced mass. We can separate this Hamiltonian into the infinite nuclear mass case H_0 plus a perturbation depending on the nuclear mass

$$H_{\mathrm{CM}} = \frac{\boldsymbol{\pi}^2}{2M} + \frac{\boldsymbol{\pi}^2}{2m_e} - \frac{Z\alpha}{\rho} = H_0 + \frac{\boldsymbol{\pi}^2}{2M}. \tag{2.8}$$

In first-order perturbation theory, the energy correction to a state $|a\rangle$ is given by the expectation value of the perturbation Hamiltonian

$$\Delta E_a = \left\langle a \left| \frac{\boldsymbol{\pi}^2}{2M} \right| a \right\rangle = \frac{m_e}{M} \left\langle a \left| \frac{\boldsymbol{\pi}^2}{2m_e} \right| a \right\rangle = -\frac{m_e}{M} E_a^{(0)}, \tag{2.9}$$

where $E_a^{(0)}$ is the unperturbed energy of the state $|a\rangle$. In the last step, we used the virial theorem which relates the expectation values of the kinetic and potential energies as $2\langle T\rangle = \langle V\rangle$. With $H = T + V$, this leads to $\langle T\rangle = -\langle H\rangle = -E$ [170]. Thus, the first-order mass shift of the state $|a\rangle$ between the two isotopes A and A' is given by

$$\Delta E_a^{\mathrm{NMS}} = \left(\frac{m_e}{M_{A'}} - \frac{m_e}{M_A}\right) E_a^{(0)}. \tag{2.10}$$

This is called the normal mass shift (NMS). In the case of a many-electron atom, the kinetic energy part of the Hamiltonian takes the form

$$T = \frac{\boldsymbol{P}^2}{2M} + \frac{1}{2m_e}\sum_k \boldsymbol{p}_k^2. \tag{2.11}$$

Proceeding as before, we find the kinetic energy in the center-of-mass frame as [166–169]

$$T_{\mathrm{CM}} = \frac{1}{2\mu}\sum_k \boldsymbol{\pi}_k^2 + \frac{1}{M}\sum_{k<l} \boldsymbol{\pi}_k \cdot \boldsymbol{\pi}_l = T^{(0)} + T^{\mathrm{NMS}} + T^{\mathrm{SMS}}. \tag{2.12}$$

The first term contains both the unperturbed kinetic energy and the normal mass shift correction. The last term, which does not arise in hydrogen-like systems, is a two-body operator known as the specific mass shift (SMS). The full mass shift operator can thus be written as

$$H_{\mathrm{MS}} = \frac{1}{2M}\left(\sum_k \boldsymbol{\pi}_k^2 + \sum_{k\neq l} \boldsymbol{\pi}_k \cdot \boldsymbol{\pi}_l\right) = \frac{1}{2M}\sum_{k,l} \boldsymbol{\pi}_k \cdot \boldsymbol{\pi}_l, \tag{2.13}$$

and the first-order mass shift of a state $|a\rangle$ is given by

$$\Delta E_a^{AA',\mathrm{MS}} = \left(\frac{1}{M_{A'}} - \frac{1}{M_A}\right)\left\langle a \left| \frac{1}{2}\sum_{k,l} \boldsymbol{\pi}_k \cdot \boldsymbol{\pi}_l \right| a \right\rangle \tag{2.14}$$

Accordingly, the mass shift of a transition i between the states $|a\rangle$ and $|b\rangle$ becomes

$$\begin{aligned} \nu_i^{AA',\mathrm{MS}} &= \left(\frac{1}{M_{A'}} - \frac{1}{M_A}\right)\left(\left\langle b \left| \frac{1}{2}\sum_{k,l} \boldsymbol{\pi}_k \cdot \boldsymbol{\pi}_l \right| b \right\rangle - \left\langle a \left| \frac{1}{2}\sum_{k,l} \boldsymbol{\pi}_k \cdot \boldsymbol{\pi}_l \right| a \right\rangle\right) \\ &\equiv \left(\frac{1}{M_{A'}} - \frac{1}{M_A}\right) K_i, \end{aligned} \tag{2.15}$$

where the factor K_i captures the electronic structure contribution to the mass shift for the specific transition i.

So far, we have restricted the discussion to a nonrelativistic description. However, especially for heavy atoms and HCIs, relativistic effects must be taken into account to achieve accurate results. A commonly used relativistic recoil operator for precise calculations is given by [165, 171, 172]

$$H_{\mathrm{MS}}^{\mathrm{rel}} = \frac{1}{2M}\sum_{k,l}\left[\boldsymbol{\pi}_k \cdot \boldsymbol{\pi}_l - \frac{Z\alpha}{\rho_k}\left(\boldsymbol{\alpha}_k + \frac{(\boldsymbol{\alpha}_k \cdot \boldsymbol{\rho}_k)\boldsymbol{\rho}_k}{\rho_k^2}\right) \cdot \boldsymbol{\pi}_l\right], \tag{2.16}$$

where $\boldsymbol{\alpha}_k$ denotes the vector of Dirac matrices, $\alpha_i = \gamma^0\gamma_i$ of the k-th electron. A full derivation of this operator is beyond the scope of this work, and we refer the reader to Refs. [171, 172] for a detailed discussion.

Field shift

While we previously focused on the kinetic part of the Hamiltonian for recoil corrections, the field shift arises from modifications of the potential due to the finite size of the nucleus. In the simplest model, the nucleus is treated as a point charge, leading to the Coulomb potential

$$V_{\mathrm{Coul}}(r) = -\frac{Z\alpha}{r}. \tag{2.17}$$

However, especially for heavier atoms and HCIs, where electron wave functions have a significant overlap with the nucleus, the finite nuclear size must be taken into account. A simple model replaces the point-like nucleus with a homogeneously charged sphere of radius R. The corresponding charge distribution and the resulting nuclear potential are given by [167, 173]

$$\varrho(r) = \begin{cases} \dfrac{3Z\alpha}{4\pi R^3}, & r \leq R \\ 0, & r > R \end{cases} \quad \rightarrow \quad V_N(r) = Z\alpha \begin{cases} \dfrac{1}{R}\left(\dfrac{r^2}{2R^2} - \dfrac{3}{2}\right), & r \leq R \\ \dfrac{1}{r}, & r > R \end{cases} \tag{2.18}$$

To gain first insights into the effect of such a modified nuclear potential, we again consider the example of nonrelativistic hydrogen. In first-order perturbation theory, the energy correction to a state $|a\rangle$ due to the potential (2.18) is

$$\Delta E^{\text{sphere}} = \left\langle a \middle| V^{\text{sphere}}(r) - V^{\text{point}}(r) \middle| a \right\rangle \tag{2.19}$$

By using the well-known hydrogen solutions

$$\psi_{nlm}(\boldsymbol{r}) = Y_l^m(\theta, \phi)\mathcal{R}_{nl}(r), \tag{2.20}$$

the angular integral is trivially solved due to the orthonormality of the spherical harmonics Y_l^m, and the remaining radial integral can be written as [167]

$$\Delta E^{\text{sphere}} = \frac{Z\alpha}{2R}\int_0^R \left(\frac{r^2}{R^2} + \frac{2R}{r} - 3\right) |\mathcal{R}_{nl}(r)|^2 \, r^2 \, \mathrm{d}r. \tag{2.21}$$

As the integration is restricted to the small region within the nucleus, one can approximate the radial wave function by its value at the origin. In this case, one obtains [167]

$$\Delta E^{\text{sphere}} \approx Z\alpha \frac{R^2}{10} |\mathcal{R}_{nl}(0)|^2 \tag{2.22}$$

Since only s-states have a nonzero probability density at the origin, the finite nuclear size correction is strongly suppressed for states with orbital angular momentum $l > 0$. Eq. (2.22) reveals that the finite-size correction depends on the squared nuclear radius.

A more realistic approach is the commonly used two-parameter Fermi distribution [173]

$$\varrho(r) = \frac{\rho_0}{1 + \exp\left(\frac{r-c}{a}\right)}, \tag{2.23}$$

where c is the half-density radius, a characterizes the surface thickness, and ρ_0 is a normalization constant. An analytical expression of the resulting nuclear potential can be found in Ref. [173]. The size of the nucleus is typically quantified by the mean square charge radius $\langle r^2 \rangle$, which is related to the charge distribution by

$$\langle r^2 \rangle = \frac{\int \varrho(r) r^2 \mathrm{d}V}{\int \varrho(r) \mathrm{d}V} \tag{2.24}$$

As shown above, the potential of a finite-size nucleus deviates from the one of a pointlike nucleus at small r and thus leads to a shift of the energy levels. The field shift refers to the energy shift of an atomic level due to a change in the nuclear charge distribution between different isotopes. In first-order perturbation theory, the field shift of a state $|a\rangle$ between isotopes A and A' is given by

$$\Delta E_a^{\mathrm{FS}} = \left\langle a \,\middle|\, \Delta V^{AA'} \,\middle|\, a \right\rangle, \tag{2.25}$$

where $\Delta V^{AA'}$ is the difference between the nuclear potentials of the two isotopes. As seen from Eq. (2.22), this effect is primarily governed by the change in the mean square radius, $\delta\langle r^2 \rangle^{AA'} = \langle r^2 \rangle^{A'} - \langle r^2 \rangle^{A}$.

A standard approach in the literature is to define a field shift operator as the derivative of the nuclear potential with respect to the mean square radius [164, 174–176]

$$\mathcal{O}^{\mathrm{FS}} = \frac{\partial V}{\partial \langle r^2 \rangle} \tag{2.26}$$

As shown in Ref. [164] for isotope shift calculations in Ca^+, the difference between evaluating Eq. (2.25) directly and using the operator in Eq. (2.26) is typically a small correction. Using the field shift operator $\mathcal{O}^{\mathrm{FS}}$, the first-order field shift of a state $|a\rangle$ is given by

$$\Delta E_a^{\mathrm{FS}} = \delta\langle r^2 \rangle^{AA'} \left\langle a \,\middle|\, \mathcal{O}^{\mathrm{FS}} \,\middle|\, a \right\rangle, \tag{2.27}$$

and the corresponding shift of a transition i between the states $|a\rangle$ and $|b\rangle$ directly follows as

$$\nu_i^{AA',\mathrm{FS}} = \delta\langle r^2 \rangle^{AA'} \left(\left\langle b \,\middle|\, \mathcal{O}^{\mathrm{FS}} \,\middle|\, b \right\rangle - \left\langle a \,\middle|\, \mathcal{O}^{\mathrm{FS}} \,\middle|\, a \right\rangle \right) \equiv \delta\langle r^2 \rangle^{AA'} F_i. \tag{2.28}$$

Similar to the mass shift, the electronic structure contribution is encoded in the coefficient F_i.

2.1.2 *Higher order Standard Model contributions*

While the leading contributions to isotope shifts are captured by the first-order mass shift and field shift as written in Eqs. (2.15) and (2.28), today's high precision in atomic spectroscopy demands the inclusion of additional contributions. In the following, we provide a brief overview of the most important higher-order effects.

Higher-order mass and field shifts

In the previous section, we discussed the effects of the finite nuclear mass and size, which lead to the mass and field shifts. The first-order results, Eqs. (2.15) and (2.28), scale with the difference of the mean square nuclear radii $\delta\langle r^2\rangle$ for the field shift and with the difference of inverse nuclear masses $1/M_{A'} - 1/M_A$ for the mass shift. However, the corresponding perturbation Hamiltonians can also be treated in higher-order perturbation theory. For instance, the second-order energy shift of a state $|a\rangle$ due to a perturbation H' is given by

$$\Delta E_a^{(2)} = \sum_{n\neq a} \frac{|\langle a\,|\,H'\,|\,n\rangle|^2}{E_a^{(0)} - E_n^{(0)}}. \tag{2.29}$$

For the second-order mass and field shifts, this leads to additional contributions in the form [164]

$$\nu_i^{AA',\mathrm{MS}^{(2)}} = \left(\frac{1}{M_{A'}^2} - \frac{1}{M_A^2}\right) K_i^{(2)} \tag{2.30a}$$

$$\nu_i^{AA',\mathrm{FS}^{(2)}} = \left(\delta\langle r^2\rangle\right)^2 F_i^{(2)}. \tag{2.30b}$$

The quadratic field shift becomes important in heavy systems like ytterbium, while the quadratic mass shift is more relevant in lighter systems like calcium [148, 164, 176]. Moreover, there exists a cross-term involving both field and mass shift effects. According to Ref. [164], this effect can be approximately taken into account through a nuclear mass-dependent modification of the electronic field shift coefficient:

$$F_i \to F_i \left(1 - 3\frac{m_e}{M} + \ldots\right). \tag{2.31}$$

Consequently, the correction to the isotope shift due to this cross term can be written as [164]

$$\nu_i^{AA',\mathrm{FS}\times\mathrm{MS}} \approx -3\left(\frac{m_e}{M_{A'}} - \frac{m_e}{M_A}\right)\delta\langle r^2\rangle F_i. \tag{2.32}$$

Nuclear deformation

So far, we restricted the analysis to spherically symmetric nuclear charge distributions, which only vary in the mean square radius between different isotopes, leading to the conventional field shift discussed above. However, for a more sophisticated analysis, one can take nuclear deformations into account. A nonspherical nucleus can be modeled by a deformed Fermi distribution, as for example [177–179]

$$\varrho(r,\theta) = \frac{\rho_0}{1+\exp\left(\frac{r-c\left(1+\beta_2 Y_2^0(\theta)\right)}{a}\right)}, \tag{2.33}$$

where Y_l^m denotes again spherical harmonics and β_2 describes the deformation of the charge distribution. In addition to the mean square radius, this distribution is characterized by the intrinsic nuclear quadrupole moment [177]

$$Q_0 = Ze\int \left(3\cos^2\theta\right)\varrho(r,\theta)r^2\mathrm{d}V. \tag{2.34}$$

The angle θ is defined with respect to the symmetry axis of the nucleus. Since the nucleus does not possess a fixed orientation in the laboratory frame, this angular dependence is averaged out to obtain an effective spherical symmetric nuclear potential, which is used to evaluate the corrections to the atomic energy levels. A detailed analysis of the effects of such a charge distribution in hydrogen-like ions is provided in Ref. [177]. The deformation can affect the radial moments $\langle r^n\rangle$ of the nuclear distribution. In fact, the analysis of King plot nonlinearities in ytterbium suggests that nuclear deformation is an important effect. In particular, it was shown that changes in higher radial moments, especially $\langle r^4\rangle$, can explain the observed deviations from linearity [150, 180].

Nuclear polarization

Above, we explored the effects of the size and shape of an otherwise static nuclear charge distribution. However, the internal dynamic structure of the nucleus can also affect electronic energy levels. Such effects on the electronic energy levels are known as nuclear polarization. These so-called nuclear polarization effects are theoretically challenging to evaluate and have been addressed in various studies [181–184]. A comprehensive treatment of nuclear polarization in hydrogen-like ions, including corrections beyond the frequently used Coulomb approximation, is provided in Ref. [185]. The Coulomb approximation is based on the assumption that the velocities of nuclear dynamics can be treated nonrelativistically. In the Coulomb approximation, the nuclear polarization correction to the energy of a state $|a\rangle$ is given by [164, 185]

$$\Delta E_{\mathrm{np}}(a) = -\alpha\sum_{\lambda LM} B(EL)_\lambda \sum_n \frac{\left|\langle a|\mathcal{F}_L Y_L^M|n\rangle\right|^2}{E_n - E_a + \mathrm{sgn}(E_n)\omega_\lambda}. \tag{2.35}$$

Here, $B(EL)_\lambda$ denotes the reduced transition probability for an electric multipole of order L from an excited nuclear state $|\lambda\rangle$ to the ground state, and ω_λ is the corresponding transition energy. The $\mathcal{F}_L$ are radial functions, whose explicit form for a solid-sphere nuclear model is given in Refs. [164, 185]. The isotope shift of a state $|a\rangle$ can be parametrized as

$$\Delta E_{\mathrm{np}}\left(a\right)^{AA'} = -F\left(a\right)\left(\langle r^2\rangle^{A'} g_a^{A'} - \langle r^2\rangle^{A} g_a^{A}\right)\cdot 10^{-3}, \tag{2.36}$$

where $F\left(a\right)$ is the electronic first-order field shift coefficient of the state $|a\rangle$ and the coefficients g_a^A depend both on the electronic state as well as on the isotope.

Calculations in Ref. [185] demonstrate that corrections beyond this approximation are non-negligible and should be considered. For many-electron systems, however, it is typically not feasible to go beyond the Coulomb approximation. This makes nuclear polarization effects a challenging systematic in the interpretation of isotope shift measurements, as we will further discuss in Section 2.3.

Hyperfine structure

King plot analyses of isotope shifts usually focus on even-even isotopes with nuclear spin $I = 0$ in order to avoid complications from hyperfine structure. However, as there is only a limited number of stable even isotopes for a given element, also isotopes with nonzero nuclear spin are used in some studies. In fact, an isotope shift analysis in strontium, including three even isotopes and one isotope with nonzero nuclear spin, revealed a nonlinear King plot [186]. The source of this deviation from the linear isotope shift relation was suspected to be the second-order hyperfine shift. Indeed, calculations in Ref. [187] demonstrated that subtracting this contribution from the measured data restored the linearity of the King plot. This confirms that the observed nonlinearity is compatible with hyperfine effects.

2.1.3 *New physics*

In addition to the Standard Model contributions discussed above, isotope shifts can be affected by hypothetical new interactions beyond the Standard Model between the nucleus and the bound electrons. In particular, they are sensitive to potential new bosons that couple to electrons and neutrons inside the nucleus. Since the number of protons remains constant across isotopes, any effects from couplings to protons largely cancel in isotope shift measurements. Examples of such new bosons have been briefly discussed in Section 1.2.3, including the scalar relaxion or new vector bosons arising from gauging the $B - L$ symmetry. In the following, we describe how these new interactions can affect isotope shifts.

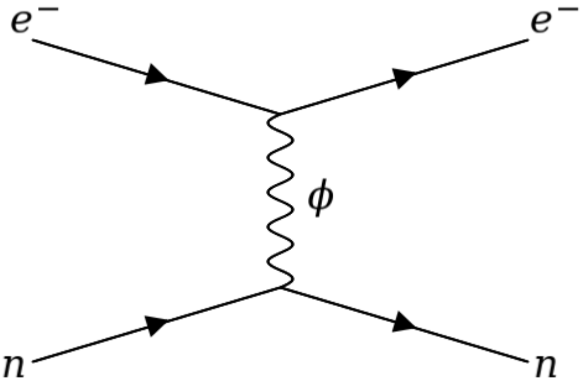

Figure 2.2: Feynman diagram of the the interaction between electrons and neutrons mediated by a new boson ϕ.

The exchange of a new boson ϕ between neutrons and electrons is illustrated in Fig. 2.2. For the case of a scalar boson, the this Feynman diagram leads to the amplitude

$$i\mathcal{M} = \frac{-iy_e y_n}{q^2 - m_\phi^2}\bar{u}_e(p_e')u_e(p_e)\bar{u}_n(p_n')u_n(p_n) \tag{2.37}$$

where y_e and y_n denote the couplings of the boson to electrons and neutrons, respectively. As shown in Ref. [188], this amplitude leads in the nonrelativistic limit to the potential

$$V(\boldsymbol{q}) = \frac{-y_e y_n}{|\boldsymbol{q}|^2 + m_\phi^2} \tag{2.38}$$

Taking the Fourier transform to position space yields the well-known Yukawa potential:

$$V(r) = -\frac{y_e y_n}{4\pi}\frac{e^{-m_\phi r}}{r}. \tag{2.39}$$

A similar calculation for a vector boson results in the same form, but with an overall minus sign due to the boson's spin. Thus, the general form of the potential between an atomic electron and a nucleus, which contains $A - Z$ neutrons, mediated by a new boson can be written as [142, 143, 145, 146]

$$V_{\mathrm{NP}}(r) = \alpha_{\mathrm{NP}}\,(A - Z)\,\frac{e^{-m_\phi r}}{r} \tag{2.40}$$

with the effective coupling

$$\alpha_{\mathrm{NP}} = (-1)^s \frac{y_e y_n}{4\pi}, \tag{2.41}$$

where s is the spin of the mediator boson. The range of the potential is governed by the mass m_ϕ of the boson. In the limit of a massless mediator, the potential becomes Coulomb-like with a $1/r$ dependence. In contrast, for large mediator masses, the interaction becomes short-ranged and approaches a contact interaction. We will explore the dependence on m_ϕ in more detail in Section 2.3.

In first-order perturbation theory, the contribution of such a new interaction to the isotope shift of transition i between atomic states $|a\rangle$ and $|b\rangle$ is given by

$$\nu_i^{AA',\mathrm{NP}} = (A - A') \left(\langle b \,|\, V_{\mathrm{NP}}(r) \,|\, b \rangle - \langle a \,|\, V_{\mathrm{NP}}(r) \,|\, a \rangle \right) \equiv (A - A') X_i. \tag{2.42}$$

As for the mass shift and field shift, the electronic structure contribution is captured in the coefficient X_i.

In the next section, we will introduce the King plot formalism and explore how precision isotope shift measurements can be used to constrain the coupling strength α_{NP}.

2.2 KING PLOT ANALYSIS

Having discussed the various contributions to isotope shifts, we now turn to the question, how experimental isotope shift data can be used to constrain possible new physics couplings. To this end, we present the King plot formalism and examine how effects beyond the first-order mass and field shifts give rise to so-called King nonlinearities. We then review how bounds on α_{NP} can be extracted both in the case of a linear King plot as well as in the more complicated scenario of significant Standard Model nonlinearities. In addition, we discuss the decomposition plot method, which can serve as a powerful tool to distinguish different sources of nonlinearity. Finally, we provide a brief overview of how King plot based constraints on new physics have evolved over the past years. This section is based on the overview provided in Ref. [Ric6].

2.2.1 *The linear King plot*

As discussed in the previous section, the leading contributions to the isotope shift of an atomic transition arise from the first-order field and mass shifts. Hence, by combining Eqs. (2.15) and (2.28) the isotope shift of a transition i can be approximated as

$$\nu_i^{AA'} \approx K_i \left(\frac{1}{M_{A'}} - \frac{1}{M_A} \right) + F_i \delta \langle r^2 \rangle^{AA'} . \tag{2.43}$$

For the following analysis, it is helpful to define the modified isotope shift

$$\tilde{\nu}_i^{AA'} \equiv \nu_i^{AA'} / \delta_M^{AA'} , \quad \text{with} \quad \delta_M^{AA'} \equiv \left(\frac{1}{M_{A'}} - \frac{1}{M_A} \right) . \tag{2.44}$$

One essential property of the first-order expression (2.43) is that both contributions factorize into an electronic structure coefficient, which only depends on the chosen transition, and a nuclear parameter, which depends on the isotope pair. Therefore, when isotope shifts are measured in two different transitions, but in the same isotopes A and A', one can eliminate the change of the mean square radius $\delta\langle r^2\rangle^{AA'}$ and obtain the linear King relation [189]

$$\tilde{\nu}_2^{AA'} = K_{21} + F_{21} \tilde{\nu}_1^{AA'} . \tag{2.45}$$

Here, we defined $F_{21} = F_2/F_1$ and $K_{21} = K_2 - F_{21} K_1$. This relation predicts a linear dependence between the modified isotope shifts in two different transitions. Consequently, when isotope shifts are measured in multiple isotope pairs and the data is plotted with the modified isotope shifts $\tilde{\nu}_1^{AA'}$ on the x-axis and $\tilde{\nu}_2^{AA'}$ on the y-axis, the data points should lie on a straight line within the experimental uncertainties. The slope and the intercept of this line are given by the coefficients F_{21} and K_{21}, respectively. Such an illustration is called a King plot and is sketched in Fig. 2.3. If there is a significant third contribution to the isotope shift, it may shift data points away from this line, giving rise to what is known as King nonlinearity. Since any two points can always be connected by a straight line, at least three different isotope pairs are required to test for linearity. There are different methods to quantify the nonlinearity in experimental data. One simple and intuitive approach is to define a reference line using two data points and then use the perpendicular distance of the third point from this line as a measure of nonlinearity. However, this method depends on the choice of reference points. A more general approach involves fitting a line to all data points and evaluating the deviations of each point from this best-fit line. For this thesis, we use a different method, which, as we will see later, naturally emerges from the algebraic framework to extract α_{NP}. When measurements are available in multiple different isotope pairs, which we denote with a_i, one can rewrite Eq. (2.45) as a vector equation:

$$\tilde{\boldsymbol{\nu}}_2 = K_{21} \mathbf{1} + F_{21} \tilde{\boldsymbol{\nu}}_1 \tag{2.46}$$

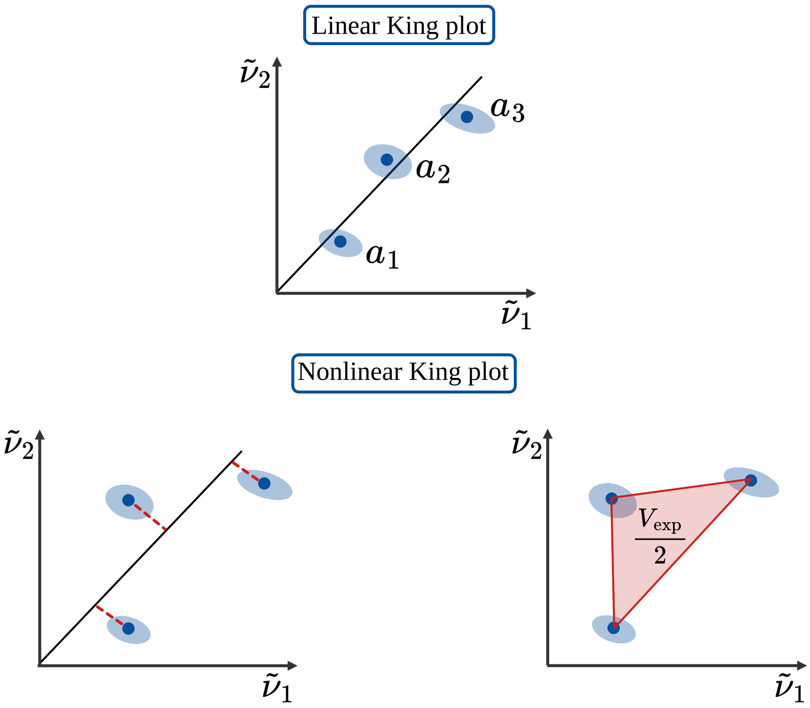

Figure 2.3: Schematic illustration of a King plot in which the modified isotope shifts $\tilde{\nu}_1$ and $\tilde{\nu}_2$ are presented on the x- and y-axis. Every data point in the King plot corresponds to measurements of $\tilde{\nu}_1$ and $\tilde{\nu}_2$ in one isotope pair a_i. In the linear case, when Eq. (2.45) holds, the data points lie on a straight line within the experimental uncertainties, which are shown by the transparent ellipses. Deviations from this linear relation can be quantified by the distance of the data points from a fitted line or by the area of the triangle defined by the data points.

where $\tilde{\boldsymbol{\nu}}_i = (\tilde{\nu}_i^{a_1}, \ldots, \tilde{\nu}_i^{a_n})$ and $\mathbf{1} = (1, \ldots, 1)$ are vectors in the isotope pair space. Their dimension depends on the available number of isotopes n. If the linear King relation holds, the vector $\tilde{\boldsymbol{\nu}}_2$ lies in the plane spanned by the vectors $\tilde{\boldsymbol{\nu}}_1$ and $\mathbf{1}$. In contrast, if there are significant additional contributions, $\tilde{\boldsymbol{\nu}}_2$ might point out of this King plane. In fact, this is the case when $\tilde{\boldsymbol{\nu}}_2$, $\tilde{\boldsymbol{\nu}}_1$ and $\mathbf{1}$ are linearly independent vectors. Therefore, when $n = 3$ isotope pairs are available the determinant of the (3×3)-matrix consisting of the vectors $\tilde{\boldsymbol{\nu}}_2$, $\tilde{\boldsymbol{\nu}}_1$ and $\mathbf{1}$ can be used as a measure of nonlinearity:

$$V_{\text{exp}} = \det\left(\tilde{\boldsymbol{\nu}}_1, \tilde{\boldsymbol{\nu}}_2, \mathbf{1}\right). \tag{2.47}$$

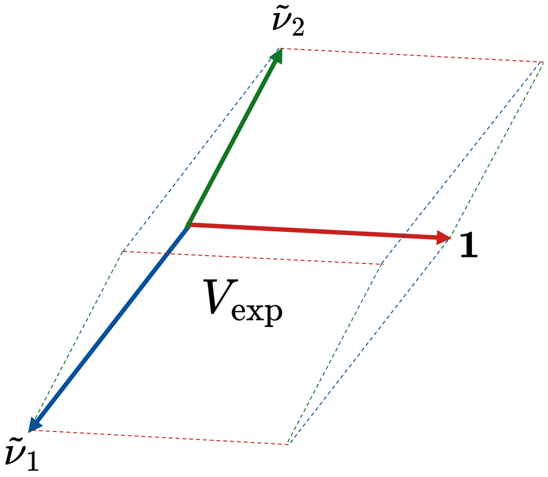

Figure 2.4: Schematic illustration of the King plane, which is spanned by the vectors $\tilde{\boldsymbol{\nu}}_1$ and $\mathbf{1}$. The King plot is nonlinear, if the vector $\tilde{\boldsymbol{\nu}}_2$ points out of this plane. The nonlinearity V_{exp} can be quantified as the volume of the parallelepiped defined by the three vectors.

Geometrically, this corresponds to the volume of the parallelepiped spanned by the three vectors $\tilde{\boldsymbol{\nu}}_1$, $\tilde{\boldsymbol{\nu}}_2$ and $\mathbf{1}$, see Fig. 2.4. Alternatively, $V_{\mathrm{exp}}/2$ can also be interpreted as the area of the triangle which is defined by the three data points in the King plot [143, 164, 190], see Fig. 2.3.

2.2.2 *Constraining new physics with linear King plots*

As discussed in Section 2.1.3, a new boson coupling to electrons and neutrons induces an additional contribution to the isotope shift, such that Eq. (2.43) becomes

$$\nu_i^{AA'} = K_i \left(\frac{1}{M_{A'}} - \frac{1}{M_A} \right) + F_i \delta \langle r^2 \rangle^{AA'} + \alpha_{\mathrm{NP}} X_i \gamma^{AA'}, \tag{2.48}$$

with $\gamma^{AA'} = A' - A$. Consequently, the King relation for the isotope shift in two transitions is modified to

$$\tilde{\nu}_2^{AA'} = K_{21} + F_{21} \tilde{\nu}_1^{AA'} + \alpha_{\mathrm{NP}} X_{21} \tilde{\gamma}^{AA'}, \tag{2.49}$$

with $X_{21} \equiv X_2 - F_{21} X_1$ and $\tilde{\nu}^{AA'} \equiv \gamma^{AA'} / \delta_M^{AA'}$. The last term in Eq. (2.49), which encodes the deviation from the linear King relation due to new physics, may induce

King nonlinearity. Thus, if the experimental data is linear within uncertainties, one can place constraints on the allowed values of the coupling constant α_{NP}. In the following, we review three methods to quantify these constraints.

The minimal King plot

If isotope shift data is available for multiple isotope pairs, Eq. (2.49) again can be written in vector form:

$$\tilde{\boldsymbol{\nu}}_2 = K_{21}\mathbf{1} + F_{21}\tilde{\boldsymbol{\nu}}_1 + \alpha_{\mathrm{NP}} X_{21}\tilde{\boldsymbol{\gamma}}. \tag{2.50}$$

When isotope shifts are measured for three isotope pairs, Eq. (2.50) can be solved for α_{NP} [190]

$$\alpha_{\mathrm{NP}} = \frac{\det\left(\tilde{\boldsymbol{\nu}}_1, \tilde{\boldsymbol{\nu}}_2, \mathbf{1}\right)}{\varepsilon_{ij}\det\left(X_i\tilde{\boldsymbol{\gamma}}, \tilde{\boldsymbol{\nu}}_j, \mathbf{1}\right)}, \tag{2.51}$$

where ε_{ij} denotes the two-dimensional Levi Civita symbol.

We refer to this expression as the “minimal King plot” equation. The numerator of this expression corresponds to the experimentally observed nonlinearity volume V_{exp}, which was introduced earlier, while the denominator can be interpreted as the theoretically predicted nonlinearity volume V_{th} for a coupling of $\alpha_{\mathrm{NP}} = 1$. Hence, the coupling can be expressed as the ratio

$$\alpha_{\mathrm{NP}} = \frac{V_{\mathrm{exp}}}{V_{\mathrm{th}}}. \tag{2.52}$$

Indeed, all methods to constrain α_{NP} that we will discuss in this chapter will follow this general structure, though the expressions for V_{exp} and V_{th} might vary. Another important feature of the minimal King plot equation is the elimination of the electronic coefficients K_{ji} and F_{ji}. Therefore, the only theoretical input that is needed are the electronic new physics coefficients X_i. However, to gain some insight into the behaviour of V_{th}, it is helpful to insert Eq. (2.49) and split V_{th} into an electronic and nuclear part. This yields the expression [190]

$$V_{\mathrm{th}} = (F_1 X_2 - F_2 X_1)\det\left(\tilde{\boldsymbol{\gamma}}, \boldsymbol{\delta}\langle\tilde{\boldsymbol{r}}^{\mathbf{2}}\rangle, \mathbf{1}\right)\,, \tag{2.53}$$

with $\boldsymbol{\delta}\langle\tilde{\boldsymbol{r}}^{\mathbf{2}}\rangle = (\delta\langle r^2\rangle^{a_1}/\delta_M^{a_1}, \delta\langle r^2\rangle^{a_2}/\delta_M^{a_2}, \delta\langle r^2\rangle^{a_3}/\delta_M^{a_3})$. This equation reveals that there are possible alignments in the electronic and in the nuclear part, which would lead to a vanishing nonlinearity volume V_{th}. The nuclear part is only nonzero when the three vectors $\tilde{\boldsymbol{\gamma}}$, $\boldsymbol{\delta}\langle\tilde{\boldsymbol{r}}^{\mathbf{2}}\rangle$ and $\mathbf{1}$ are linearly independent. In the illustration in Fig. 2.4, this would correspond to the new physics contribution pointing out of the plane defined by $\boldsymbol{\tilde{\nu}_1}$ and $\mathbf{1}$. If the vectors are linearly dependent, the new physics contribution can be absorbed into redefinitions of K_i and F_i in Eq. (2.45). The electronic part vanishes when the ratio X_2/X_1 approaches F_2/F_1. As we will discuss further in Section 2.3, this electronic part is crucial for understanding the dependence of the resulting constraints on the mediator mass m_ϕ.

In the case of a linear King plot, which means that the observed nonlinearity V_{exp} is smaller than its uncertainty $\sigma\left[V_{\mathrm{exp}}\right]$, the constraint on α_{NP} is dominated by its uncertainty $\sigma[\alpha_{\mathrm{NP}}]$. This uncertainty arises from the experimental uncertainties in the isotope shift frequencies $\nu_i^{a_i}$ and in the isotope masses, which enter through the modified isotope shifts $\tilde{\nu}_i^{a_i} = \mu^{a_i}\nu_i^{a_i}$, and from the theoretical uncertainty on the electronic new physics coefficients X_i. The evaluation of $\sigma\left[\alpha_{\mathrm{NP}}\right]$ can proceed via linear error propagation

$$\sigma\left[\alpha_{\mathrm{NP}}\right] \approx \sqrt{\sum_{i,a_i}\left(\frac{\partial\alpha_{\mathrm{NP}}}{\partial\nu_i^{a_i}}\sigma\left[\nu_i^{a_i}\right]\right)^2 + \sum_A\left(\frac{\partial\alpha_{\mathrm{NP}}}{\partial M_A}\sigma\left[M_A\right]\right)^2 + \sum_i\left(\frac{\partial\alpha_{\mathrm{NP}}}{\partial X_i}\sigma\left[X_i\right]\right)^2} \tag{2.54}$$

or via a Monte Carlo approach. In the latter case, α_{NP} is sampled by drawing input parameters from normal distributions that reflect the respective uncertainties, and $\sigma[\alpha_{\mathrm{NP}}]$ is taken as the standard deviation of the sampled values. Throughout this thesis, bounds on new physics are presented as 2σ limits: $\alpha_{\mathrm{NP}} \pm 2\sigma[\alpha_{\mathrm{NP}}]$. Moreover, Eq. (2.51) is sensitive to the sign of the preferred value of the coupling α_{NP}. Since even a small V_{exp} yields a nonzero central value of α_{NP}, the bounds for positive and negative α_{NP} will in general differ. However, to be conservative, we always quote the upper bound on the absolute value: $|\alpha_{\mathrm{NP}}| + 2\sigma[\alpha_{\mathrm{NP}}]$.

The no-mass King plot

As discussed above, the uncertainty $\sigma\left[\alpha_{\mathrm{NP}}\right]$ is affected by the experimental uncertainties in the isotope shift frequencies as well as in the isotope masses. When the mass uncertainties are large, they might present a limiting factor for the constraints on α_{NP}. In such cases, it is useful to eliminate the dependence on the isotope masses by including a third electronic transition. Analogous to how the nuclear charge radius differences $\delta\langle r^2\rangle$ were eliminated by using a second transition, a third transition can be used to replace the isotope masses. This leads to the relation [190]

$$\boldsymbol{\nu_3} = f_{31}\boldsymbol{\nu_1} + f_{32}\boldsymbol{\nu_2} + \alpha_{\mathrm{NP}}\left(X_3 - f_{31}X_1 - f_{32}X_2\right)\boldsymbol{\gamma}, \tag{2.55}$$

where the electronic coefficients are defined as

$$f_{31} \equiv \frac{K_3F_2 - K_2F_3}{K_1F_2 - K_2F_1} \quad \text{and} \quad f_{32} \equiv \frac{K_1F_3 - K_3F_1}{K_1F_2 - K_2F_1}. \tag{2.56}$$

Similar to the minimal King plot, one can solve this equation for α_{NP} if measurements are available for three different isotope pairs. The resulting expression for the "no-mass King plot" (NMKP) takes the form

$$\frac{\alpha_{\mathrm{NP}}}{\alpha_{\mathrm{EM}}} = \frac{\det\left(\boldsymbol{\nu_1}, \boldsymbol{\nu_2}, \boldsymbol{\nu_3}\right)}{\frac{1}{2}\varepsilon_{ijk}\det\left(X_i \boldsymbol{\gamma}, \boldsymbol{\nu_j}, \boldsymbol{\nu_k}\right)} . \tag{2.57}$$

Analogous to the minimal King plot case, the numerator corresponds to the volume of the parallelepiped spanned by the three isotope shift vectors $\boldsymbol{\nu_1}$, $\boldsymbol{\nu_2}$ and $\boldsymbol{\nu_3}$, while the denominator is the volume predicted for $\alpha_{\mathrm{NP}} = 1$. The latter one can again be separated into an electronic and a nuclear part

$$V_{\mathrm{th}}^{\mathrm{NMKP}} = \frac{1}{2}\varepsilon_{ijk} K_i F_j X_k \det\Big(\boldsymbol{\delta_M}, \boldsymbol{\delta}\langle \boldsymbol{r^2}\rangle, \boldsymbol{\gamma}\Big) , \tag{2.58}$$

revealing possible alignments of mass shift, field shift and new physics vectors which would lead to a vanishing $V_{\mathrm{th}}^{\mathrm{NMKP}}$.

Projection Method

The equations for the minimal King plot and the no-mass King plot include exactly three isotope pairs. If measurements for even more isotope pairs are available, one can create subsets of the data and perform the analysis for all possible combinations of isotope pairs. An alternative formalism, which includes all isotope pairs simultaneously, is given by the "projection method" (PM) introduced in Ref. [145].

Having isotope shift data for n isotope pairs, such that all the vectors in isotope pair space are n-vectors now, one can define the $(n \times 2)$ matrix

$$D_{\boldsymbol{w}} \equiv \left(\boldsymbol{\tilde{\nu}_1}, \boldsymbol{w}\right) , \tag{2.59}$$

where $\boldsymbol{w}$ is an arbitrary vector in isotope-pair space. This matrix allows to construct the projection of the $\mathbf{1}$-vector onto the plane defined by $\boldsymbol{\tilde{\nu}_1}$ and $\boldsymbol{w}$. This projection is given by

$$\boldsymbol{p_w} = D_{\boldsymbol{w}} \left(D_{\boldsymbol{w}}^{\intercal} D_{\boldsymbol{w}}\right)^{-1} D_{\boldsymbol{w}}^{\intercal} \mathbf{1} . \tag{2.60}$$

Now, one obtains the volume of the parallelepiped spanned by the three vectors $\mathbf{1}$, $\boldsymbol{\tilde{\nu}_1}$ and $\boldsymbol{w}$ as

$$V^{\mathrm{PM}}\left(\mathbf{1}, \boldsymbol{\tilde{\nu}_1}, \boldsymbol{w}\right) = |\mathbf{1} - \boldsymbol{p_w}| \sqrt{|\boldsymbol{\tilde{\nu}_1}|^2 |\boldsymbol{w}|^2 - \left(\boldsymbol{\tilde{\nu}_1} \cdot \boldsymbol{w}\right)^2} . \tag{2.61}$$

With this, the new physics coupling α_{NP} can be written as

$$|\alpha_{\mathrm{NP}}| = \frac{V^{\mathrm{PM}}\left(\mathbf{1}, \boldsymbol{\tilde{\nu}_1}, \boldsymbol{\tilde{\nu}_2}\right)}{|X_{21}| V^{\mathrm{PM}}\left(\mathbf{1}, \boldsymbol{\tilde{\nu}_1}, \boldsymbol{\tilde{\gamma}}\right)} . \tag{2.62}$$

In the special case of three isotope pairs, this expression becomes equivalent to the minimal King Plot approach described earlier in Eq.(2.51), with the caveat that the magnitude of α_{NP} is obtained, but not its sign.

2.2.3 *The nonlinear King plot*

In the previous section, we discussed how constraints on a possible new physics coupling α_{NP} can be extracted from isotope shift data, under the assumption that the data are consistent with the linear King relation. However, we have not yet addressed how to proceed when the King plot exhibits a significant deviation from linearity, that is, when one finds $V_{\mathrm{exp}} > \sigma\left[V_{\mathrm{exp}}\right]$. While it might be tempting to interpret such a nonlinearity as direct evidence for the existence of a new boson, this conclusion would be too hasty, as there are also Standard Model effects that can cause nonlinearities. We have already encountered some of these additional effects in Section 2.1.

In the presence of several possible sources of nonlinearity, the isotope shift of the transition i can be expressed in the form [190]

$$\boldsymbol{\nu_i} = K_i \boldsymbol{\delta_M} + F_i \boldsymbol{\delta \langle r^2 \rangle} + \sum_l G_{i,l} \boldsymbol{\eta}_l . \tag{2.63}$$

where the first two terms correspond to the first-order mass and field shifts, as before. The final sum includes all additional contributions. Each term in this sum is assumed to factorize into an electronic coefficient $G_{i,l}$ and a nuclear parameter $\boldsymbol{\eta}_l$. In the following, we refer to these as “nonlinear terms”. While this factorization is valid for the higher-order mass and field shifts, this is not necessarily the case for every isotope shift contribution. For instance, the nuclear polarization shift cannot, in general, be expressed in such a simple form. Nevertheless, any isotope shift contribution can always be decomposed into a sum of factorizable components, even if, in the worst case, one must introduce a separate term for each isotope pair. In the following, we address the question of how to identify the dominant sources of nonlinearity in a given dataset.

The Nonlinearity Decomposition

The decomposition plot is a powerful tool to analyze the observed nonlinearity in isotope shift data and to distinguish between different possible sources of nonlinearity. The first concept of this approach was presented in Ref. [148]. The key idea is to study the pattern of deviations of the data points from the best-fit line in the King plot and compare these deviations to the patterns expected from known sources of nonlinearity.

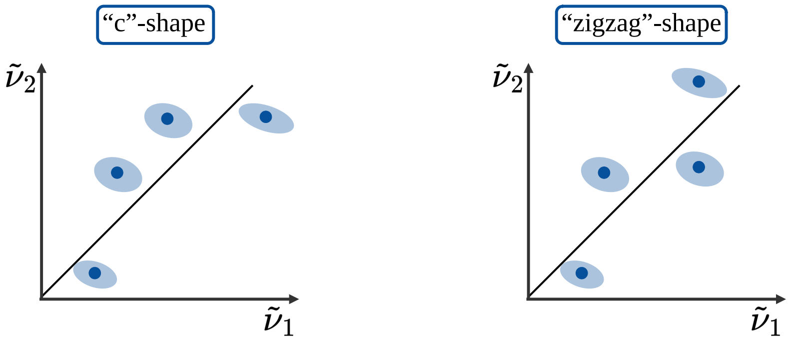

Figure 2.5: Schematic illustration of the decomposition plot method introduced in Ref. [148]. Every pattern of deviations from the best-fit line can be decomposed into combinations of a "c"-shape and a "zigzag"-shape. Analysing these nonlinearity patterns helps to distinguish different sources of nonlinearity.

For four isotope pairs, any deviation from linearity in the King plot can be decomposed into two orthogonal components: a "c"-shaped and a "zigzag"-shaped pattern, which form a basis for all possible nonlinear patterns, see Fig. 2.5. This idea was further developed in a more algebraic framework in Ref. [149]. If measurements are available for four isotope pairs, the King relation with an arbitrary nonlinearity can be written as

$$\tilde{\boldsymbol{\nu}}_{\mathbf{2}} = K_{21}\mathbf{1} + F_{21}\tilde{\boldsymbol{\nu}}_{\mathbf{1}} + \lambda_{21}^{+}\boldsymbol{\Lambda}^{+} + \lambda_{21}^{-}\boldsymbol{\Lambda}^{-}, \tag{2.64}$$

where we choose $\boldsymbol{\Lambda}^{+}$ and $\boldsymbol{\Lambda}^{-}$ as two linearly independent vectors which point out of the King plane defined by $\tilde{\boldsymbol{\nu}}_{\mathbf{1}}$ and $\mathbf{1}$. Therefore, the vectors $\boldsymbol{\Lambda}^{+}$ and $\boldsymbol{\Lambda}^{-}$ span the space of vectors deviating from the King plane. Thus, if there is any nonlinear contribution to the isotope shift data, it can be decomposed into its projections on these two basis vectors. One can define the basis vectors orthogonal to $\tilde{\boldsymbol{\nu}}_{\mathbf{1}}$ and $\mathbf{1}$ as

$$\boldsymbol{\Lambda}^{+} \sim \left(\tilde{\nu}_1^{a_3} - \tilde{\nu}_1^{a_2}, \tilde{\nu}_1^{a_1} - \tilde{\nu}_1^{a_4}, \tilde{\nu}_1^{a_4} - \tilde{\nu}_1^{a_1}, \tilde{\nu}_1^{a_2} - \tilde{\nu}_1^{a_3}\right) , \tag{2.65a}$$

$$\boldsymbol{\Lambda}^{-} \sim \left(\tilde{\nu}_1^{a_4} - \tilde{\nu}_1^{a_2}, \tilde{\nu}_1^{a_1} - \tilde{\nu}_1^{a_3}, \tilde{\nu}_1^{a_2} - \tilde{\nu}_1^{a_4}, \tilde{\nu}_1^{a_3} - \tilde{\nu}_1^{a_1}\right) . \tag{2.65b}$$

These basis vectors now take the role of the c-shaped and zigzag-shaped deviation patterns, in which the total nonlinearity can be decomposed. The coefficients $\lambda_{21}^{\pm}$ for the nonlinearity in the experimental data can be calculated as

$$\begin{pmatrix} \lambda_{21}^{+} \\ \lambda_{21}^{-} \end{pmatrix} = \left(\boldsymbol{L}^{\intercal}\boldsymbol{L}\right)^{-1}\boldsymbol{L}^{\intercal}\tilde{\boldsymbol{\nu}}_{\mathbf{2}\perp} \, , \tag{2.66}$$

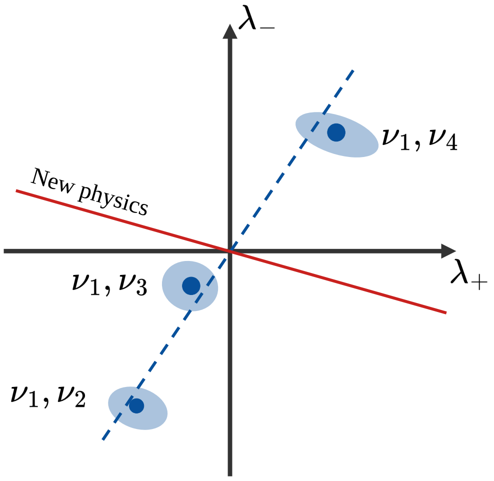

Figure 2.6: Schematic illustration of a decomposition plot. The experimentally observed nonlinearity can be decomposed into its components $\lambda_\pm$ along the basis vectors $\boldsymbol{\Lambda}_\pm$, see Eq. (2.64). Each data point in the two-dimensional decomposition plot corresponds to the isotope shift measurement of one pair of transitions in four isotope pairs. The nonlinearity induced by a nonlinear term, which is factorizable into nuclear and electronic parts, corresponds to a line through the origin. If the experimental points do not lie on the line induced by new physics, the observed nonlinearity cannot solely be explained by the presence of a new boson. When the experimental points approximately lie on the fitted dashed line, the observed nonlinearity likely stems from a single nonlinear term with a corresponding nuclear dependence.

where we define the (4×2) matrix $L \equiv (\boldsymbol{\Lambda}^+, \boldsymbol{\Lambda}^-)$ and $\tilde{\boldsymbol{\nu}}_{\mathbf{2}\perp}$ denotes the projection of $\tilde{\boldsymbol{\nu}}_{\mathbf{2}}$ orthogonal to the King plane. Since the basis vectors $\boldsymbol{\Lambda}^\pm$ are constructed to be orthogonal to the King plane, we can replace $\tilde{\boldsymbol{\nu}}_{\mathbf{2}\perp}$ with $\tilde{\boldsymbol{\nu}}_{\mathbf{2}}$ and write

$$\begin{pmatrix} \lambda_{21}^+ \\ \lambda_{21}^- \end{pmatrix} = (\boldsymbol{L}^\intercal \boldsymbol{L})^{-1} \boldsymbol{L}^\intercal \tilde{\boldsymbol{\nu}}_{\mathbf{2}} \,, \tag{2.67}$$

The obtained coefficients $\lambda_{21}^\pm$ characterize the shape and size of the nonlinearity and define a point in the two-dimensional decomposition plot, see Fig. 2.6. In the case of a linear King plot, the obtained (λ^+, λ^-)-point should coincide with the origin within the experimental uncertainties. This decomposed nonlinearity can be compared to the nonlinearity expected from a specific isotope shift contribution, by replacing $\tilde{\boldsymbol{\nu}}_{\mathbf{2}}$ in Eq. (2.67) with the corresponding vector of this contribution. In particular, if a contribution can be factorized into an electronic and a nuclear part, the decomposition coefficients become

$$\begin{pmatrix}\lambda_{21}^{+}\\ \lambda_{21}^{-}\end{pmatrix} = G_{21}(\boldsymbol{L}^{\intercal}\boldsymbol{L})^{-1}\boldsymbol{L}^{\intercal}\tilde{\boldsymbol{\eta}}\,. \tag{2.68}$$

In this case, the ratio λ^{-}/λ^{+} depends only on the nuclear parameter $\tilde{\boldsymbol{\eta}}$, but not on the electronic coefficient G_{21}. Therefore, any factorizable source of nonlinearity corresponds to a line through the origin in the decomposition plot, with its slope $\frac{\lambda^{-}}{\lambda^{+}}$ set by the isotope dependence of the contribution. Therefore, one can test whether the observed nonlinearity is compatible with a specific effect, even without knowing the electronic structure in detail. For example, if the experimental point does not lie on the line associated with the new physics vector $\tilde{\boldsymbol{\gamma}}$, the observed nonlinearity cannot be attributed to the presence of a new boson alone, and other Standard Model contributions must be considered.

Additional transitions $\tilde{\boldsymbol{\nu}}_{\boldsymbol{j}}$ can be included by computing their corresponding coordinates in the decomposition plot by replacing $\tilde{\boldsymbol{\nu}}_{\boldsymbol{2}}$ with $\tilde{\boldsymbol{\nu}}_{\boldsymbol{j}}$ in Eq. (2.67) to obtain additional experimental points in the same decomposition plot. This has proven particularly useful in the case of nonlinear King plots in ytterbium, where multiple transitions yielded points lying approximately along a common line through the origin. This suggested a dominant source of nonlinearity with a specific isotope dependence, which was identified as a contribution proportional to $\delta\langle r^4\rangle$ [149, 150].

When more isotope pairs are included in the analysis, the vector space orthogonal to the King plane increases in dimension, and Eq. (2.64) can be generalized for the case of n isotope pairs:

$$\tilde{\boldsymbol{\nu}}_{\boldsymbol{2}} = K_{21}\mathbf{1} + F_{21}\tilde{\boldsymbol{\nu}}_{\boldsymbol{1}} + \lambda_{21}^{(1)}\boldsymbol{\Lambda}^{\boldsymbol{(1)}} + \cdots + \lambda_{21}^{(n-2)}\boldsymbol{\Lambda}^{\boldsymbol{(n-2)}}, \tag{2.69}$$

In this case, Eq. (2.67) can still be used with the $(n \times (n-2))$-matrix $L = \left(\boldsymbol{\Lambda}^{\boldsymbol{(1)}}, \ldots, \boldsymbol{\Lambda}^{\boldsymbol{(n-2)}}\right)$ and the vector $\left(\lambda_{21}^{(1)}, \ldots, \lambda_{21}^{(n-2)}\right)$. Such a higher-dimensional decomposition analysis can be advantageous when different sources of nonlinearity are aligned in the two-dimensional decomposition plot and thus can not be distinguished. Adding another isotope pair, and therefore another dimension to the decomposition space, may help resolve these contributions.

2.2.4 *Constraining new physics with nonlinear King plots*

Having discussed the decomposition plot as a tool to gain understanding of the origin of an observed nonlinearity, the question remains whether it is still possible to extract constraints on α_{NP} from a nonlinear King plot.

If the source of the nonlinearity is known and can be calculated with sufficient accuracy, a natural strategy is to subtract the theoretical prediction of this contribution from the experimental data. This leads to the expression

$$(\tilde{\boldsymbol{\nu}}_{\mathbf{2}} - G_2\tilde{\boldsymbol{\eta}}) = K_{21}\mathbf{1} + F_{21}\left(\tilde{\boldsymbol{\nu}}_{\mathbf{1}} - G_1\tilde{\boldsymbol{\eta}}\right) + \alpha_{\mathrm{NP}}X_{21}\tilde{\boldsymbol{\gamma}}. \tag{2.70}$$

Now, one can simply apply the methods presented in Section 2.2.2 with the substitution $\tilde{\boldsymbol{\nu}}_{\boldsymbol{i}} \to (\tilde{\boldsymbol{\nu}}_{\boldsymbol{i}} - G_i\tilde{\boldsymbol{\eta}})$. In this case, the uncertainties of the electronic coefficients G_i and the nuclear parameters η^{a_i} must be properly included in the estimation of $\sigma\left[\alpha_{\mathrm{NP}}\right]$. We will return to such an approach in Section 2.3, where it will be particularly important to account for the second-order mass shift. Before doing so, however, we explore an alternative method to remove nonlinearities without relying on additional theoretical input.

The generalized King plot

In the following, we present a generalization of the minimal King plot method to incorporate additional nonlinear terms, which was introduced in Ref. [190]. We start with the case of only one significant nonlinear term. Including this contribution along with the new physics term, the isotope shift of transition i can be written as

$$\tilde{\boldsymbol{\nu}}_{\boldsymbol{i}} = K_i\mathbf{1} + F_i\boldsymbol{\delta}\langle\widetilde{\boldsymbol{r}^{\mathbf{2}}}\rangle + G_i\tilde{\boldsymbol{\eta}} + \alpha_{\mathrm{NP}}X_i\tilde{\boldsymbol{\gamma}}. \tag{2.71}$$

As for the minimal King plot, we use a second transition to eliminate $\delta\langle r^2\rangle^{a_i}$ and obtain

$$\tilde{\boldsymbol{\nu}}_{\mathbf{2}} = K_{21}\mathbf{1} + F_{21}\tilde{\boldsymbol{\nu}}_{\mathbf{1}} + G_{21}\tilde{\boldsymbol{\eta}} + \alpha_{\mathrm{NP}}X_{21}\tilde{\boldsymbol{\gamma}}, \tag{2.72}$$

with $G_{21} = G_2 - F_{21}G_1$. In the same way, a third transition can be used to replace η^{a_i}, yielding

$$\tilde{\boldsymbol{\nu}}_{\mathbf{3}} = K_{321} + F_{321}\tilde{\boldsymbol{\nu}}_{\mathbf{1}} + G_{321}\tilde{\boldsymbol{\nu}}_{\mathbf{2}} + \alpha_{\mathrm{NP}}X_{321}\tilde{\boldsymbol{\gamma}}\,. \tag{2.73}$$

Here, the more complicated electronic coefficients are defined as [149]

$$G_{321} \equiv G_{31}/G_{21}, \tag{2.74a}$$

$$F_{321} \equiv G_{32}/G_{12}, \tag{2.74b}$$

$$K_{321} \equiv K_{31} - G_{321}K_{21}, \tag{2.74c}$$

$$X_{321} \equiv X_{31} - G_{321}X_{21}. \tag{2.74d}$$

Having one additional electronic coefficient G_{321} compared to the minimal King plot, also one additional isotope pair is needed to extract constraints on α_{NP}. This also intuitively follows from geometrical considerations. In the minimal King plot, two data points define a straight line and a third data point can be used to probe deviations from this line. This idea can be promoted to a higher dimension, in which three data points are needed to define a plane while the fourth data point can be used to search for deviations from planarity. Assuming data for four isotope pairs are available, one can solve Eq. (2.73) for α_{NP} and obtain [190]

$$\alpha_{\mathrm{NP}} = \frac{\det\left(\tilde{\boldsymbol{\nu}}_{\mathbf{1}}, \tilde{\boldsymbol{\nu}}_{\mathbf{2}}, \tilde{\boldsymbol{\nu}}_{\mathbf{3}}, \mathbf{1}\right)}{\frac{1}{2}\varepsilon_{i_1,i_2,i_3}\det\left(X_{i_1}\tilde{\boldsymbol{\gamma}}, \tilde{\boldsymbol{\nu}}_{\boldsymbol{i_2}}, \tilde{\boldsymbol{\nu}}_{\boldsymbol{i_3}}, \mathbf{1}\right)}\,. \tag{2.75}$$

The resulting expression follows a similar structure as the minimal King plot and can again be interpreted as the ratio of the nonlinearity volume found in the experimental data and the one theoretically predicted for $\alpha_{\mathrm{NP}} = 1$. The same procedure of eliminating additional nonlinear terms can be repeated by including more transitions and the corresponding number of isotope pairs. For n isotope pairs and $n-1$ transitions, one obtains the general expression

$$\alpha_{\mathrm{NP}} = \frac{V_{\mathrm{exp}}^{\mathrm{GKP}}}{V_{\mathrm{th}}^{\mathrm{GKP}}} = \frac{\det\left(\tilde{\boldsymbol{\nu}}_{\mathbf{1}}, \ldots, \tilde{\boldsymbol{\nu}}_{\boldsymbol{n-1}}, \mathbf{1}\right)}{\frac{1}{(n-2)!}\varepsilon_{i_1 \ldots i_{n-1}}\det\left(X_{i_1}\tilde{\gamma}, \tilde{\boldsymbol{\nu}}_{\boldsymbol{i_2}}, \ldots, \tilde{\boldsymbol{\nu}}_{\boldsymbol{i_{n-1}}}, \mathbf{1}\right)}\,. \tag{2.76}$$

For $n = 3$ isotope pairs, this formula reproduces the minimal King plot equation. Hence, this method is referred to as the "generalized King plot" (GKP). In summary, the GKP allows us to account for $n-3$ nonlinear terms when n isotope pairs and $n-1$ transitions are available. If all significant nonlinear contributions are taken into account and the resulting generalized King plot is consistent with linearity, such that $V_{\mathrm{exp}}^{\mathrm{GKP}} < \sigma\left[V_{\mathrm{exp}}^{\mathrm{GKP}}\right]$, then 2σ-bounds on α_{NP} can be derived by estimating the uncertainty $\sigma\left[\alpha_{\mathrm{NP}}\right]$ as described in Section 2.2.2.

The no-mass generalized King plot

As discussed in Section 2.2.2, when the uncertainty in the isotope masses limits the resulting constraints on α_{NP}, the no-mass King plot offers a solution by eliminating the dependence on nuclear masses through the use of an additional transition. This idea can also be extended to the generalized King plot [190]. In this case, the "no-mass generalized King plot" (NMGKP) requires n isotope pairs and n transitions to simultaneously eliminate the nuclear masses as well as $n-3$ nonlinear terms. The resulting vector equation can again be solved for α_{NP}, yielding [Ric6]

$$\frac{\alpha_{\mathrm{NP}}}{\alpha_{\mathrm{EM}}} = \frac{V_{\mathrm{exp}}^{\mathrm{NMGKP}}}{V_{\mathrm{th}}^{\mathrm{NMGKP}}} = \frac{\det\left(\tilde{\boldsymbol{\nu}}_{\mathbf{1}}, \tilde{\boldsymbol{\nu}}_{\mathbf{2}}, \ldots, \tilde{\boldsymbol{\nu}}_{\boldsymbol{n}}\right)}{\frac{1}{(n-1)!}\varepsilon_{i_1,i_2,\ldots,i_n}\det\left(X_{i_1}\boldsymbol{\gamma}, \tilde{\boldsymbol{\nu}}_{\boldsymbol{i_2}}, \ldots, \tilde{\boldsymbol{\nu}}_{\boldsymbol{i_n}}\right)}\,. \tag{2.77}$$

The nuclear-input King plot

Finally, we consider the scenario in which the dominant source of nonlinearity is identified and its associated nuclear parameter is known with sufficient precision. A notable example is the second-order mass shift, which is expected to be a leading nonlinear contribution in lighter atomic systems. Its nuclear parameter is given by the difference of squared inverse nuclear masses,

$$\delta_M^{AA'(2)} = \frac{1}{M_A'^2} - \frac{1}{M_A^2}. \tag{2.78}$$

Since the nuclear masses are already required for constructing the minimal King plot, the parameter $\delta_M^{AA'(2)}$ is automatically known with high accuracy. In this case, the second-order mass shift can be explicitly included in the King relation, yielding

$$\tilde{\boldsymbol{\nu}}_{\mathbf{2}} = K_{21}\mathbf{1} + F_{21}\tilde{\boldsymbol{\nu}}_{\mathbf{1}} + \alpha_{\mathrm{NP}} X_{21}\tilde{\boldsymbol{\gamma}} + K_{21}^{(2)}\tilde{\boldsymbol{\delta}}_{\boldsymbol{M}}^{\mathbf{(2)}}. \tag{2.79}$$

Assuming measurements in four isotopes are available, we can solve this expression for α_{NP} and obtain the equation for the “nuclear-input King Plot” [Ric6]

$$\alpha_{\mathrm{NP}} = \frac{\det\left(\tilde{\boldsymbol{\nu}}_1, \tilde{\boldsymbol{\nu}}_2, \tilde{\boldsymbol{\delta}}_{\boldsymbol{M}}^{\mathbf{(2)}}, \mathbf{1}\right)}{\varepsilon_{ij}\det\left(X_i\tilde{\boldsymbol{\gamma}}, \tilde{\boldsymbol{\nu}}_j, \tilde{\boldsymbol{\delta}}_{\boldsymbol{M}}^{\mathbf{(2)}}, \mathbf{1}\right)}, \tag{2.80}$$

This equation presents the advantage that one nonlinear term can be taken into account without adding a third transition to the analysis.

2.2.5 *Existing constraints on new physics*

Before presenting the results of the first King plot analysis, including a HCI, which form the main result of this chapter, we give a brief overview of some existing bounds on α_{NP}. These constraints are illustrated in the exclusion plot in Fig. 2.7.

The three black lines represent limits from previous King plot analyses in Ca^+. The upper line corresponds to the first-ever King-plot-based bound on new physics from Ref. [143]. In that analysis, the ${}^2S_{1/2} \rightarrow {}^2P_{1/2}$ and ${}^2D_{3/2} \rightarrow {}^2P_{1/2}$ transitions were used, which were both measured with an uncertainty below 100 keV [191]. These bounds were later significantly improved by using the narrow ${}^2S_{1/2} \rightarrow {}^2D_{5/2}$ and ${}^2D_{3/2} \rightarrow {}^2D_{5/2}$ transitions, measured with and uncertainty of about 20 Hz [145]. A further improvement came from remeasuring these transitions with an uncertainty of roughly 8 Hz, which tightened the resulting constraints on α_{NP} [146]. Despite the rapid increase in experimental precision, all Ca^+ King plots remained linear.

In contrast, King plot analyses in ytterbium have revealed a notable King nonlinearity. The first such King nonlinearity was observed using the ${}^2S_{1/2} \rightarrow {}^2D_{3/2}$ and ${}^2S_{1/2} \rightarrow {}^2D_{5/2}$ transitions in Yb$^+$, which were measured with an uncertainty of about 300 Hz [148]. This discovery was followed by additional isotope shift measurements of the ${}^2S_{1/2} \rightarrow {}^2F_{7/2}$ transition in Yb$^+$ [149, 150] as well as the ${}^1S_0 \rightarrow {}^3P_0$ and ${}^1S_0 \rightarrow {}^1D_2$ transitions in neutral Yb [147, 151]. This large set of available transitions allowed a thorough decomposition plot analysis, which identified the dominant nonlinear term to be proportional to $\delta\langle r^4\rangle$. By performing a generalized King plot analysis, it was possible to extract constraints on α_{NP} despite such nonlinearity. In Fig. 2.7, we show only the most recent ytterbium bound from Ref. [150], indicated by the blue line.

A different type of constraint, which is also based on isotope shift measurements, is shown by the green solid and dashed lines. These bounds result from comparing the measured isotope shift of the $1s_{1/2} \rightarrow 2s_{1/2}$ transition in hydrogen and deuterium with theoretical predictions. The theory calculations use nuclear radii inferred from Lamb shift measurements in muonic atoms. Since these values would be affected by the coupling of the new boson to muons, this has to be taken into account when evaluating the bounds on α_{NP}. Assuming zero coupling to muons, $y_\mu = 0$, the resulting constraint is shown by the purple dashed line [192]. By relaxing this assumption to $-y_e < y_\mu < 100 y_e$, the resulting bounds are weakened and shown by the purple solid line [193].

An additional laboratory bound, which still remains stronger than those extracted from King plot analyses, is shown by the blue shaded region. This constraint results from a combination of $(g-2)_e$ measurements [46], which constrain y_e, and neutron scattering experiments [194–196], which constrain y_n. The other shaded regions present constraints from stellar cooling [198, 199], from observations of the supernova SN1987A [197] and from fifth force searches via Casimir effect experiments [200, 201]. Finally, the black cross denotes the preferred region for a new protophobic vector boson to explain the beryllium anomaly [158].

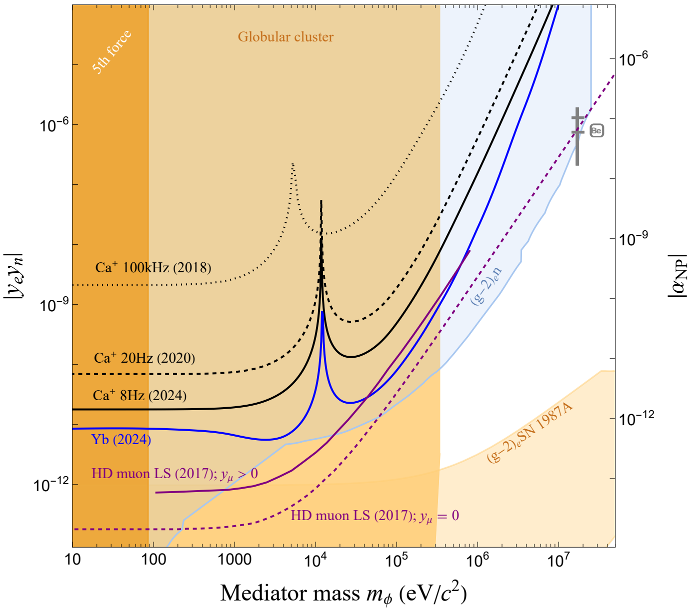

Figure 2.7: Bounds on the coupling of a hypothetical new boson to electrons and neutrons. The bounds are shown in terms of $y_e y_n$ as well as in terms of $\alpha_{\mathrm{NP}} = y_e y_n/(4\pi)$. The dotted black, dashes and solid black lines show constraints resulting from previous King plot analyses in Ca$^+$ [143, 145, 146]. The blue line depicts the most recent constraints from King plot analyses in Yb and Yb$^+$ [150]. The purple dashed and solid lines show constraints from experimental and theoretical isotope shift determinations in H and D. For the theoretical calculations, values of the nuclear charge radius are taken from Lamb shift (LS) measurements in muonic atoms. The dashed line assumes zero coupling of the new boson to muons [192], while the assumption $-y_e < y_\mu < 100 y_e$ results in the weaker solid line [193]. Moreover, the blue shaded region shows a combination of constraints on y_e from $(g-2)_e$ measurements [46] and constraints on y_n from neutron scattering experiments [194–196]. The orange shaded regions show bounds from fifth force searches via Casimir effect experiments [200, 201] and astrophysical bounds from observations of the supernova SN 1987A and Stellar cooling [197–199]. Finally, the black cross shows the favoured region of the protophobic model to explain the beryllium anomaly [158]. Figure adapted from Ref. [Ric4]

2.3 RESULTS I: KING PLOT ANALYSIS IN SINGLY CHARGED AND HIGHLY CHARGED CALCIUM

The final section of this chapter presents the results of a new King plot analysis using transitions in singly charged Ca^{+} and highly charged Ca^{14+} ions from Ref. [Ric4]. This study forms one of the main results of this thesis. In this work, new isotope shift measurements of the ν_{729}: ${}^2S_{1/2} \to {}^2D_{5/2}$ transition in Ca^{+} and the ν_{570}: ${}^3P_0 \to {}^3P_1$ transition in Ca^{14+} were performed with uncertainties below 1 Hz in the calcium isotopes with $A = 40, 42, 44, 46, 48$. These results were combined with new nuclear mass ratio measurements with a relative uncertainty smaller than 10^{-11}. We show the values of the newly measured data in Tables 2.1 and 2.2.

The contributions of this thesis focus on the analysis of the sensitivity of the selected transitions to new physics, presented in Section 2.3.1, including the calculation of the relevant electronic coefficients X_i. Moreover, we analyze the observed nonlinearity and perform a decomposition analysis to explore different sources of nonlinearity. Finally, we discuss how the most stringent King-plot-based bounds on new physics are obtained from a generalized King plot analysis by including the ν_{DD}: ${}^2D_{3/2} \to {}^2D_{5/2}$ transition.

A	ν_{570}	ν_{729}	ν_{DD}
42	539 088 421.24(12)	2 771 872 430.217(27)	-3 519 944.6(60)[a]
44	1 030 447 731.64(11)	5 340 887 395.288(38)	-6 792 440.1(59)[a]
46	1 481 135 946.74(14)	7 768 401 432.916(63)	-9 901 524(21)[b]
48	1 894 297 294.53(14)	9 990 382 526.834(55)	-12 746 588.2(57)[a]

[a] Calculated using $\delta\nu_{729}$ from Ref. [Ric4] and $\delta\nu_{732}$ from Ref. [146].

[b] Taken from Ref. [145].

Table 2.1: Isotope shift frequencies and their uncertainties in parentheses taken from Ref. [Ric4]. The isotope shift of the ${}^3P_0 \to {}^3P_1$ transition in Ca^{14+} is denoted as ν_{570}, while the IS of the ${}^2S_{1/2} \to^2 D_{5/2}$ and ${}^2D_{3/2} \to^2 D_{5/2}$ in Ca^{+} as ν_{729} and ν_{DD}, respectively. The reference isotope is $A = 40$.

A	$R_{AA'}$
42	1.049 961 066 498(15)
44	1.099 943 105 797(15)
46	1.149 958 773 895(30)
48	1.199 990 087 090(40)

Table 2.2: Nuclear mass ratios $R_{AA'}$ and their uncertainties in parentheses taken from Ref. [Ric4]. The reference isotope is $A = 40$.

2.3.1 *Sensitivity to new physics*

Before we analyze the experimental results, we explore the sensitivity of the measured transitions to a hypothetical new boson. As discussed in Section 2.2.2, extracting α_{NP} from isotope shift data requires the calculation of the electronic new physics coefficients X_i for the considered transitions. Moreover, the amount of nonlinearity induced by new physics depends on the expression $(F_2X_1 - F_1X_2)$, see Eq. (2.53). To be able to extract bounds on α_{NP} and to gain understanding of the expected dependence of the bounds on the mediator mass m_ϕ, we calculate the electronic coefficients X_i and F_i for the relevant transitions in Ca$^+$ and Ca^{14+}.

Electronic coefficients X_i of beyond-Standard-Model physics contribution

In this Section, we describe the calculation of the electronic coefficients X_i and F_i. For this purpose, we follow the same approach as in Refs. [143, 164]. In this method, the new physics potential from Eq. (2.40) is directly added to the Dirac equation in the many-body electronic structure calculations. By performing multiple calculations while varying the value of α_{NP}, the new physics coefficient of the transition i can be extracted as the derivative of the transition energy E_i with respect to α_{NP}

$$X_i = \frac{1}{A-Z} \frac{\partial E_i}{\partial \alpha_{\mathrm{NP}}}\bigg|_{\alpha_{\mathrm{NP}}=0} . \tag{2.81}$$

Similarly, the field shift coefficient can be evaluated by varying the mean square radius of the nuclear charge distribution and taking the derivative of the transition energy with respect to $\delta\langle r^2\rangle$:

$$F_i = \frac{\partial E_i}{\partial \delta\langle r^2\rangle}\bigg|_{\delta\langle r^2\rangle=0} . \tag{2.82}$$

The electronic structure calculations are performed by using a combination of configuration interaction (CI) and many-body perturbation theory (MBPT), as it is implemented in the AMBiT code [203]. In the following, we give a brief overview of the theoretical framework implemented in AMBiT and the specific parameters used for the calculations in Ca^{+} and Ca^{14+}.

CI+MBPT calculations with AMBiT

The basic theory of CI+MBPT calculations, as well as its implementation in the AMBiT code, are thoroughly explained in Refs. [203–206].

The first step in such calculations is the generation of a basis of one-electron orbitals $\psi_{n\kappa m_j}(r)$. For this purpose, a Dirac-Fock calculation is performed for a given electronic configuration. This calculation can include all electrons of the ion or only a subset. For instance, it is common to exclude the valence electrons from this procedure. From these calculations, one obtains the one-electron radial wave functions of the Dirac-Fock core. The other basis orbitals, namely the remaining valence orbitals and additional excited virtual orbitals, are obtained as B-spline solutions of the Dirac-Fock Hamiltonian H_{DF}. B-splines are non-negative piecewise polynomial functions with compact support, which can be used to construct a finite basis set in which the Hamiltonian can be diagonalized. Further details about the explicit form of B-splines and their usage for solving the radial Schrödinger and Dirac equations are given in Refs. [207, 208]. Corrections due to finite nuclear size, nuclear recoil, the Breit interaction and QED can be included through modifications of H_{DF}.

In the next step, configuration state functions (CSFs) Φ_k are constructed from antisymmetrized products of one-electron orbitals as eigenfunctions of the angular momentum operators J^2 and J_z. The atomic state wavefunction (ASF) Ψ is then expressed as a linear combination of the CSFs

$$\Psi = \sum_k c_k \Phi_k. \tag{2.83}$$

The expansion coefficients c_k are determined through the eigenvalue problem of the CI Hamiltonian H^{CI}

$$\sum_l \left\langle \Phi_k \middle| H^{\mathrm{CI}} \middle| \Phi_l \right\rangle c_l = E c_k. \tag{2.84}$$

In the particle-hole formalism, the CI Hamiltonian takes the form [203, 206]

$$H^{\mathrm{CI}} = \sum_i \boldsymbol{\alpha} \cdot \boldsymbol{p} + (\beta - 1) + \frac{Z\alpha}{r_i} - e_i V^{\mathrm{core}} + \sum_{i<j} \frac{e_i e_j}{|\boldsymbol{r}_i - \boldsymbol{r}_j|}. \tag{2.85}$$

where, $e_i = -1$ for valence electron states and $e_i = +1$ for core holes. The term V^{core} represents the mean field generated by the core electrons, and the two-body term includes valence-valence interactions. The number of CSFs included in the CI calculations is controlled by selecting one or multiple leading configurations from which the CI space is built up by generating additional CSFs through electron excitations from these leading configurations. The number of CSFs is typically limited by specifying the number of excitations and a maximum principal quantum number n and orbital angular momentum l of the included one-electron orbitals.

Since the CI-space and thus the needed computational resources can grow quickly, it is common to include only a restricted CI space and account for additional correlations, such as core-valence correlations, by using MBPT. Including MBPT corrections modifies Eq. (2.84) as

$$\sum_l \left(\left\langle \Phi_k \middle| H^{\text{CI}} \middle| \Phi_l \right\rangle + \sum_m \frac{\left\langle \Phi_k \middle| H^{\text{CI}} \middle| \Phi_m \right\rangle \left\langle \Phi_m \middle| H^{\text{CI}} \middle| \Phi_l \right\rangle}{E - E_m} \right) c_l = E c_k, \quad (2.86)$$

where the sum over the index m only includes CSFs that lie outside the CI space. This MBPT space is similarly limited by specifying maximum values of n and l for the included orbitals.

Calculations for Ca^{+} and Ca^{14+}

We perform calculations using the AMBiT code for the ν_{570} transition in Ca^{14+} as well as for the ν_{729} and ν_{DD} transitions in Ca^{+}.

For Ca^{+}, we exclude the single valence electron from the Dirac-Fock procedure. Thus, the Dirac-Fock core consists of the 18 electrons in the $1s^2 2s^2 2p^6 3s^2 3p^6$ configuration. The CI-space was constructed by choosing the leading configurations $3p^6 4s$, $3p^6 4p$ and $3p^6 3d$ and allowing single-electron excitations of the valence electron to orbitals with maximum $n = 10$ and $l = 4$. The MBPT-space includes orbitals up to $n = 30$ and $l = 4$.

For Ca^{14+}, we include all six electrons in the $1s^2 2s^2 2p^2$ configuration in the Dirac-Fock calculations. Afterwards, the CI-space was generated from the leading configuration $1s^2 2s^2 2p^2$ with single- and double-electron excitations of the valence electrons to one-electron orbitals up to $n = 12$ and $l = 3$. In addition, single and double hole excitations from the $2s$ shell were included. The $1s$ electrons are treated as the frozen core, such that no hole excitations from the $1s$ shell are considered in the CI-space. The MBPT corrections include one-electron orbitals up to $n = 35$ and $l = 4$. The results of the X_i coefficients are shown in the left panel of Fig. 2.8 and in Tab. 2.3. To estimate the uncertainty on the calculated electronic coefficients X_i, we vary the

	ν_{570}	ν_{729}	ν_{DD}
ΔE (eV)	2.163	1.685	7.89×10^{-3}
	2.177 [202]	1.700 [202]	7.52×10^{-3} [202]
F_i (Hz/fm^2)	8.7×10^{6}	-3.77×10^{8}	5.6×10^{5}
$X_i(m_\phi = 1$ keV) (Hz)	1.96×10^{16}	-9.73×10^{16}	4.7×10^{14}

Table 2.3: Our theoretical results of the transition energy ΔE, electronic field shift coefficient F_i and electronic new physics coefficient X_i for the mediator mass $m_\phi = 1\,\text{keV}$. The calculations were performed for the ν_{729} and ν_{DD} transitions in Ca^{+} as well as for the ν_{570} transition in Ca^{14+} using the AMBiT code. The results of the transition energies deviate from reference values from Ref. [202] not more than 5%. For the King plot analysis, we assume the uncertainty on the X_i coefficients to be approximately 10%, see Tab. 2.4.

size of the basis included in the CI and MBPT calculations. In the following King plot analysis, we assume a 10% uncertainty on the X_i, see Tab. 2.4.

Sensitivity to new physics and dependence on the boson mass m_ϕ

In Fig. 2.8, we observe that the X_i coefficients decrease for higher mediator masses m_ϕ, since the range of the Yukawa potential becomes shorter and its overlap with the electronic wave functions is reduced. In contrast, for low masses the X_i coefficients become constant. In this regime, the range of the Yukawa potential becomes larger than the atomic scale, such that the overlap of the relevant electronic wavefunctions with the potential does not change significantly anymore. However, these observations alone do not fully explain the mass dependence of the resulting bounds on α_{NP}. To understand the full behavior, we recall the King relation, including the new physics contribution

$$\tilde{\boldsymbol{\nu}}_{\mathbf{2}} = K_{21} + F_{21}\tilde{\boldsymbol{\nu}}_{\mathbf{2}} + X_{21}\boldsymbol{\gamma}, \tag{2.87}$$

with $X_{21} = X_2 - \frac{F_2}{F_1}X_1$. To gain some more understanding of the electronic part of the new physics term we calculate the expression X_{21} for the combination of the old calcium King plots ν_{729}/ν_{DD} as well as for the new combination ν_{729}/ν_{570}. The results are shown in the right panel of Fig. 2.8.

First of all, we observe that X_{21} approaches zero for heavy new bosons, as the ratio X_2/X_1 approaches F_2/F_1 in the high mass regime. The reason for this behavior

$n_{\text{max}}^{\text{CI}}$	10	12	13	12	12
$l_{\text{max}}^{\text{CI}}$	3	3	3	4	3
$n_{\text{max}}^{\text{MBPT}}$	35	35	35	35	40
$l_{\text{max}}^{\text{MBPT}}$	4	4	4	4	4
ΔE_{570} (eV)	2.183	2.163	2.162	2.163	2.163
X_{570} (10^{16} Hz)	1.968	1.959	1.965	1.961	1.959

$n_{\text{max}}^{\text{CI}}$	8	10	11	10	10
$l_{\text{max}}^{\text{CI}}$	4	4	4	5	4
$n_{\text{max}}^{\text{MBPT}}$	30	30	30	30	35
$l_{\text{max}}^{\text{MBPT}}$	4	4	4	4	4
ΔE_{729} (eV)	1.691	1.685	1.688	1.685	1.685
X_{729} (10^{16} Hz)	−9.748	−9.728	−9.748	−9.728	−9.728
ΔE_{DD} (meV)	8.119	7.898	7.390	7.898	7.898
X_{DD} (10^{14} Hz)	4.367	4.703	4.362	4.703	4.703

Table 2.4: The calculated electronic new physics coefficient X_i for a boson mass of $m_\phi = 1\,\text{keV}$ and transition energy depending on the size of the CI and MBPT space. The calculations are performed for the ν_{570} transition in Ca^{14+} (upper table) as well as for the ν_{729} and ν_{DD} in Ca^{+} (lower table).

is that in the high mass limit, when the range of the Yukawa potential becomes smaller than the nuclear size, the interaction between the electrons and neutrons in the nucleus becomes effectively a contact interaction. In this limit, the new physics coefficients become approximately proportional to the field shift coefficients

$$X_i \propto F_i \propto |\Psi_b(0)|^2 - |\Psi_a(0)|^2 \,, \tag{2.88}$$

where $|\Psi_{a,b}(r)|^2$ denotes the electron density of the two states involved in the transition i [143]. Because of this alignment X_{21}, and thus also V_{th}, vanishes in the high mass limit, leading to the loss of sensitivity for high masses. Moreover, for the combination ν_{729}/ν_{DD} we observe a zero crossing in the right panel of Fig. 2.8 around $m_\phi \approx 10^4\,\text{eV}$. Such accidental cancellations lead to the peaks in the King-plot-based

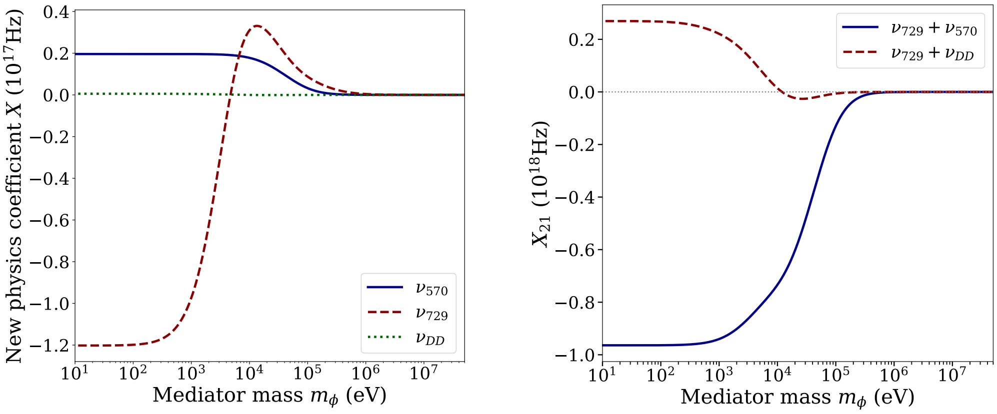

Figure 2.8: The left panel shows the electronic new physics coefficients X_i for the transitions ν_{729}, ν_{570} and ν_{DD}. The right panel shows the coefficient $X_{21} = X_2 - F_{21}X_1$ as it appears in the King relation for the two combinations ν_{729}/ν_{DD} and ν_{729}/ν_{570}. Figure adapted from Ref. [Ric4]

bounds for specific masses in the exclusion plot in Fig. 2.7. In contrast, for the combination of ν_{729} and ν_{570} no such cancellation occurs, and thus no peaks in the exclusion plot are expected for this pair of transitions.

We also note that small deviations between the theoretically predicted ratio F_i/F_j and the experimental slope $(F_i/F_j)^{\text{exp}}$ extracted from the King plot can strongly affect the bounds in the high mass regime. To correctly portray the high mass behavior, we later rescale the X_i coefficients such that X_i/X_j approaches $(F_i/F_j)^{\text{exp}}$ in the high mass limit

$$X_i' = X_i \frac{(F_i/F_j)^{\text{exp}}}{(X_i/X_j)|_{m_\phi \to \infty}} \tag{2.89}$$

With this rescaling, we obtain the correct high mass behavior

$$\frac{X_i'}{X_j} \to \left(\frac{F_i}{F_j}\right)^{\text{exp}} \quad \text{for} \quad m_\phi \to \infty. \tag{2.90}$$

Finally, we emphasize that the high mass behavior of the bounds based on the hydrogen-deuterium isotope shift differs from the King-plot-based bounds. This is because the direct comparison of the measured isotope shift frequency to its theoretical prediction is not affected by the alignment of X_i and F_i. In that case, the mass dependence is governed solely by the decrease of the X_i as a function of m_ϕ.

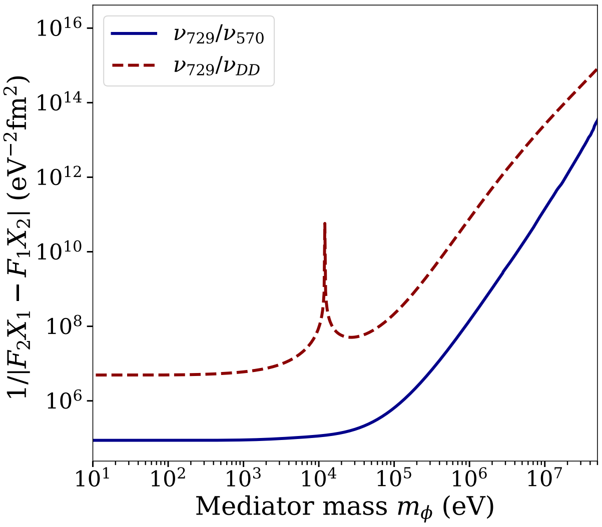

Figure 2.9: The inverse of the electronic part of V_{th} as it appears in the minimal King plot expression for α_{NP}. Results are shown for the older King plot, combining the ν_{729} and the ν_{DD} transitions in Ca$^+$ as well as for the new combination of the ν_{570} transition in Ca^{14+} with ν_{729}.

Having understood the general mass behavior, we compare the expected sensitivities of the two transition combinations to set constraints on α_{NP}. We recall from Section 2.2.2 that the bounds on α_{NP} depend on $1/V_{\text{th}}$, while the electronic part of V_{th} is given by $(F_2X_1 - F_1X_2)$. Therefore we calculate the expression $|F_jX_i - F_iX_j|^{-1}$ and show the results in Fig. 2.9 as a function of m_ϕ. We observe that the inclusion of the HCI transition ν_{570} significantly improves sensitivity, such that more stringent bounds on α_{NP} can be expected from this combination of transitions.

2.3.2 *King nonlinearities in calcium*

In this section, we turn to the analysis of the new experimental data presented in Ref. [Ric4], see Tables 2.1 and 2.2. To use the newly measured nuclear mass ratios $R_{AA'} = M'_A/M_A$ in the King plot formalism, we can rewrite the difference of inverse nuclear masses as

$$\delta_M^{AA'} = \frac{1}{M_A}\frac{1 - R_{AA'}}{R_{AA'}}, \tag{2.91}$$

where M_A is the nuclear mass of the reference isotope, which in this work will always be ^{40}Ca. The atomic mass M_{40} is given in Ref. [209]. To obtain the correct nuclear mass from this value, one has to subtract the electron masses and account for the binding energies of the electrons. However, in the expression for α_{NP}, the reference mass M_A will cancel, such that only the uncertainties on the mass ratios will affect $\sigma\,[\alpha_{\mathrm{NP}}]$. Using the formalism presented in Section 2.2, we analyze the experimental data and probe for King linearity. To quantify any nonlinearity in the data, we use the minimal King plot expression $V_{\mathrm{exp}} = \det(\tilde{\boldsymbol{\nu}}_{\mathbf{1}}, \tilde{\boldsymbol{\nu}}_{\mathbf{2}}, \mathbf{1})$ for subsets of three isotope pairs and calculate its significance with respect to the experimental uncertainty $V_{\mathrm{exp}}/\sigma\,[V_{\mathrm{exp}}]$. The results for all three combinations of isotope pairs are shown in Tab. 2.5 and we observe a large nonlinearity of approximately $10^3\sigma$.

To gain a deeper understanding of the impact of the three new measurements, we also show in Tab. 2.5 the nonlinearity significance for different combinations with older isotope shift or isotope mass data. By combining old data of the ν_{729} and ν_{732} transitions from Refs. [144, 146] with either older mass data from Ref. [209] or with the newly measured mass ratios, we obtain no significant nonlinearity $V_{\mathrm{exp}}/\sigma\,[V_{\mathrm{exp}}] < 1$. In the next step, we combine the newly measured isotope shift data of ν_{729} and ν_{570} with the former mass values and already obtain and small nonlinearity with $V_{\mathrm{exp}}/\sigma\,[V_{\mathrm{exp}}] \leq 3$. Finally, combining the new isotope shift data with the new mass ratios leads to the tremendous significance of $V_{\mathrm{exp}}/\sigma\,[V_{\mathrm{exp}}] \approx 10^3$. In the following, we will explore the origin of this nonlinearity.

Decomposition analysis

As discussed in Section 2.2.3, the decomposition plot serves as a powerful tool to analyze King nonlinearities. With measurements in four isotope pairs, we can use the two basis vectors $\boldsymbol{\Lambda}^{+}$ and $\boldsymbol{\Lambda}^{-}$, defined in Eq. (2.65).

The experimental nonlinearity is depicted by the black cross in the decomposition plot shown in Fig. 2.10. The uncertainties in λ_{+} and λ_{-} are evaluated using a Monte Carlo approach. However, the experimental uncertainty is too small to be visible in the decomposition plot.

We can compare the experimental nonlinearity to the prediction for a hypothetical new boson. The new-physics-induced nonlinearity is represented by the cyan line in Fig. 2.10, with its slope being determined by the nuclear parameter $\boldsymbol{\gamma}$. Since the experimental point does not lie on this line, the observed nonlinearity cannot be attributed solely to the effect of a new boson. Therefore, higher-order Standard Model contributions must be considered.

In Ca^{+}, the dominant Standard Model sources of nonlinearity are predicted to be the second-order mass shift and nuclear polarization, while other effects are expected

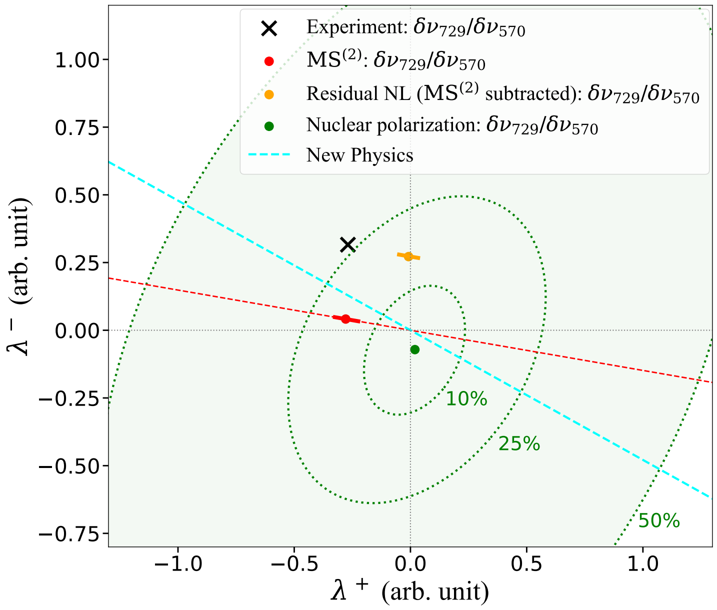

Figure 2.10: Decomposition plot of the nonlinearity in the ν_{729}/ν_{570} King plot. The observed experimental nonlinearity is depicted by the black cross, where the uncertainty is too small to be visible. The red dot shows the prediction for the second-order mass shift. The orange dot shows the residual nonlinearity after subtracting the second-order mass shift. The green dot depicts the nuclear polarization contribution. However, the nuclear polarization contribution is subject to large theoretical uncertainties, which are shown by the green shaded ellipses. Here, the different ellipses represent theoretical uncertainties of 50%, 25% and 10% on the g coefficients in Eq. (2.36). Finally, the cyan line presents the contribution of a hypothetical new boson. Figure taken from Ref. [Ric4]

to be negligible [164]. The nuclear parameter of the second-order mass shift can be expressed in terms of the nuclear mass ratios as

$$\delta_M^{AA\prime(2)} = \frac{1}{M_A^2}\frac{1-R_{AA\prime}^2}{R_{AA\prime}^2}. \tag{2.92}$$

Using this isotope dependence, we obtain the red line in the decomposition plot.

Again, the experimental uncertainty is too small to be visible, but the uncertainty in the nuclear mass ratios propagates to an uncertainty in the slope of the red line. As the experimental point does not lie on this red line either, also the second-order mass shift alone cannot explain the observed nonlinearity. To quantify its contribution to the observed nonlinearity, the electronic coefficients $K_i^{(2)}$ are required. These were calculated for Ca^{14+} in Ref. [Ric4] with an estimated uncertainty of 10% and for Ca^{+} in Ref. [164], for which the uncertainty is conservatively set to 100%. The values are given by $K^{(2)}_{729} = 0.59\,\mathrm{GHz} \times \mathrm{amu}^2$ and $K^{(2)}_{570} = 1.0\,\mathrm{GHz} \times \mathrm{amu}^2$. Using these, we calculate the nonlinearity introduced by the second-order mass shift, shown as a red dot in the decomposition plot. The associated uncertainty is again estimated with a Monte Carlo approach. Importantly, since the theoretical uncertainty in the $K^{(2)}_i$ coefficients is correlated across all isotope pairs, its impact on the overall nonlinearity is significantly suppressed. Therefore, we can subtract the second-order mass shift from the experimental data and obtain a residual nonlinearity, which is depicted by the orange dot in the decomposition plot. According to the predictions of Ref. [164], this residual nonlinearity likely stems from nuclear polarization. The corresponding isotope shifts in Ca^{+} and Ca^{14+} were calculated using the Coulomb approximation in Refs. [Ric4, 164]. and the resulting nonlinearity is shown by the green dot in Fig. 2.10. These calculations, however, do not match the residual nonlinearity. In fact, the resulting nonlinearity has an opposite sign compared to the residual experimental nonlinearity in the decomposition plot. However, nuclear polarization effects for a single state in a single isotope are already challenging to compute accurately. As a result, when evaluating differential quantities like the isotope shift between two isotopes of a transition between two states, these uncertainties can grow even more. Consequently, the predicted nonlinearity and its decomposition are also affected by large theoretical uncertainties. In this analysis, we assume a 50% uncertainty on the g coefficients in Eq. (2.36). The resulting uncertainty in the nonlinearity is again evaluated using a Monte Carlo approach. Since the theoretical uncertainty on the nuclear polarization shift stems mostly from the nuclear model, we treat this uncertainty as fully correlated between the two transitions but uncorrelated across the isotope pairs. This results in the largest green shaded ellipse shown in the decomposition plot. The true nonlinearity induced by nuclear polarization is expected to lie somewhere inside this ellipse. Since the point of the residual nonlinearity is located within this ellipse, the observed nonlinearity is compatible with the Standard Model contributions. An improvement of the theoretical uncertainty would help to decide whether nuclear polarization fully accounts for the residual nonlinearity or if other significant contributions must be taken into account. To illustrate the effect of such a reduced uncertainty, we also show the corresponding ellipses for 25% and 10% uncertainty.

2.3.3 *Constraints on new physics*

After gaining some insight into the origin of the observed nonlinearity and concluding that it is likely caused by a combination of the second-order mass shift and nuclear polarization, we finally turn to the question of wether the new isotope shift data can improve the constraints on α_{NP}.

In Section. 2.2.4, we introduced the generalized King plot method, which allows one to set constraints on new physics even in the presence of King nonlinearities. To perform such a generalized King plot analysis, at least four isotope pairs and three transitions are required. While we already have data for four isotope pairs, we need to include a third transition. Therefore, we combine the new ν_{570} and ν_{729} data with the ν_{DD} transition obtained from earlier experiments [145, 146], see Tab. 2.1.

Using the expression for the nonlinearity volume of the generalized King plot for three transitions and four isotope pairs, $V_{\mathrm{exp}}^{\mathrm{GKP}} = \det\left(\boldsymbol{\tilde{\nu}_1}, \boldsymbol{\tilde{\nu}_2}, \boldsymbol{\tilde{\nu}_3}, \mathbf{1}\right)$, we can again calculate the significance of the observed nonlinearity $V_{\mathrm{exp}}^{\mathrm{GKP}}/\sigma\left[V_{\mathrm{exp}}^{\mathrm{GKP}}\right]$. In this case, we obtain a nonlinearity of approximately 4σ. Such a remaining nonlinearity is expected, as with three transitions, it is possible to eliminate one nonlinear term. However, there are at least two significant nonlinear terms. The second-order mass shift introduces one term and the nuclear polarization introduces at least one more. Since the nuclear polarization cannot be factorized from first principles, it is not possible to clearly predict how many significant nonlinear terms are introduced through this effect. However, as we have already demonstrated in the decomposition plot, we can subtract the second-order mass shift from the experimental data. After this subtraction, the remaining nonlinearity likely stems from nuclear polarization. If this residual nonlinearity is dominated by a single factorizable term, it can be treated with the generalized King plot. For this purpose, we define the mass shift corrected isotope shifts as

$$\boldsymbol{\nu}_i^{\mathrm{MS}^{(2)}} = \boldsymbol{\nu}_i - K_i^{(2)} \boldsymbol{\delta_M^{(2)}}. \tag{2.93}$$

Replacing $\boldsymbol{\nu}_i$ with $\boldsymbol{\nu}_i^{\mathrm{MS}^{(2)}}$ in $V_{\mathrm{exp}}^{\mathrm{GKP}}$, we obtain a nonlinearity significance of only $V_{\mathrm{exp}}^{\mathrm{GKP}}/\sigma\left[V_{\mathrm{exp}}^{\mathrm{GKP}}\right] \approx 0.6$. Here, we again assume an uncertainty of 10% for the $K_i^{(2)}$ in Ca^{14+} and 100% in Ca^{+}. One might assume that the reduced significance arises solely from the increased uncertainty $\sigma\left[V_{\mathrm{exp}}^{\mathrm{GKP}}\right]$ due to the theoretical uncertainty in the $K_i^{(2)}$ coefficients. However, as in the decomposition analysis, it is crucial to consider that the uncertainty in the $K_i^{(2)}$ is correlated along all isotope pairs. This correlation strongly suppresses the impact on the overall uncertainty. As a result, $\sigma\left[V_{\mathrm{exp}}^{\mathrm{GKP}}\right]$ increases only by a factor of approximately 1.3, while the nonlinearity volume itself is reduced by a factor of approximately 6 due to the subtraction of the second-order mass shift. Even if we set the theoretical uncertainty on $K_i^{(2)}$ to zero, the resulting nonlinearity significance would be only $V_{\text{exp}}^{\text{GKP}}/\sigma\left[V_{\text{exp}}^{\text{GKP}}\right] \approx 0.9$.

Consequently, we can use the mass shift corrected isotope shifts $\boldsymbol{\nu}_i^{\text{MS}^{(2)}}$ and the resulting linear generalized King plot to constrain α_{NP}. Using Eq. (2.76), we obtain the 2σ upper bounds on $|\alpha_{\text{NP}}|$ depicted by the red line in the exclusion plot in Fig. 2.11. In most of the mass range, this line slightly improves the previous ytterbium bounds. Thus, for most of the considered mass range, this result presents the most stringent King-plot-based constraint on a coupling of a new boson to electrons and neutrons to date. The bounds from the most recent King plot analysis in ytterbium remain stronger for boson masses between 10^3 and 10^4 keV.

Transitions	Masses	Isotopes A	$V_{\mathrm{exp}}/\sigma\,[V_{\mathrm{exp}}]$
ν_{732}, ν_{729} [144, 146]	[209]	42, 44, 46	0.005
		42, 44, 48	0.3
		42, 46, 48	0.001
		44, 46, 48	0.0002
ν_{732}, ν_{729} [144, 146]	[Ric4]	42, 44, 46	0.005
		42, 44, 48	0.3
		42, 46, 48	0.001
		44, 46, 48	0.0003
ν_{570}, ν_{729} [Ric4]	[209]	42, 44, 46	2.3
		42, 44, 48	0.4
		42, 46, 48	3.0
		44, 46, 48	2.9
ν_{570}, ν_{729} [Ric4]	[Ric4]	42, 44, 46	897
		42, 44, 48	808
		42, 46, 48	5056
		44, 46, 48	5070
ν_{570}, ν_{729}, ν_{DD} [Ric4]	[Ric4]	42, 44, 46, 48	4.3
$\nu_{570}^{\mathrm{MS}^{(2)}}$, $\nu_{729}^{\mathrm{MS}^{(2)}}$, $\nu_{DD}^{\mathrm{MS}^{(2)}}$ [Ric4]	[Ric4]	42, 44, 46, 48	0.6
$\nu_{570}^{\mathrm{MS}^{(2)}}$, $\nu_{729}^{\mathrm{MS}^{(2)}}$, $\nu_{DD}^{\mathrm{MS}^{(2)}}(\sigma[K_i^{(2)}=0])$ [Ric4]	[Ric4]	42, 44, 46, 48	0.9

Table 2.5: The significance of nonlinearity $V_{\mathrm{exp}}/\sigma\,[V_{\mathrm{exp}}]$ for different data sets with reference isotope $A = 40$. Here, V_{exp} is defined as in Eqs. (2.57) and (2.76) either for two transitions and three isotope pairs or for three transitions and four isotope pairs. First, we combine older isotope shift data from Refs. [144, 146] either with the former mass values from Ref. [209] or with our newly measured nuclear mass ratios from [Ric4]. Afterwards, the different mass data are combined with the new isotope shift data of the ν_{570} and ν_{729} transitions from [Ric4]. We include the ν_{DD} transition within a GKP analysis and show the reduced nonlinearity significance in the fifth row. The last two rows show the resulting nonlinearity significance of the GKP after subtraction of the second-order mass shift from the experimental isotope shift data. In the sixth row, we assume an uncertainty on the $K_i^{(2)}$ of 10%, in Ca^{14+} and 100%, in Ca^{+}. In the last row, we set the uncertainty on the $K_i^{(2)}$ to zero. Table adapted from Ref. [Ric4]

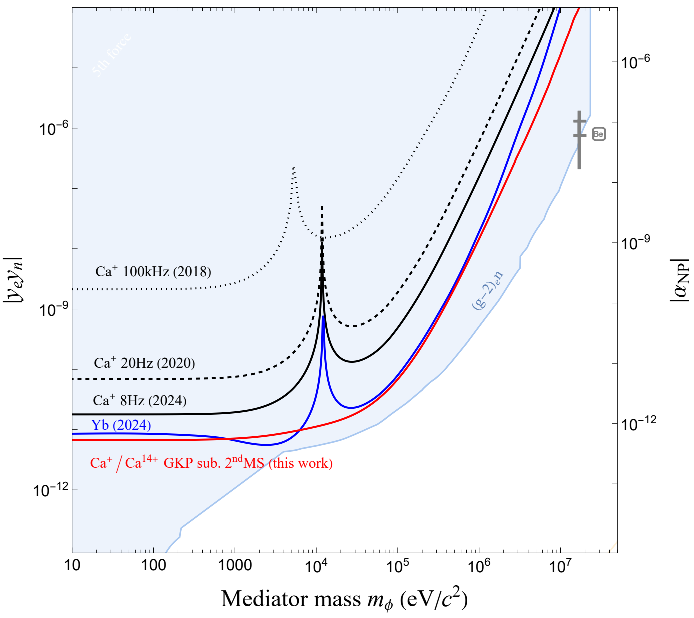

Figure 2.11: Bounds on the coupling of a hypothetical new boson to electrons and neutrons. The red line depicts the new bounds from the generalized King plot analysis including the second-order mass shift corrected isotope shift data of the ${}^2S_{1/2} \to {}^2D_{5/2}$ and ${}^2D_{3/2} \to {}^2D_{5/2}$ transitions in Ca^+ as well as of the ${}^3P_0 \to {}^3P_1$ transition in Ca^{14+}. The bounds are shown in terms of $y_e y_n$ as well as in terms of $\alpha_{\mathrm{NP}} = y_e y_n/(4\pi)$. The dotted, dashed and solid black lines show constraints resulting from previous King plot analyses in Ca^+ [143, 145, 146]. The blue line depicts the most recent constraints from King plot analyses in Yb and Yb^+ [150]. Moreover, the blue shaded region shows a combination of constraints on y_e from $(g-2)_e$ measurements [46] and constraints on y_n from neutron scattering experiments [194–196]. Finally, the black cross shows the favored region of the protophobic model to explain the beryllium anomaly [158]. Here, additional constraints, which are shown in Fig. 2.7, are omitted for better visibility. Figure adapted from Ref. [Ric4]

3

RESONANT PHOTON SCATTERING BY HIGHLY CHARGED IONS IN THE PRESENCE OF EXTERNAL FIELDS

In the previous chapter, we explored the great potential of precision spectroscopy of optical transitions in HCIs to probe nuclear effects and to constrain new physics beyond the Standard Model. In this chapter, we turn to a different energy regime and focus on the interaction of HCIs with x-ray photons. Specifically, we investigate the resonant scattering of photons by HCIs. We will discuss how this process serves as a powerful tool to study properties of HCIs and may open pathways to various different applications, including searches for physics beyond the Standard Model.

Indeed, the elastic scattering of photons on atoms or ions is one of the most fundamental aspects of light-matter interactions. Therefore, it has been the subject of various theoretical and experimental studies, and emerged as a powerful tool within atomic, molecular and nuclear physics or material science [210–217].

In general, there are three different important channels, through which the elastic scattering of x-rays by an atomic system can proceed, see Fig. 3.1. For instance, the photon can directly scatter on the nucleus, which is referred to as nuclear Thomson scattering. Moreover, the photon can scatter on the electric field of the nucleus via the excitation of virtual electron-positron pairs. This process is called Delbrück scattering and is particularly interesting as a test of QED [218–220]. Finally, the process of interest in this chapter is the scattering by the bound electrons, which is known as Rayleigh scattering. In particular, we will focus on a special case of Rayleigh scattering, in which the energy of the incoming photon is tuned to closely match the transition energy between the ground state and some excited state of the atom or ion [221–223]. This resonance condition leads to a significant enhancement of the scattering cross section and offers a variety of applications for HCI physics. For instance, it is used in EBIT experiments to study dynamics of HCIs by measuring oscillator strengths, delivering important data for the characterization of astrophysical and laboratory plasmas [224]. Another novel application of resonant photon scattering by HCIs arises through the proposal of the Gamma Factory project, which is supported by the Physics Beyond Colliders studies at CERN [11]. The key idea of this project is to store ultrarelativistic beams of HCIs in the Super Proton Synchrotron (SPS) and Large Hadron Collider (LHC) rings at CERN and collide them with counter-propagating laser photons. Due to the relativistic Doppler effect, the energy of the emitted photons is strongly enhanced, such that this process can offer a source of

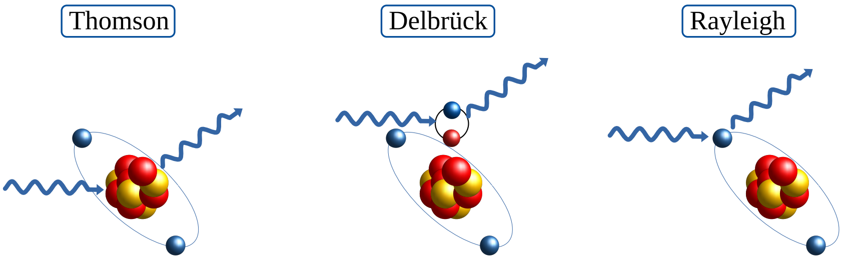

Figure 3.1: The three channels for elastic scattering between x-rays and atoms or ions. The photon can be scattered directly by the nucleus, which is called Thomson scattering. The scattering in the field of the nucleus via the excitation of virtual electron-positron pairs is known as Delbrück scattering. Here, we focus on the scattering of photons by the bound electrons, which is referred to as Rayleigh scattering.

high-intensity γ-rays. The Gamma Factory project would offer various applications for atomic, nuclear and particle physics, including different possible experiments to test the Standard Model [12–15], which we will briefly review in Section 3.5. In this thesis, we will focus in particular on the effects of external electric and magnetic fields on the process of resonant photon scattering, which will reveal applications for both, EBIT experiments and the Gamma Factory project.

We start our analysis in Section 3.1 by reviewing the basic theory of elastic photon scattering with special emphasis on the resonant approximation. Afterwards, in Section 3.2, we focus on the impact of the external fields on the electronic structure of the ions, namely the Stark and Zeeman shifts. The effects of these shifts on the scattering process will be analyzed in Section 3.3. In particular, we give an overview of the Hanle effect, which describes the modification of the polarization and angular distribution of scattered photons and will play a crucial role in this chapter [225,226]. Finally, we will turn to the two experimental scenarios. First, in Section 3.4, we consider HCIs confined in an EBIT and explore how the EBIT's magnetic field and the resulting Hanle effect enable the determination of lifetimes of excited states through resonant scattering experiments [Ric2, Ric3]. Afterwards, in Section 3.5, we turn to the spectroscopy of HCIs in storage rings within the framework of the Gamma Factory project. Specifically, we consider a setup in which a magnet is placed in the collision zone, leading to a strong magnetic and an additional electric field in the rest frame of the ion. These external fields offer additional degrees of control, enabling resonance condition tuning, beam cooling, and polarization manipulation of the emitted radiation [Ric5].

3.1 THEORY OF RESONANT ELASTIC PHOTON SCATTERING

In this section, we present the general theoretical framework for resonant elastic photon scattering, which forms the foundation of the theoretical investigations discussed in Refs. [Ric2, Ric3, Ric5].

We begin by outlining the basic geometry of the scattering process. We continue with the core of the theoretical description, the scattering amplitude for Rayleigh scattering, which is derived from the Lagrangian for bound-state QED. We then explore the resonant approximation, which becomes applicable when the photon energy closely matches the transition energy between the ground state and an excited state of the ion. In this regime, the scattering amplitude simplifies considerably, and special attention is given to the role of the natural linewidth of the intermediate excited state. Finally, we introduce the photon density matrix formalism, which provides a convenient tool for analyzing polarization properties of the scattered photons.

3.1.1 *Scattering geometry*

Before we discuss the scattering theory, it is helpful to establish the geometry of the process, which is shown in Fig. 3.2. The propagation directions of the incoming and outgoing photons with momentum vectors $\boldsymbol{k}_{i,f}$ are given by

$$\hat{\boldsymbol{k}}_{i,f} = \frac{\boldsymbol{k}_{i,f}}{|\boldsymbol{k}_{i,f}|} = \left(\sin\theta_{i,f}\cos\phi_{i,f}, \sin\theta_{i,f}\sin\phi_{i,f}, \cos\theta_{i,f}\right) . \tag{3.1}$$

Here, the two scattering angles $\theta_{i,f}$ and $\phi_{i,f}$ are defined with respect to the quantization Z-axis and the X-Z-plane, respectively. In this simple case, the natural choice is to define the Z-axis by the propagation direction of the incident radiation, such that $\theta_i = \phi_i = 0$. The ultimate goal of this chapter is the analysis of the scattering process in the presence of external electric and magnetic fields. In this case, the geometry becomes more complex and a different choice of the quantization axis, for example, along the external magnetic field vector, becomes more suitable. However, to present the basic theory of resonant photon scattering, the geometry presented in Fig. 3.2 is sufficient and we will return to more advanced geometries when we discuss external field effects. Moreover, the polarization of incoming and outgoing photons is characterized by the vectors $\boldsymbol{\epsilon}_i$ and $\boldsymbol{\epsilon}_f$. For the polarization analysis of the emitted radiation, it will prove helpful to define the scattering plane, spanned by the vectors $\hat{\boldsymbol{k}}_i$ and $\hat{\boldsymbol{k}}_f$, see Fig. 3.2.

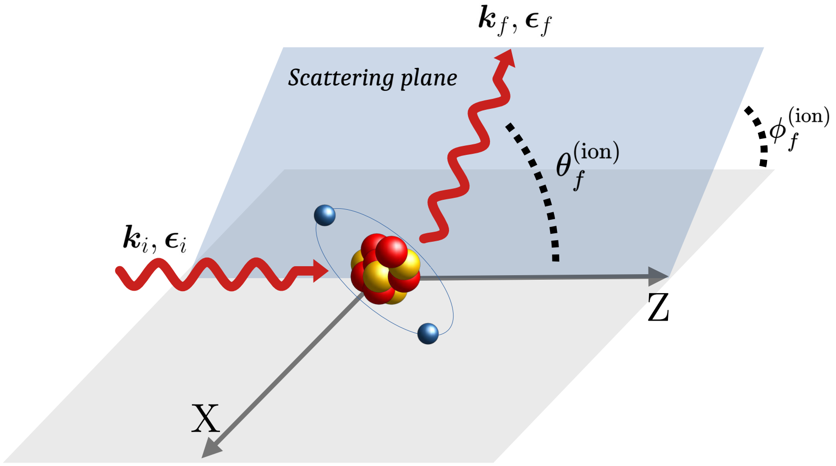

Figure 3.2: The general geometry of the resonant photon scattering process. The incoming radiation propagates along the quantization Z-axis while the direction of the emitted photons is defined by the angles θ_f and ϕ_f. The vectors $\hat{\boldsymbol{k}}_i$ and $\hat{\boldsymbol{k}}_f$ of incoming and outgoing light define the so-called scattering plane.

3.1.2 *Scattering amplitude for elastic photon scattering on bound electrons*

The process of photon scattering by electrons can be best described within the framework of QED. The QED Lagrangian is given by

$$\mathcal{L}_{\text{QED}} = -\frac{1}{4} F^{\mu\nu} F_{\mu\nu} + \bar{\psi}(i\gamma^\mu \partial_\mu - m)\psi - e\bar{\psi}\gamma^\mu A_\mu \psi, \tag{3.2}$$

where ψ is the Dirac field and A_μ is the four-potential of the electromagnetic field and $F^{\mu\nu} = \partial_\mu A_\nu - \partial_\nu A_\mu$ is the electromagnetic field tensor. The first term describes the free electromagnetic field, the second and third terms correspond to the kinetic and mass terms of the Dirac field and the last term reflects the interaction between the Dirac and the photon fields.

However, this Lagrangian describes the interaction of photons and free electrons, while we are interested in electrons bound in an atom or ion. The usual method in

(a) Absorption-first

(b) Emission-first

Figure 3.3: The process of elastic photon scattering on bound electrons is described in leading-order by two Feynman diagrams, where the double line denotes the electron in the electric field of the nucleus. The absorption-first diagram corresponds to the first term in Eq. (3.7) and the emission-first diagram represents the second term.

bound-state QED is to use the so-called Furry picture [227–229]. In this approach, the interaction with the nucleus is incorporated non-perturbatively by modifying the Dirac part of the Lagrangian, while only the interaction with the external photon field is treated as a perturbation. This leads to the modified QED Lagrangian of the form:

$$\mathcal{L}_{\text{Furry}} = -\frac{1}{4}F^{\mu\nu}F_{\mu\nu} + \bar{\psi}(i\gamma^{\mu}\partial_{\mu} - e\gamma^{0}A_{0} - m)\psi - e\bar{\psi}\gamma^{\mu}A_{\mu}\psi, \tag{3.3}$$

where the term $e\gamma^0 A_0$ reflects the static nuclear potential.

We consider the elastic photon scattering process $e^- + \gamma(\boldsymbol{k}_i, \boldsymbol{\epsilon}_i) \to e^- + \gamma(\boldsymbol{k}_f, \boldsymbol{\epsilon}_f)$, which in leading-order perturbation theory is described by the two Feynman diagrams shown in Fig. 3.3. Here, the electron states in the field of the nucleus are denoted by double lines. These diagrams can be translated to the scattering amplitude [228, 229]

$$\begin{aligned}
\mathcal{M} = {} & \\
\alpha \Bigg(& \int \mathrm{d}^4x_1 \mathrm{d}^4x_2 \bar{\varphi}_f(x_2)\gamma_{\mu_2}\epsilon_f^{\mu_2 *} e^{i\omega_i t_2 - i\boldsymbol{k}_f\cdot\boldsymbol{r}_2} S(x_2,x_1)\gamma_{\mu_1}\epsilon_i^{\mu_1} e^{-i\omega_i t_1 + i\boldsymbol{k}_i\cdot\boldsymbol{r}_1}\varphi_i(x_1) \\
& + \int \mathrm{d}^4x_1 \mathrm{d}^4x_2 \bar{\varphi}_f(x_2)\gamma_{\mu_2}\epsilon_i^{\mu_2} e^{-i\omega_i t_2 + i\boldsymbol{k}_i\cdot\boldsymbol{r}_2} S(x_2,x_1)\gamma_{\mu_1}\epsilon_f^{\mu_1 *} e^{i\omega_i t_1 - i\boldsymbol{k}_f\cdot\boldsymbol{r}_1}\varphi_i(x_1)\Bigg),
\end{aligned} \tag{3.4}$$

where the first term corresponds to the absorption-first diagram and the second term to the emission-first diagram of Fig. 3.3. Moreover, $x_{1,2} = (\boldsymbol{r}_{1,2}, t_{1,2})$ denotes space-time points and the $\varphi_n(x_{1,2}) = \varphi_n(\boldsymbol{r}_{1,2})e^{iE_n t_{1,2}}$ are solutions of the Dirac equation including the nuclear potential $V(\boldsymbol{r}) = eA_0$:

$$\left(-i\boldsymbol{\alpha}\cdot\partial_{\boldsymbol{r}} + V(\boldsymbol{r}) + \beta\right)\varphi_n(\boldsymbol{r}) = E\varphi_n(\boldsymbol{r}) \tag{3.5}$$

In this expression, we used the common notation in atomic physics with $\boldsymbol{\alpha} = \gamma^0\boldsymbol{\gamma}$ and $\beta = \gamma^0$. Moreover, the electron propagator in Eq. (3.4) is given by [228,229]

$$S(x_2, x_1) = \frac{i}{2\pi}\int \mathrm{d}\omega' e^{-i\omega'(t_2-t_1)} \sum_n \frac{\varphi_n(\boldsymbol{r}_2)\bar{\varphi}_n(\boldsymbol{r}_1)}{\omega' - E_n(1-i\delta)}, \tag{3.6}$$

with the infinitesimal shift δ. By performing the time and frequency integration and employing the Dirac notation, one obtains the well-known scattering amplitude of Rayleigh scattering [210,212,220,222,228]

$$\begin{aligned} \mathcal{M}_{M_f,M_i} = \alpha \sum_\nu & \frac{\langle f|\hat{\mathcal{R}}^\dagger(\boldsymbol{k}_f,\boldsymbol{\epsilon}_f)|\nu\rangle \, \langle\nu|\hat{\mathcal{R}}(\boldsymbol{k}_i,\boldsymbol{\epsilon}_i)|i\rangle}{E_i - E_\nu + \omega_i} \\ & + \frac{\langle f|\hat{\mathcal{R}}(\boldsymbol{k}_i,\boldsymbol{\epsilon}_i)|\nu\rangle \, \langle\nu|\hat{\mathcal{R}}^\dagger(\boldsymbol{k}_f,\boldsymbol{\epsilon}_f)|i\rangle}{E_i - E_\nu - \omega_i}. \end{aligned} \tag{3.7}$$

Here, we write $|i\rangle = |\xi_i J_i M_i\rangle$, $|\nu\rangle = |\xi_\nu J_\nu M_\nu\rangle$, and $|f\rangle = |\xi_f J_f M_f\rangle$ as the initial, intermediate, and final states, respectively, with total angular momentum J, its projection M and ξ denoting all remaining quantum numbers for a unique characterization of the states. Moreover, the operators $\hat{\mathcal{R}}$ and $\hat{\mathcal{R}}^\dagger$ were introduced as

$$\hat{\mathcal{R}} = \gamma^0\gamma_\mu\epsilon^\mu e^{i\boldsymbol{k}\cdot\boldsymbol{r}}, \tag{3.8}$$

which describe photon absorption and emission, respectively. We will describe these operators in more detail later in Section 3.1.4. But first, we explore the resonant approximation for the case of incoming photon energies that fulfill the resonance condition $\omega_i = E_\nu - E_i$.

3.1.3 *Resonant approximation*

In general, the scattering amplitude given in Eq. (3.7) involves a sum over the entire atomic spectrum, including discrete states as well as the positive and negative energy continua. In this work, however, we are specifically interested in the case of resonant photon scattering, schematically illustrated in Fig. 3.4. We assume that the energy ω_i of the incoming photon is close to the transition energy between the initial state $|i\rangle$ and an intermediate excited state $|\nu\rangle$ of the ion, such that the resonance condition $\omega_i \approx E_\nu - E_i$ is fulfilled. Under this condition, the scattering amplitude (3.7) can be significantly simplified.

In the resonant approximation, only the first term of Eq. (3.7), corresponding to the absorption-first diagram, contributes. Moreover, only a single intermediate state

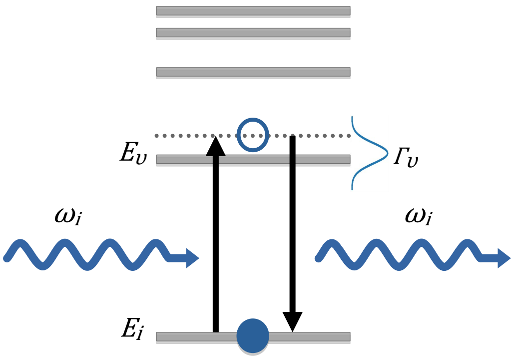

Figure 3.4: Illustration of the resonant scattering of a photon on a bound electron. Due to the absorption of the incoming photon with the energy $\omega_i \approx E_\nu - E_i$, the electron is excited to an intermediate state with the natural width Γ_ν. Afterwards, the electron decays again to the ground state and emits a photon with $\omega_f = \omega_i$. Figure taken from Ref. [Ric5]

$|\nu\rangle$, that satisfies the resonance condition, contributes, such that the sum reduces to a sum over the degenerate magnetic sublevels of the state $|\nu\rangle$. The resonant scattering amplitude in this approximation can be written as [222, 223]

$$\mathcal{M}^{\mathrm{res},(0)}_{M_f,M_i} = \alpha \sum_{M_\nu} \frac{\langle f|\hat{\mathcal{R}}^\dagger(\boldsymbol{k}_f, \boldsymbol{\epsilon}_f)|\nu\rangle \langle\nu|\hat{\mathcal{R}}(\boldsymbol{k}_i, \boldsymbol{\epsilon}_i)|i\rangle}{E_i - E_\nu + \omega_i}. \tag{3.9}$$

It is evident that Eq. (3.9) exhibits a singularity, when the photon energy exactly matches the transition energy, $\omega_i = E_\nu - E_i$. This unphysical divergence is usually resolved by accounting for the finite lifetime τ_ν of the intermediate excited state. The resulting width of this level, $\Gamma_\nu = 1/\tau_\nu$, is introduced via a complex energy shift in the denominator, $E_\nu \to E_\nu - i\Gamma_\nu/2$ and we obtain the resonant scattering amplitude [210, 222, 223, 230]

$$\mathcal{M}^{\mathrm{res}}_{M_f,M_i} = \alpha \sum_{M_\nu} \frac{\langle f|\hat{\mathcal{R}}^\dagger(\boldsymbol{k}_f, \boldsymbol{\epsilon}_f)|\nu\rangle \langle\nu|\hat{\mathcal{R}}(\boldsymbol{k}_i, \boldsymbol{\epsilon}_i)|i\rangle}{E_i - E_\nu + \omega_i + i\Gamma_\nu/2}. \tag{3.10}$$

For the evaluation of the resonant scattering process, the input parameter Γ_ν can be obtained either from experimental data of the lifetime or by calculating the transition rates of all significant decay channels for the state $|\nu\rangle$.

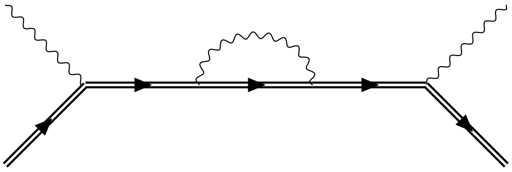

(a) First order self energy

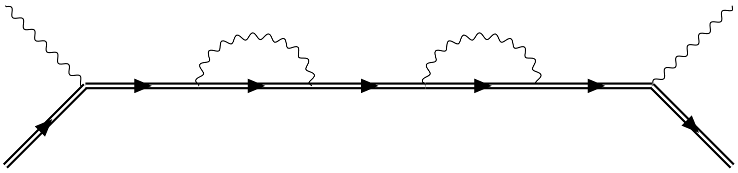

(b) Second order self energy

Figure 3.5: The first- and second-order self-energy corrections to the resonant photon scattering. The resummation of all self-energy corrections leads to the occurrence of the complex energy in the denominator of Eq. (3.10).

A more rigorous derivation of this complex energy denominator within a QED framework is presented in Refs. [228, 229]. In this approach, the lifetime effects are introduced by explicitly including self-energy corrections to the propagator of the intermediate state. The first-order self-energy insertion, which is displayed in Fig. 3.5, leads to a corrected scattering amplitude of the form

$$\mathcal{M}^{\mathrm{res},(1)}_{M_f,M_i} = \mathcal{M}^{\mathrm{res},(0)}_{M_f,M_i} \frac{\left(\hat{\Sigma}\left(\omega_i + E_i\right)\right)_{\nu\nu}}{\omega_i + E_i - E_\nu}. \tag{3.11}$$

Here, $\left(\hat{\Sigma}\left(\omega_i + E_i\right)\right)_{\nu\nu}$ denotes the matrix elements of the self-energy operator whose explicit form is given in Refs. [228,229]. Adding more self-energy insertions, as shown in Fig. 3.5 for two loops, leads to a geometric progression. After resummation, one finally obtains the scattering amplitude

$$\mathcal{M}^{\mathrm{res}}_{M_f,M_i} = \alpha \sum_{M_\nu} \frac{\langle f|\hat{\mathcal{R}}^\dagger(\boldsymbol{k}_f, \boldsymbol{\epsilon}_f)|\nu\rangle\, \langle\nu|\hat{\mathcal{R}}(\boldsymbol{k}_i, \boldsymbol{\epsilon}_i)|i\rangle}{E_i - \tilde{E}_\nu + \omega_i}, \tag{3.12}$$

with $\tilde{E}_\nu = E_\nu + \left(\hat{\Sigma}\left(\omega_i + E_i\right)\right)_{\nu\nu}$. To obtain the line shape, the self energy operator is replaced by the first term of the Taylor expansion around $E_i + \omega_i = E_\nu$, which is written as a sum of real and imaginary parts $\left(\hat{\Sigma}\left(E_\nu\right)\right)_{\nu\nu} = \Delta E^{\mathrm{SE}} + i\Gamma^{\mathrm{SE}}_\nu/2$. Here, ΔE^{SE} denotes the lowest-order electron self-energy contribution to the Lamb shift and Γ^{SE}_ν represents the lowest-order radiative width. Assuming that the real part of the self-energy correction is just absorbed into E_ν, we finally arrive again at the resonant scattering amplitude (3.10).

3.1.4 *Multipole expansion*

For further analysis of the resonant scattering amplitude (3.10), one needs to evaluate the matrix elements of the photon absorption ($\hat{\mathcal{R}}$) and emission ($\hat{\mathcal{R}}^\dagger$) operators. The absorption operator can be expressed as a sum of single-electron operators and in Coulomb gauge, it takes the form [222, 223]

$$\hat{\mathcal{R}}(\boldsymbol{k}, \boldsymbol{\epsilon}) = \sum_q \boldsymbol{\alpha}_q \cdot \boldsymbol{\epsilon} e^{i\boldsymbol{k}\boldsymbol{r}_q}, \tag{3.13}$$

where the index q represents the qth-electron. To evaluate the matrix elements of these operators, it is helpful to express the plane wave as a multipole expansion [222, 223, 231]

$$\boldsymbol{\alpha}_q \cdot \boldsymbol{\epsilon}_i e^{i\boldsymbol{k}_i\boldsymbol{r}_q} = 4\pi \sum_{pLM} i^{L-|p|} \left(\boldsymbol{\epsilon}_i \cdot \boldsymbol{Y}^{(p)*}_{LM}\left(\hat{\boldsymbol{k}}_i\right)\right) \left(\boldsymbol{\alpha}_q \cdot \boldsymbol{a}^{(p)}_{LM}\left(\omega_i; \boldsymbol{r}_q\right)\right) \tag{3.14}$$

Here, $a^{(0)}_{LM}$ and $a^{(1)}_{LM}$ represent magnetic and electric multipole components and $\boldsymbol{Y}^{(p)}_{LM}$ consists of vector spherical harmonics with the exact definition given in [231]. The matrix elements of the multipole components can be evaluated using the Wigner-Eckart theorem:

$$\begin{aligned} &\langle f|\boldsymbol{\alpha} \cdot \boldsymbol{\epsilon} e^{i\boldsymbol{k}\boldsymbol{r}}|i\rangle \\ &= \frac{4\pi}{\sqrt{2J_f+1}} \sum_{p,L,M} i^{L-|p|} \left(\boldsymbol{\epsilon} \cdot \boldsymbol{Y}^{(p)*}_{LM}(\hat{\boldsymbol{k}})\right) (J_i, m_i; L, M|J_f, m_f) \langle f||\boldsymbol{\alpha} \cdot \boldsymbol{a}^{(p)}_L||i\rangle . \end{aligned} \tag{3.15}$$

Combining this with the resonant scattering amplitude from Eq. (3.10), we obtain:

$$\begin{aligned} \mathcal{M}^{\text{res}}_{M_f,M_i} = (4\pi)^2\alpha \sum_{M_\nu} \sum_{\substack{p_1L_1M_1 \\ p_2L_2M_2}} & i^{L_1-|p_1|}(-i)^{L_2-|p_2|} \left(\boldsymbol{\epsilon}_1 \cdot \boldsymbol{Y}^{(p_1)}_{L_1M_1}(\hat{\boldsymbol{k}}_1)\right) \left(\boldsymbol{\epsilon}_2 \cdot \boldsymbol{Y}^{(p_2)*}_{L_2M_2}(\hat{\boldsymbol{k}}_2)\right)^* \\ \times & \frac{1}{\sqrt{(2J_\nu+1)(2J_f+1)}} (J_i, M_i; L_1, M_1 \mid J_\nu, M_\nu) (J_\nu, M_\nu; L_2, M_2 \mid J_f, M_f) \\ \times & \frac{\langle f|| \sum_q \boldsymbol{\alpha}_q \cdot \boldsymbol{a}^{(p_2)}_{L_2,q}||\nu\rangle \langle \nu|| \sum_q \boldsymbol{\alpha}_q \cdot \boldsymbol{a}^{(p_1)}_{L_1,q}||i\rangle}{E_\nu - E_i - \omega_1 - i\Gamma_\nu/2}. \end{aligned} \tag{3.16}$$

This form highlights a key feature of the resonant scattering amplitude, which is the factorization into angular and radial parts for each multipole channel. The radial integrals are encoded in the reduced matrix elements, while the angular dependence is determined by the Clebsch-Gordan coefficients and the vector spherical harmonics. Consequently, if there is one dominant multipole component, which is usually the case for electric dipole (E1) transitions, the angular distribution and polarization properties of the scattered photons can be fully determined by evaluating these angular functions, such that no detailed knowledge about the electronic structure is needed. In contrast, the total scattering rate always requires the calculation of the reduced matrix elements and energy levels.

3.1.5 *Cross section and polarization*

We now turn to the evaluation of physical observables of the scattering process, such as the cross section or the polarization of the scattered photons, based on the resonant scattering amplitude derived in Section 3.1.2. The differential cross section for the process, where an incident photon with polarization $\boldsymbol{\epsilon}_i$ is scattered into an outgoing photon with polarization $\boldsymbol{\epsilon}_f$, is given by the absolute square of the scattering amplitude, averaged over initial and summed over final magnetic sublevels:

$$\frac{\mathrm{d}\sigma}{\mathrm{d}\Omega}\left(\theta_f, \phi_f, \omega_i, \boldsymbol{\epsilon}_i, \boldsymbol{\epsilon}_f\right) = \frac{1}{2J_i+1} \sum_{M_i, M_f} \left| \mathcal{M}^{\mathrm{res}}_{M_f, M_i} \right|^2 . \tag{3.17}$$

Here, we assumed an initially unpolarized target ion and no detection of the angular momentum projection of the final state. While Eq. (3.17) allows to compute cross sections for fixed photon polarizations, a more general treatment of polarization properties is achieved by using the density matrix formalism [221, 223, 232].

The photon polarization can be characterized with the Stokes parameters, which are given by

$$P_1 = \frac{I_{0^\circ} - I_{90^\circ}}{I_{0^\circ} + I_{90^\circ}}, \quad P_2 = \frac{I_{45^\circ} - I_{135^\circ}}{I_{45^\circ} + I_{135^\circ}}, \quad \text{and} \quad P_3 = \frac{I_{\lambda=+1} - I_{\lambda=-1}}{I_{\lambda=+1} + I_{\lambda=-1}} . \tag{3.18}$$

Here, I_χ denotes the photon intensity of linearly polarized light, with the polarization angle χ relative to the scattering plane, see Fig. 3.2, and $I_{\lambda=\pm 1}$ corresponds to the intensity of right- and left-circularly polarized light, respectively.

The polarization state of a photon can be fully described by a 2×2 density matrix, which can be expressed by the Stokes parameters. In the helicity basis, it takes the form

$$\rho_{\lambda,\tilde{\lambda}} \equiv \langle \boldsymbol{k}\lambda|\hat{\rho}|\boldsymbol{k}\tilde{\lambda}\rangle = \mathcal{N}\begin{pmatrix} 1+P_3 & -P_1+iP_2 \\ -P_1-iP_2 & 1-P_3 \end{pmatrix}, \tag{3.19}$$

where $\lambda, \tilde{\lambda} \in \{+1, -1\}$ are the photon helicities and $\mathcal{N}$ is a normalization factor. For the incoming radiation, we set $\mathcal{N} = 1$, while for the scattered radiation, $\mathcal{N} = \mathrm{d}\sigma/\mathrm{d}\Omega$ encodes the differential cross section. If the density matrix of the outgoing photons is known, the Stokes parameters of the scattered radiation are given by

$$P_1 = -\frac{1}{2}\frac{\rho^{(f)}_{1,-1} + \rho^{(f)}_{-1,1}}{\rho^{(f)}_{1,1} + \rho^{(f)}_{-1,-1}}, \tag{3.20a}$$

$$P_2 = -\frac{i}{2}\frac{\rho^{(f)}_{1,-1} - \rho^{(f)}_{-1,1}}{\rho^{(f)}_{1,1} + \rho^{(f)}_{-1,-1}}, \tag{3.20b}$$

$$P_3 = \frac{1}{2}\frac{\rho^{(f)}_{1,1} - \rho^{(f)}_{-1,-1}}{\rho^{(f)}_{1,1} + \rho^{(f)}_{-1,-1}}. \tag{3.20c}$$

and the differential cross section can be calculated as the trace of the density matrix

$$\frac{\mathrm{d}\sigma}{\mathrm{d}\Omega}(\theta_f, \phi_f, \omega_i) = \sum_{\lambda} \rho^{(f)}_{\lambda,\lambda}. \tag{3.21}$$

Therefore, we have to relate the density matrix of the scattered photons to the one of the incoming radiation. The evolution of the density matrix is governed by the transition operator $\hat{T}$, which accounts for the resonant scattering process. The final-state density matrix is then given by

$$\hat{\rho}_f = \hat{T}\hat{\rho}_i\hat{T}^\dagger. \tag{3.22}$$

In the helicity representation, and again assuming an unpolarized target ion, the matrix elements of the final photon density matrix become

$$\begin{aligned}\langle \boldsymbol{k}_f, \lambda_f|\hat{\rho}_f|\boldsymbol{k}_f, \tilde{\lambda}_f\rangle = \frac{1}{2J_i+1}\sum_{\lambda_i,\tilde{\lambda}_i}\sum_{M_i,M_f} &\langle \boldsymbol{k}_i, \lambda_i|\hat{\rho}_i|\boldsymbol{k}_i, \tilde{\lambda}_i\rangle \\ &\times \mathcal{M}^{\text{res}}_{M_f,M_i}(\lambda_i, \lambda_f)\mathcal{M}^{\text{res}*}_{M_f,M_i}(\tilde{\lambda}_i, \tilde{\lambda}_f).\end{aligned} \tag{3.23}$$

Here, $\mathcal{M}^{\text{res}}_{M_f,M_i}(\lambda_i, \lambda_f)$ denotes the resonant scattering matrix element for the case of circularly polarized incoming and outgoing photons.

3.2 EFFECTS OF EXTERNAL FIELDS

In the previous section, we gained the tools to describe resonant photon scattering by atoms and ions. However, before we are able to explore the impact of static external electric and magnetic fields on this process, we first have to understand how such external fields affect the electronic structure of an ion. For an ion exposed to external electric and magnetic fields, we can write the Hamiltonian [233]

$$\mathcal{H} = \mathcal{H}_0 + \mathcal{H}_{\mathrm{el}} + \mathcal{H}_{\mathrm{mag}} = \mathcal{H}_0 + \sum_q \phi\left(\boldsymbol{r}_q\right) + \sum_q c\boldsymbol{\alpha}_q \boldsymbol{A}\left(\boldsymbol{r}_q\right), \tag{3.24}$$

where the scalar potential ϕ and the vector potential $\boldsymbol{A}$ describe the static external electric and magnetic fields. The effects of such fields on the electronic structure of atoms and ions have been explored in various studies [233–236]. In the present work, we will briefly revisit the basic theory of the dominant effects, namely the Stark shift and the Zeeman shift.

3.2.1 *Stark shift*

To evaluate energy shifts due to the interaction with the external electric field, it is useful to express $\mathcal{H}_{\mathrm{el}}$ as a multipole expansion. The lowest-order contribution, which affects transition energies, is the dipole contribution, leading to the well-known Stark shift. The resulting Hamiltonian can be written as [233]

$$\mathcal{H}_S = \boldsymbol{d} \cdot \boldsymbol{\mathcal{E}}, \tag{3.25}$$

where $\boldsymbol{\mathcal{E}}$ is the external electric field and $\boldsymbol{d}$ the electric dipole operator. Treating this Hamiltonian in perturbation theory, there is no energy shift in first-order. The quadratic Stark shift for a state with total angular momentum J and projection M_J along the Z-axis can be written as [235, 236]

$$\Delta E_S = -\frac{1}{2}\alpha_0 \mathcal{E}^2 - \frac{1}{4}\alpha_2 \frac{3M_J^2 - J(J+1)}{J(2J-1)}(3\mathcal{E}_z^2 - \mathcal{E}^2). \tag{3.26}$$

In this expression, α_0 and α_2 are the scalar and tensor polarizabilities. Since they do not depend on the angular momentum projection M_J, only the second term in Eq. (3.26) introduces a splitting of sublevels with different values of M_J^2.

For a state $|a\rangle$, these polarizabilities can be expressed in terms of reduced matrix elements of the electric dipole operator [235, 236]:

$$\alpha_0 = -\frac{2}{3\left(2J_a+1\right)} \sum_\nu \left(-1\right)^{\left(J_\nu - J_a\right)} \frac{\langle a||\boldsymbol{d}||\nu\rangle \langle \nu||\boldsymbol{d}||a\rangle}{E_a - E_\nu} \tag{3.27a}$$

$$\alpha_2 = (-1)^{2J_a+1} \sqrt{\frac{40J_a\,(2J_a-1)}{3\,(J_a+1)\,(2J_a+1)\,(2J_a+3)}} \times \sum_\nu \begin{Bmatrix} 1 & 1 & 2 \\ J_a & J_a & J_\nu \end{Bmatrix} \frac{\langle a||\boldsymbol{d}||\nu\rangle\,\langle\nu||\boldsymbol{d}||a\rangle}{E_a - E_\nu}. \tag{3.27b}$$

Additional to Eq. (3.25), there are higher multipole contributions like the quadrupole shift, which is, for example, investigated in Ref. [233] and depends on the electric field gradient. However, in the present work, we restrict the analysis to homogeneous electric fields, such that we only have to consider the Hamiltonian (3.25).

3.2.2 *Zeeman shift*

Similar to the Stark shift, the interaction of a bound electron, carrying a magnetic moment $\boldsymbol{\mu}$, with a homogeneous and static external magnetic field $\boldsymbol{B}$ is described by the operator [233]

$$\hat{H}_Z = (\boldsymbol{\mu} + \Delta\boldsymbol{\mu}) \cdot \boldsymbol{B}. \tag{3.28}$$

Here, $\Delta\boldsymbol{\mu}$ is a correction due to the anomalous magnetic moment of the electron. Treating this interaction in first-order perturbation theory gives rise to a shift of the atomic energy levels which is linear in the magnetic field strength $B = |\boldsymbol{B}|$:

$$\Delta E_Z^{(1)} = \mu_B g B M_J. \tag{3.29}$$

Here, μ_B is the Bohr magneton and g is the Landé g-factor [233]

$$g = \frac{\langle a||\boldsymbol{\mu} + \Delta\boldsymbol{\mu}||a\rangle}{\sqrt{J_a\,(J_a+1)\,(2J_a+1)}}. \tag{3.30}$$

This first-order Zeeman shift causes a splitting of a state with total angular momentum J into $2J+1$ substates. In second-order perturbation theory, the Hamiltonian from Eq. (3.28) leads to the additional quadratic Zeeman shift

$$\Delta E_Z^{(2)} = C_2 B^2, \tag{3.31}$$

which is proportional to B^2. The quadratic Zeeman shift coefficient C_2 for a state $|a\rangle$ can be expressed in terms of reduced matrix elements of the magnetic dipole operator

$$C_2 = \frac{1}{2J+1} \sum_\nu \frac{|(J_a M_a; 10|J_\nu M_\nu)|^2}{E_a - E_\nu} \,|\langle\nu||\boldsymbol{\mu} + \Delta\boldsymbol{\mu}||a\rangle|^2 \tag{3.32}$$

More details about the calculation of C_2 can be found in Refs. [233, 234].

3.3 SCATTERING IN EXTERNAL FIELDS AND THE HANLE EFFECT

The Stark and Zeeman shift caused by external electric and magnetic fields can have a notable impact on the properties of the resonant scattering process. One famous example of this impact, which will be important for the results of this thesis, is the well-known Hanle effect. In this effect, the Zeeman splitting of the excited state in a magnetic field leads to modifications in the polarization and angular distribution of resonantly scattered photons. Therefore, we start this section with a short excursion to the history of the Hanle effect and its classical and quantum mechanical interpretation. Afterwards, we discuss how one can incorporate such effects of external fields within the theoretical framework of resonant photon scattering.

3.3.1 *History of the Hanle effect*

The first experiments that initiated the discussion leading to the discovery of the Hanle effect were already performed at the beginning of the 20th century. In the following, we give a brief overview of the early experimental observations and its theoretical interpretation, mainly based on Ref. [237].

One of the first experiments was performed by Robert W. Wood in 1912, in which he studied the polarization properties of light scattered on mercury vapor [238]. He observed that the emitted light is linearly polarized when the scattering occurs off resonance, whereas the scattered radiation becomes unpolarized when the initial photons are in resonance with the 254 nm, $^1S_0 \to {}^3P_1$, line. Similarly, Lord Rayleigh observed slight changes in the degree of linear polarization of the scattered light in different setups without any clear explanation for this effect [237, 239]. We allow ourselves the remark that, in this context, 'Lord Rayleigh' refers to Robert John Strutt, 4th Baron Rayleigh, whereas the term 'Rayleigh scattering' is associated with his father, John William Strutt, 3rd Baron Rayleigh. Later in 1923, Robert W. Wood and Alexander Ellett revisited this issue [237,240]. They investigated the polarization of the scattered radiation for linearly polarized incoming light and explored the effect of a static external magnetic field on this scattering process. They observed that the magnetic field has a notable impact and can reduce the degree of polarization of the scattered light. Indeed, they noted that the varying polarization for slightly different setups, which was observed earlier, can be explained by different orientations with respect to the earth's magnetic field and that the degree of linear polarization can be enhanced by neutralizing the earth's magnetic field.

Wilhelm Hanle published the first correct interpretation of this effect [225]. Before we explore the quantum mechanical explanation, we briefly present the classical in-

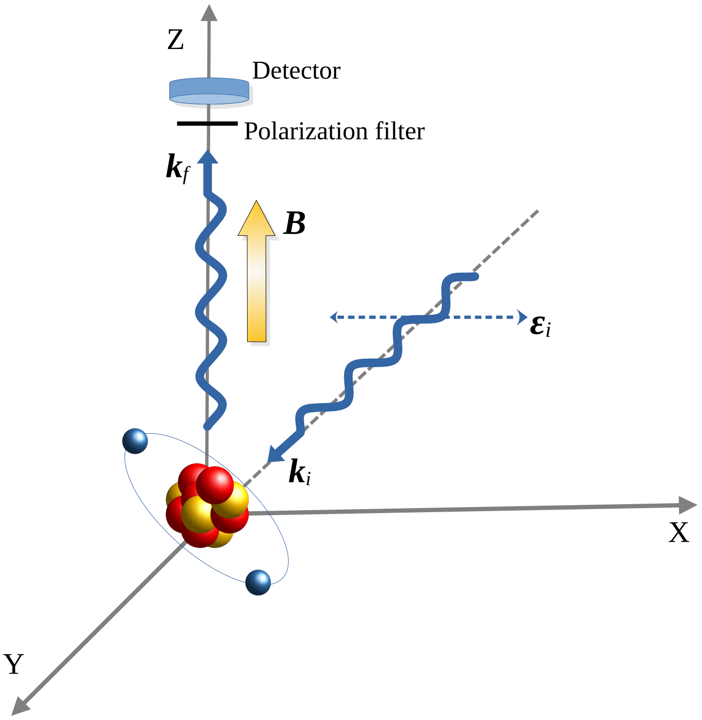

Figure 3.6: Schematic of a typical Hanle effect experiment. The incoming light is linearly polarized along the X-axis. The polarization of the scattered photons is measured for the emitted radiation in Z-direction.

terpretation. A simple schematic of a typical experimental setup to observe the Hanle effect is shown in Fig. 3.6. The incoming light, polarized along the X-axis, leads to a damped oscillation of the bound electron in X-direction. Therefore, in the absence of any external magnetic field, the emitted radiation in Z-direction is also linearly polarized in X-direction. This oscillation of the electron can be decomposed into two counter-rotating circular motions, which would each cause circularly polarized light emitted in Z-direction, such that in total linearly polarized light is observed [237]. Due to the Zeeman shift, the frequencies of the two circular motions are slightly shifted by the Larmor frequency ω_L, if an external magnetic field is introduced:

$$\omega_+ = \omega_0 + \omega_L, \tag{3.33a}$$

$$\omega_- = \omega_0 - \omega_L. \tag{3.33b}$$

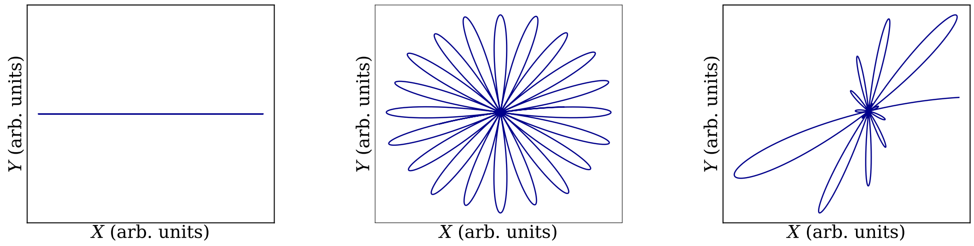

(a) Field-free case ($B = 0$) (b) $B \neq 0$ and $\tau \to \infty$ (c) $B \neq \infty$ and $\tau \sim \tau_L$

Figure 3.7: The electron in the X-Y-plane as expected from Eq. (3.34) for the classical interpretation of the Hanle effect. (a) In the field free case, the electron oscillates in X-direction. (b) For a nonzero magnetic field and a damping time τ much larger than the precession time τ_L, which is related to the Larmor frequency ω_L, the electron performs a rosette-like motion. This leads to completely unpolarized emitted radiation. (c) In the case of a nonzero magnetic field and damping time τ and precession time τ_L of similar magnitude, the electron motion leads to partial depolarization of the emitted radiation and a slight rotation of the polarization vector.

This leads to a modified electron motion in the X-Y-plane [237]

$$X(t) = A_0 e^{-\frac{t-t_0}{\tau}} \cos\left(\omega_L\left(t-t_0\right)\right) \cos\left(\omega_0\left(t-t_0\right)\right), \tag{3.34a}$$

$$Z(t) = A_0 e^{-\frac{t-t_0}{\tau}} \sin\left(\omega_L\left(t-t_0\right)\right) \cos\left(\omega_0\left(t-t_0\right)\right). \tag{3.34b}$$

This altered electron motion results in depolarization and rotation of the polarization vector of the emitted radiation and is visualized in Fig. 3.7. The magnitude of the effect depends on the damping time τ of the oscillation as well as on the external magnetic field strength which determines the Larmor frequency.

In the quantum mechanical interpretation, differences in the degree of polarization of the scattered radiation depend on whether the magnetic sublevels of the excited state contribute coherently or incoherently. First, we consider the case of two magnetic sublevels, which are degenerate in the absence of any external magnetic field. In this case, the sublevels contribute coherently, allowing the two circularly polarized components of the emitted radiation to interfere, which results in linearly polarized light. Applying an external magnetic field lifts the degeneracy, with the separation between sublevels determined by the Zeeman shift. As this splitting becomes comparable to the natural linewidth $\Gamma_\nu = 1/\tau_\nu$ of the excited state, the coherence between the sublevels is reduced. Here, the excited-state lifetime τ_ν plays the role of the damping time in the classical description. In the limit of complete separation, the sublevels no longer interfere, and the emitted light becomes unpolarized.

The dependence of this effect on the widths and, hence, on the lifetime of the excited state makes Hanle experiments a powerful tool for lifetime determinations, which was studied and used in various experiments for different systems [241–243]. We will come back to such an application for the case of lifetime determination in HCIs in Section 3.4.

As seen already in Section 3.2.1, also an electric field can lead to a splitting of sublevels. Indeed, the electric Hanle effect will play a role again in Section 3.5, in which we consider the scenario of resonant photon scattering in the Gamma Factory setup, where the ions can be exposed to strong magnetic and electric fields.

3.3.2 *Hanle effect in the framework of resonant photon scattering*

Having discussed how the Zeeman or Stark shift can influence the scattering process, we incorporate such external fields in the theoretical framework of resonant photon scattering as presented in Section 3.1.
The amplitude (3.10) is typically used to describe resonant elastic photon scattering in the absence of any external electric or magnetic fields [221–223]. However, the Stark and Zeeman shifts can easily be included by modifying the ionic energy levels in the denominator of Eq. (3.10) as [Ric5]

$$E_i = E_i^{(0)} + \Delta E_{Z,i} + \Delta E_{S,i} \tag{3.35a}$$

$$E_\nu = E_\nu^{(0)} + \Delta E_{Z,\nu} + \Delta E_{S,\nu}. \tag{3.35b}$$

Here $E_{i,f}^{(0)}$ denotes the unperturbed energies in the absence of external fields. Generally also the wave functions are affected by the external electric and magnetic fields. For example, in first-order perturbation theory, the electric field also leads to a mixture of opposite-parity states [Ric1]. Such mixing effects would allow additional transition channels in the scattering amplitude. However, we expect such effects of the external electric field on the wave functions to be quite small for the experimental scenarios that we will discuss in the next section. In these scenarios, we focus on scattering processes which proceed via E1 transitions. Consequently, the mixing of opposite-parity states would only lead to additional M1 contributions, which are usually much weaker. Therefore, we only account for the modification of the energy levels and neglect any external field effects on the ionic wave functions. Hence, the scattering amplitude can still be written in the form of Eq. (3.10) and we obtain

$$\mathcal{M}^{\mathrm{res}}_{M_f,M_i} = \alpha \sum_{M_\nu} \frac{\langle f|\hat{\mathcal{R}}^\dagger(\boldsymbol{k}_f,\boldsymbol{\epsilon}_f)|\nu\rangle\,\langle\nu|\hat{\mathcal{R}}(\boldsymbol{k}_i,\boldsymbol{\epsilon}_i)|i\rangle}{E_i^{(0)} + \Delta E_{Z,i} + \Delta E_{S,i} - E_\nu^{(0)} - \Delta E_{Z,\nu} - \Delta E_{S,\nu} + \omega_i + i\Gamma_\nu/2}. \tag{3.36}$$

A similar approach was used to study the Hanle effect in Refs. [244–246].

One consequence of this modification is that the separation of the angular and polarization part, as described in Section 3.1, becomes more complicated in the presence of external fields. Indeed, the Zeeman and Stark shifts ΔE_Z and ΔE_S generally depend on the angular momentum projections and hence have an impact on the angular distribution and polarization properties. Moreover, when the magnetic sublevels of the intermediate state are not degenerate anymore, also the initial photon energy ω_i affects the angular distribution and polarization.

To gain some confidence in this approach, we consider a typical Hanle effect experiment, as shown in Fig. 3.6. Using the scattering amplitude (3.16) and the modified energies, we can calculate the Stokes parameters of the emitted radiation for the considered geometry:

$$P_1^{(f)} = 1 - \frac{8\left(g\mu_B B\right)^2}{4\left(g\mu_B B\right)^2 + 4\Delta\omega^2 + \Gamma^2}, \tag{3.37a}$$

$$P_2^{(f)} = \frac{4g\mu_B B\Gamma}{4\left(g\mu_B B\right)^2 + 4\Delta\omega^2 + \Gamma^2}, \tag{3.37b}$$

$$P_3^{(f)} = -\frac{8g\mu_B B\Delta\omega}{4\left(g\mu_B B\right)^2 + 4\Delta\omega^2 + \Gamma^2}. \tag{3.37c}$$

Here, we introduced the detuning of the initial photon energy from the unperturbed transition energy, $\Delta\omega = E_\nu^{(0)} - E_i^{(0)} - \omega_i$. From these expressions, we can already confirm some of the observations from the early Hanle effect experiments discussed in the previous section. While the emitted radiation is completely linearly polarized ($P_1^{(f)} = 1$) for the field-free case ($B = 0$), an increasing magnetic field strength leads to a decrease of the degree of linear polarization. Moreover, $P_2^{(f)}$ becomes nonzero, corresponding to the slight rotation of the polarization vector, which was already predicted by the classical picture illustrated in Fig. 3.7. These expressions were derived for monochromatic incoming radiation, hence the Stokes parameters depend on the detuning $\Delta\omega$. Especially, the Stokes parameter $P_3^{(f)}$ is only nonzero for a nonzero detuning. However, such experiments are often times performed for the case of broad band excitation, when the width of the incoming radiation is much larger

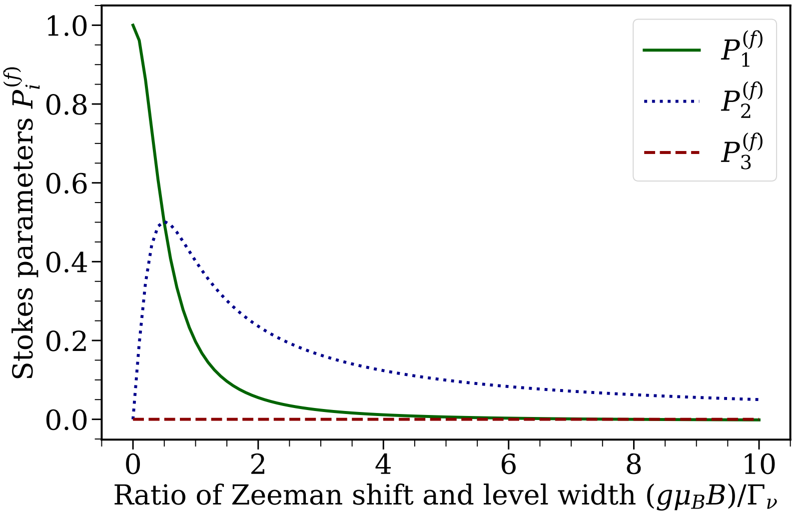

Figure 3.8: Stokes parameters of the scattered light for the experimental setup shown in Fig. 3.6. As expected, a nonzero magnetic field leads to depolarization and a rotation of the polarization vector.

than the Zeeman splitting of the excited state. Therefore, we integrate the cross section over the incoming photon frequency, or in our notation, over the detuning

$$\frac{\mathrm{d}\tilde{\sigma}}{\mathrm{d}\Omega} = \int \frac{\mathrm{d}\sigma}{\mathrm{d}\Omega}\left(\Delta\omega\right)\frac{1}{\Gamma_\omega\sqrt{2\pi}}e^{-\frac{\Delta\omega^2}{2\Gamma_\omega^2}}\,\mathrm{d}\Delta\omega. \tag{3.38}$$

Here, Γ_ω denotes the width of the frequency distribution of the incoming radiation, which is assumed to be much larger than ΔE_Z and the level width Γ_ν. The resulting Stokes parameters are shown in Fig. 3.8. This figure reproduces the expected results, showing complete linear polarization for the field-free case as well as depolarization and slight rotation for an increasing magnetic field.

3.4 RESULTS II: EBIT EXPERIMENTS FOR LIFETIME DETERMINATION

In this section, we turn to the first application of resonant photon scattering in the presence of external fields presented in this thesis. In particular, we analyze the use of the Hanle effect for lifetime determinations of excited states of HCIs confined in EBITs. The following results are based on the theoretical analysis presented in Refs. [Ric2, Ric3]. Such data of HCIs is essential for plasma diagnostics. In particular, we focus on He-like and Li-like ions, which naturally occur in astrophysical plasmas [16, 17].

We start with a short description of the considered geometry, which slightly differs from the typical Hanle experiments shown in Fig. 3.6. This experimental setup allows lifetime determinations of HCIs confined in an EBIT via resonant photon scattering using linearly polarized synchrotron radiation. Afterwards, we analyze this approach for different HCIs. First, we apply this method to the resonant photon scattering via the transition from the $1s^2\ {}^1S_0$ ground state to a $1snp\ {}^1P_1$ excited state in He-like N ions. In this case, an experiment was performed in Ref. [Ric2], which enables us to compare our theoretical predictions with experimental results. Afterwards, we turn to the case of Li-like ions and discuss the prospects of future experiments for the resonant scattering via ${}^2P_{1/2}$ or ${}^2P_{3/2}$ states [Ric3].

3.4.1 *Geometry*

We consider HCIs confined in an EBIT such that the ions are exposed to the external magnetic field of the ion trap. The experimental geometry is shown in Fig. 3.9. The external magnetic field defines the quantization Z-axis. The incoming light also propagates in Z-direction and is linearly polarized along the X-direction. The scattered photons are detected perpendicular to the incoming radiation, $\theta_f = 90°$, and either within, $\phi_f = 0°$, or perpendicular, $\phi_f = 90°$, to the polarization plane of the incident light. Here, we use the shorthand notation

$$\begin{aligned} \sigma_\perp(\omega_i) &\equiv \frac{\mathrm{d}\sigma}{\mathrm{d}\Omega}\left(\theta_f = 90°, \phi_f = 90°, \omega_i\right), \\ \sigma_\parallel(\omega_i) &\equiv \frac{\mathrm{d}\sigma}{\mathrm{d}\Omega}\left(\theta_f = 90°, \phi_f = 0, \omega_i\right). \end{aligned} \tag{3.39}$$

In the following, we will explore how the external magnetic field alters the angular distribution of the emitted photons and thus the ratio $\sigma_\parallel / \sigma_\perp$.

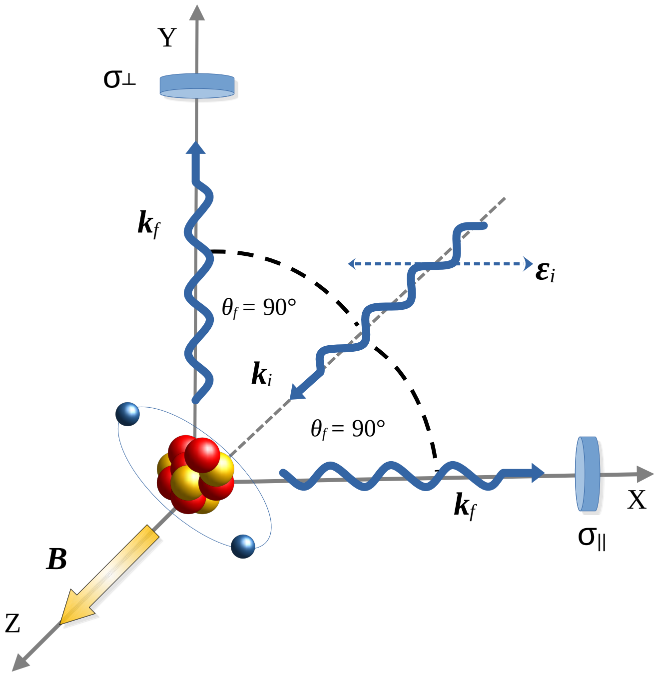

Figure 3.9: The geometry of the scattering process for the lifetime determination of HCIs confined in an EBIT. The incident radiation propagates parallel to the external magnetic field in Z-direction and is linearly polarized along the X-axis. The scattered photons are detected within and perpendicular to the polarization plane of the incident light. Figure adapted from Ref. [Ric3]

3.4.2 *Scattering via a* $J_i = 0 \to J_\nu = 1$ *transition*

In Ref. [Ric2], the setup discussed above was experimentally realized. In particular, He-like N ions were confined in the PolarX-EBIT [21] and the ratio $\sigma_{\|}/\sigma_{\perp}$ was measured using incoming soft x-rays from the Elettra synchrotron radiation facility. In this experiment, the resonant scattering proceeded via the transition from the $1s^2$ $^1S_0$ ground state to an excited $1snp$ $^1P_1$ state, where the measurement was repeated for the principal quantum numbers of the excited electron $2 \le n \le 7$. The transition energies between the ground state and the different excited $^1P_1$ states range from 431 eV for $n = 2$ up to 542 eV for $n = 7$ [Ric2]. The experimental results are depicted by the black dots in Fig. 3.10. This figure shows that $\sigma_{\|}/\sigma_{\perp}$ is close to zero for

$n = 2$, while it increases for higher excited states, such that the ratio approaches one for $n = 7$. In the following, we provide a theoretical analysis of this behavior and explore how these results are related to the lifetimes of the excited ionic states.

Using Eqs. (3.16) and (3.17), one can calculate the angular distribution for the field-free case, $B = 0$ [223]

$$\frac{\mathrm{d}\sigma}{\mathrm{d}\Omega}\left(\theta_f, \phi_f, \omega_i\right) = \sigma_0\left(\omega_i\right)\left(3 + \cos\left(2\theta_f\right) - 2\sin\left(\theta_f\right)\cos\left(2\phi_f\right)\right). \tag{3.40}$$

From this expression follows that in the absence of any external fields, no photons are scattered parallel to the initial polarization vector. In this case, we would expect the cross section ratio $\sigma_{\|}/\sigma_{\perp} = 0$ to be independent of the quantum number n.

In the next step, we account for the EBIT's magnetic field by applying the modified scattering amplitude (3.36) and calculate the cross sections for photons scattered in parallel or perpendicular directions to the polarization $\boldsymbol{\epsilon}_i$ of the incoming light. By defining the parameter $\kappa = R^2/\left[\Gamma_\nu^2 + 4\left(\Delta\omega - g\mu_B B\right)^2\right]\left[\Gamma_\nu^2 + 4\left(\Delta\omega + g\mu_B B\right)^2\right]$ we obtain the cross sections [Ric2]

$$\sigma_{\|} = 16\kappa\left(g\mu_B B\right)^2, \tag{3.41a}$$

$$\sigma_{\perp} = 4\kappa\left(\Gamma_\nu^2 + 4\Delta\omega^2\right). \tag{3.41b}$$

Here, $R = 2\pi\alpha\left|\langle 1sn\mathrm{p}^1\mathrm{P}_1||\hat{a}_{E1}||1\mathrm{s}^{21}\mathrm{S}_0\rangle\right|^2$ encodes the reduced E1 transition matrix elements. Consequently, we obtain the cross section ratio

$$\frac{\sigma_{\|}}{\sigma_{\perp}} = \frac{4\left(g\mu_B B\right)^2}{\Gamma_\nu^2 + 4\Delta\omega^2}. \tag{3.42}$$

Indeed, this expression implies that a nonzero external magnetic field leads to a nonzero cross section ratio $\sigma_{\|}/\sigma_{\perp}$, as observed in the experiment. However, the external magnetic field remains constant throughout the whole experiment and can therefore not explain the dependence of $\sigma_{\|}/\sigma_{\perp}$ on n. The origin of this behavior is hidden in the level width $\Gamma_\nu = 1/\tau_\nu$ of the intermediate state. Therefore, we calculate the lifetimes of the excited $1snp\ ^1P_1$ states using the AMBiT code, which we explained in Section 2.3.1, and present the results as the red dots in Fig. 3.11. This figure shows that the lifetime strongly increases for the higher excited $^1P_1$ states. For example, the lifetime of the $n = 7$ state is about a factor 40 larger than the lifetime for $n = 2$. This growth of the lifetime and the resulting decrease of the level width $\Gamma_\nu = 1/\tau_\nu$ leads to the observed enhancement of the cross section ratio $\sigma_{\|}/\sigma_{\perp}$.

The discussion above provides a qualitative understanding of the experimental results. However, Eqs. (3.41) and (3.42) were derived for the idealized case of monochromatic incoming light and pointlike detectors. To account for realistic experimental

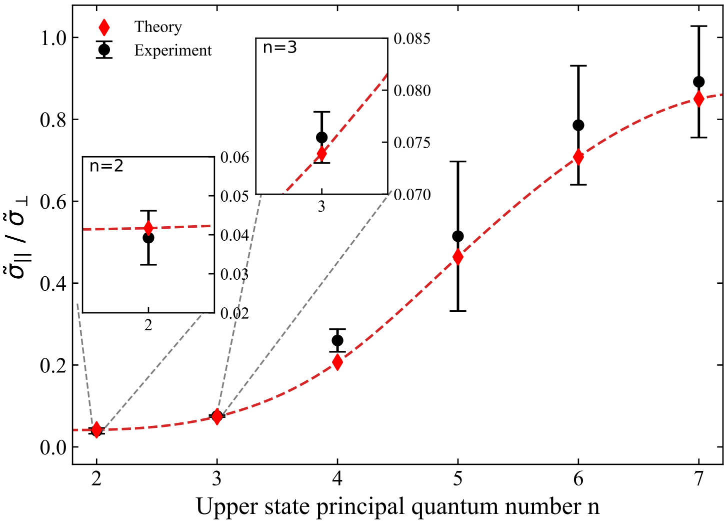

Figure 3.10: The detected and calculated cross section ratios $\tilde{\sigma}_{\perp}/\tilde{\sigma}_{\|}$ of photons scattered within or perpendicular to the polarization plane of the incoming radiation for the $1s^2\ ^1S_0 \rightarrow 1snp\ ^1P_1$ transition in He-like N ions. Figure taken from Ref. [Ric2].

conditions and to provide a quantitative analysis, we average the cross section over a Gaussian frequency distribution as in Eq. (3.38) and integrate over the solid angle of the photon detectors

$$\tilde{\sigma}_{\perp,\|} = \int \mathrm{d}\Omega^{(\mathrm{det})}_{\perp,\|} \int \mathrm{d}\Delta\omega \left[\frac{\mathrm{d}\sigma}{\mathrm{d}\Omega} (\Delta\omega) \frac{1}{\Gamma_\omega \sqrt{2\pi}} e^{-\frac{\Delta\omega^2}{2\Gamma_\omega^2}} \right] . \tag{3.43}$$

Here, the width of the incoming synchrotron radiation is set to $\Gamma_\omega = 0.1\,\mathrm{eV}$.

Using the calculated lifetimes and the external magnetic field strength of the PolarX-EBIT of $B = 0.85\,\mathrm{T}$, we obtain the predicted cross section ratio $\tilde{\sigma}_{\|}/\tilde{\sigma}_{\perp}$ shown by the red dots in Fig. 3.10. Our theoretical predictions are in good agreement with the experimental results, which verifies the assumption that the Zeeman splitting of the excited states causes the observed change in the angular distribution. In fact, this behavior is again rooted in the Hanle effect, even so the considered scheme differs from typical Hanle effect experiments. As shown in Fig. 3.8, one usually varies the external magnetic field strength, which leads to a change of the Zeeman splitting of the excited state. Consequently, the overlap of the magnetic sublevels is modified, which in turn affects the interference contribution between these sublevels. However, in the scheme considered in this thesis, the external magnetic field is constant, but the level width varies for the different excited states. For $n = 2$, the Zeeman shift

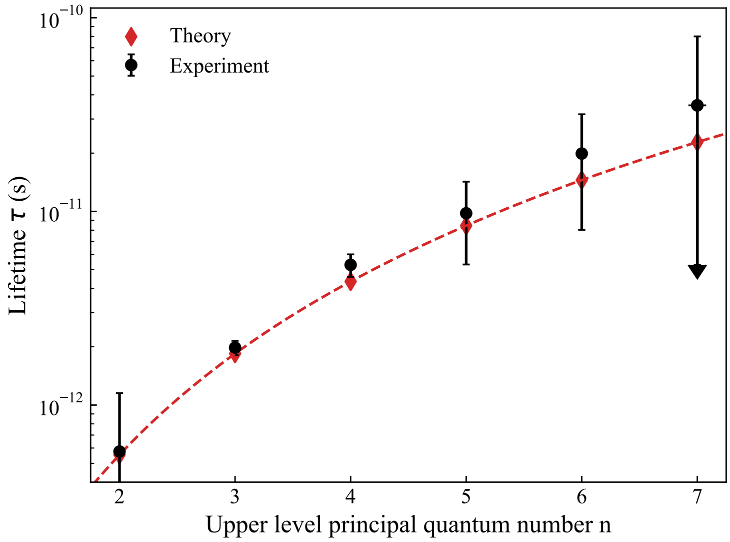

Figure 3.11: The lifetimes $\tau_\nu = 1/\Gamma_\nu$ of the excited $1snp\ ^1P_1$ states in He-like N. The theoretical predictions are calculated with the AMBiT code and are shown by the red diamonds. The results are in good agreement with the lifetimes extracted from the experimental data, which are depicted by the black dots. Figure taken from Ref. [Ric2].

is much smaller than the level width Γ_ν, such that the external magnetic field has no significant effect on the angular distribution and we obtain a cross section ratio close to zero. For the higher excited states, the level width and consequently also the overlap of the magnetic sublevels decrease. This leads to an increasing cross section ratio up to the limiting case when the magnetic sublevels are fully separated and the ratio $\tilde{\sigma}_{||}/\tilde{\sigma}_{\perp}$ approaches one.

Having identified the Hanle effect as the source of the observed behavior, one can use the experimental results of the ratio $\tilde{\sigma}_{||}/\tilde{\sigma}_{\perp}$ to determine the lifetimes of the excited states.

To extract the lifetime, the theoretical results of $\tilde{\sigma}_{||}/\tilde{\sigma}_{\perp}$ were fitted to the experimental results, where the level width Γ_ν is treated as the only free input parameter. The resulting lifetimes are shown as the black dots in Fig. 3.11 and are in good agreement with our theoretical predictions.

3.4.3 *Scattering via a* $J_i = 1/2 \rightarrow J_\nu = 1/2$ *transition*

Having demonstrated the scheme for lifetime determinations on the example of He-like ions, we want to expand this method to the case of Li-like ions [Ric3]. First, we consider the resonant scattering via the transition from the $1s^2 2s\ ^2S_{1/2}$ ground state to an excited $1s^2 np\ ^2P_{1/2}$ state.

Using the resonant scattering theory, presented in the previous sections, it follows that for $J_i = J_\nu = 1/2$ the angular distribution of scattered photons is isotropic in the absence of an external magnetic field ($B = 0$) [223]. Consequently, the cross section ratio is given by $\sigma_\parallel/\sigma_\perp = 1$. Even in the presence of an external magnetic field, this isotropy remains, such that also the ratio $\sigma_\parallel/\sigma_\perp = 1$ is unchanged. Therefore, the angular distribution of the emitted photons does not provide access to the excited-state lifetimes [Ric3].

An alternative approach, which is similar to the typical Hanle experiment shown in Fig. 3.6, enables lifetime determination also for $J_i = 1/2 \rightarrow J_\nu = 1/2 \rightarrow J_i = 1/2$ transitions through the Hanle effect [242, 243]. In this method, the incoming radiation is circularly polarized, and only circularly polarized scattered light is detected. Moreover, the measurement involves scanning the magnetic field strength to detect the zero-field crossing of the excited magnetic sublevels. While such polarization control is routine in the visible range, producing and detecting circularly polarized light in the EUV and X-ray domains remains considerably more challenging.

3.4.4 *Scattering via a* $J_i = 1/2 \rightarrow J_\nu = 3/2$ *transition*

As the considered scheme does not allow lifetime determination for $J_i = 1/2 \rightarrow J_\nu = 1/2 \rightarrow J_i = 1/2$ transitions, we now turn to the case of excited states with total angular momentum $J_\nu = 3/2$. In particular, we focus on the resonant scattering in Li-like ions via transitions from the $1s^2 2s\ ^2S_{1/2}$ ground state to an excited $1s^2 np\ ^2P_{3/2}$ state.

We again start by evaluating the angular distribution in the absence of external fields. In this field-free case, the angle-differential cross section for linearly polarized incoming light takes the form [223]:

$$\frac{\mathrm{d}\sigma}{\mathrm{d}\Omega}\left(\theta_f, \phi_f, \omega_i\right) = \sigma_0\left(\omega_i\right)\Big(17 + 3\cos\left(2\theta_f\right) - 6\sin^2\left(\theta_f\right)\cos\left(2\phi_f\right)\Big). \tag{3.44}$$

Consequently, we obtain the cross section ratio $\sigma_\parallel/\sigma_\perp = 2/5$. In contrast to the case of $J_\nu = 1/2$, we find that this angular distribution is affected by the presence of an external magnetic field, such that one obtains a modified cross section ratio $\sigma_\parallel/\sigma_\perp$. The analytical expression for $\sigma_\parallel/\sigma_\perp$ for $J_\nu = 3/2$ is much more complicated than

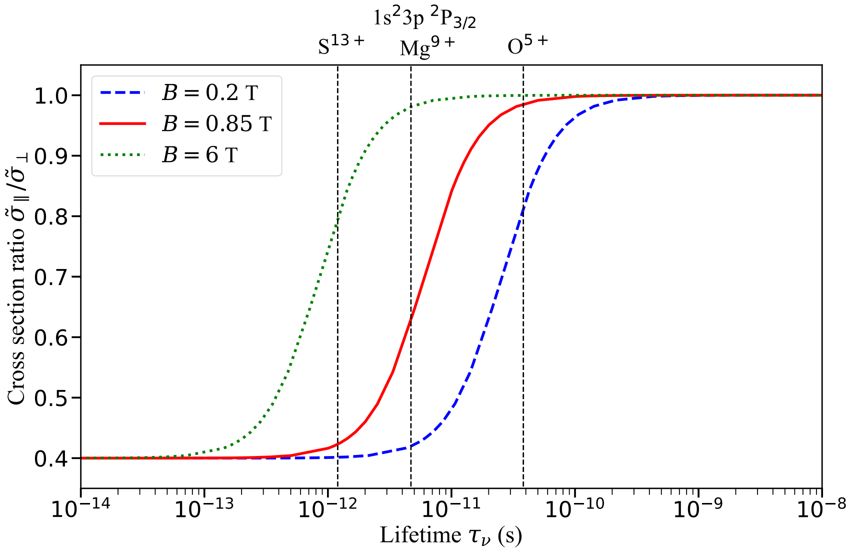

Figure 3.12: The frequency averaged cross section ratio $\tilde{\sigma}_{\|}/\tilde{\sigma}_{\perp}$ for the $1s^2 2s\ ^2S_{1/2} \to 1s^2 np\ ^2P_{3/2}$ transition in Li-like ions as a function of the lifetime $\tau_\nu = 1/\Gamma_\nu$ of the excited state. The results are shown for external magnetic field strengths of $B = 0.2$ T (blue dashed line), $B = 0.85$ T (red solid line), and $B = 6$ T (green dotted line). Moreover, the lifetimes of the $1s^2 3p\ ^2P_{3/2}$ state in Li-like O, Mg and S ions are depicted by the vertical lines. Figure taken from Ref. [Ric3].

for the previous case of the $J_i = 0 \to J_\nu = 1$ transition. The reason for this is that for the $J_i = 1/2 \to J_\nu = 3/2$ transition, more magnetic sublevels are involved in the scattering process, and a Zeeman splitting occurs not only in the excited state but also in the ground state. Therefore, we will not present the analytical expression and restrict ourselves to a numerical analysis. As above, we average the cross section over a Gaussian frequency distribution of the incident radiation and evaluate the ratio $\tilde{\sigma}_{\|}/\tilde{\sigma}_{\perp}$. For the evaluation of the Zeeman shift, the g-factors of the involved states are required. For low-Z ions, these are approximately given by $g_{^2S_{1/2}} \approx 2$ and $g_{^2P_{3/2}} \approx 4/3$.

To identify suitable systems for lifetime determination, we calculate $\tilde{\sigma}_{\|}/\tilde{\sigma}_{\perp}$ as a function of the lifetime $\tau_\nu = 1/\Gamma_\nu$ for different external magnetic field strengths. The results are shown in Fig. 3.12 together with the lifetimes of the $1s^2 3p\ ^2P_{3/2}$ states in Li-like O, Mg, and S ions, depicted by the three vertical lines. The resulting curve is similar to the one for the $J_i = 0 \to J_\nu = 1$ transition. For small lifetimes, the level width is larger than the Zeeman shift and the resulting cross section ratio approaches the value of the field-free case $\tilde{\sigma}_{\|}/\tilde{\sigma}_{\perp} = 2/5$. Larger lifetimes, and thus smaller Γ_ν, lead to an increasing cross section ratio up to the limiting case in which the sublevels are fully separated. In both of these limiting cases, the cross section ratio does not significantly change anymore with variations of the lifetime τ_ν. However, in the intermediate regime $\tilde{\sigma}_{\|}/\tilde{\sigma}_{\perp}$ is very sensitive to the lifetime of the excited state. This marks the favored region for lifetime determinations. For $B = 0.85\,\mathrm{T}$, which corresponds to the field of the PolarX-EBIT, the results are shown by the solid red line in Fig. 3.12. In this case, the regime for lifetime determinations is approximately $10^{-12}\,\mathrm{s} \leq \tau_\nu \leq 3 \times 10^{-11}\,\mathrm{s}$, which corresponds to the lifetimes of the $1s^2 3p\ ^2P_{3/2}$ state of Li-like ions with $9 \leq Z \leq 16$. A stronger magnetic field of $B = 6\,\mathrm{T}$, available with FLASH-EBIT [247], would shift the favored region to smaller lifetimes with approximately $10^{-13} \leq \tau_\nu \leq 10^{-11}\,\mathrm{s}$. Similarly, a weaker magnetic field of $B = 0.2\,\mathrm{T}$ would shift the favored region to lifetimes within the range $5 \times 10^{-12} \leq \tau_\nu \leq 10^{-10}$.

Our analysis of the $^2S_{1/2} \to {}^2P_{3/2}$ scattering process has been carried out within the electric dipole approximation in which the additional magnetic quadrupole channel was neglected. In Ref. [223], it was shown that this channel can modify the angular distribution and polarization properties of the emitted photons by up to 15% for high-Z ions. However, for low- and medium-Z ions the effect is not significant. Depending on the achievable experimental precision, this effect has to be included in future work.

Having observed the effects of an external magnetic field on the scattering process, we go one step further in the next section and account for both magnetic and electric external fields.

3.5 RESULTS III: STATIC EXTERNAL FIELDS IN THE GAMMA FACTORY SETUP

Finally, we investigate the spectroscopy of transitions in the keV regime within the framework of the Gamma Factory project. The Gamma Factory (GF) is a novel proposal and part of the Physics Beyond Colliders studies at CERN [11, 248]. Its goal is to generate high-intensity, narrow-band γ-ray beams. The key idea is to exploit resonant scattering between ultrarelativistic beams of highly charged ions and counter-propagating laser photons in the SPS and LHC rings at CERN.

Due to the relativistic Doppler effect, the photon energy in the ion rest frame is boosted according to [12]

$$\omega_{\text{ion}} \approx 2\gamma_L \omega_{\text{lab}}, \tag{3.45}$$

where $\gamma_L = 1/\sqrt{1-v^2}$ is the Lorentz factor of the ion beam. This enables laser excitation of transitions in heavy HCIs that would otherwise be inaccessible without the Doppler boost. Therefore, the GF project not only offers a source of tunable γ-rays, but also enables direct investigations of HCIs stored in the SPS or LHC rings [12]. In the second step, the energy of the scattered photons is further boosted, and their emission is strongly focused in a narrow cone along the ion beam direction due to the Lorentz transformation back to the laboratory frame. This results in photon beams with the energy [12]

$$\omega'_{\text{lab}} \approx 2\gamma_L \omega_{\text{ion}} \approx 4\gamma_L^2 \omega_{\text{lab}}. \tag{3.46}$$

This process is illustrated in Fig. 3.13. With Lorentz factors up to $\gamma_L \approx 3000$, photon energies of up to $\sim 400\,\text{MeV}$ can be reached, with intensities of around 10^{17} photons per second. This would present an improved intensity of several orders of magnitude compared to current γ-ray sources [12].

Such tunable, high-intensity and narrow-band γ-rays, as well as the direct laser excitation of heavy HCIs have tremendous potential for a wide range of experiments in atomic, nuclear and particle physics [12,13]. Examples include tests of QED through high-precision HCI spectroscopy [12], studies of Delbrück scattering [218–220, 249] and vacuum birefringence [13, 250], atomic parity violation experiments [Ric1, 106], potential measurements of ionic and nuclear electric dipole moments [12] and tests of special relativity [12, 251, 252]. The GF can also serve as a tool for new particle searches, such as axion-like particles coupling to photons. Ref. [14] explores, for instance, the prospects of using the generated γ-rays in setups similar to light-shining-through-a-wall experiments and shows that the GF might improve constraints from beam dump experiments in the mass range of approximately 1 MeV to 1 GeV. Other proposals include searches for dark photons or $B-L$ gauge bosons via dark Compton scattering [15]. In this scenario, the produced γ-ray beam is aimed at a fixed target to produce a new boson A' via the scattering $\gamma e^- \to A' e^-$. This new A' boson is then emitted under a certain angle and decays afterwards into an e^+e^- pair, which can be detected. Furthermore, circularly polarized γ-rays can be used to generate longitudinally polarized muon and positron beams, with intensities potentially exceeding those of current sources by up to four orders of magnitude [253]. The first experimental steps, which are the production and storage of highly charged ions, have been successfully demonstrated with hydrogen- and helium-like Pb and phosphorus-like Xe in the SPS and LHC rings [254, 255]. The final proof of the GF concept will be the proof of principle experiment at the SPS [256].

In this thesis, we focus on a particular scenario in which a dipole magnet is placed in the collision zone of the HCI beam and laser photons. In the ion rest frame, the Lorentz transformation leads to strong magnetic and electric fields. For velocities much smaller than those achievable at the LHC, this approach of Doppler boosting the photon frequency as well as the external electromagnetic fields is well-established in atomic physics already since the 1970s [257–260]. Within the framework of the GF project, such external fields are relevant for different applications. For instance, combined electric and magnetic fields are crucial for studies of atomic parity violation using the Stark-interference method [Ric1]. Moreover, the strong electric field would enable the measurement of polarizabilities of the HCIs [12]. In the following, we apply the theory presented in the previous sections to analyze the influence of the external electric and magnetic fields on the resonant scattering process. We examine their effects on the scattering rate as well as on the angular distribution and polarization properties of the scattered photons. Finally, we briefly discuss some technical applications of these findings for the GF setup, such as resonance condition tuning, beam cooling and polarization control. The results presented in this section are based on Ref. [Ric5].

3.5.1 *The Gamma Factory setup*

Analogous to the previous scenarios, we have to start the analysis by defining the geometry of the scattering process, which is shown in Fig 3.13, and discuss some basic parameters of the considered experimental setup. As discussed above, the key process of the Gamma Factory is the head-on collision between laser photons and relativistic HCI beams. Here, the ion beam propagation defines the Y-axis, while the photons move in the opposite direction. The emission direction of the scattered

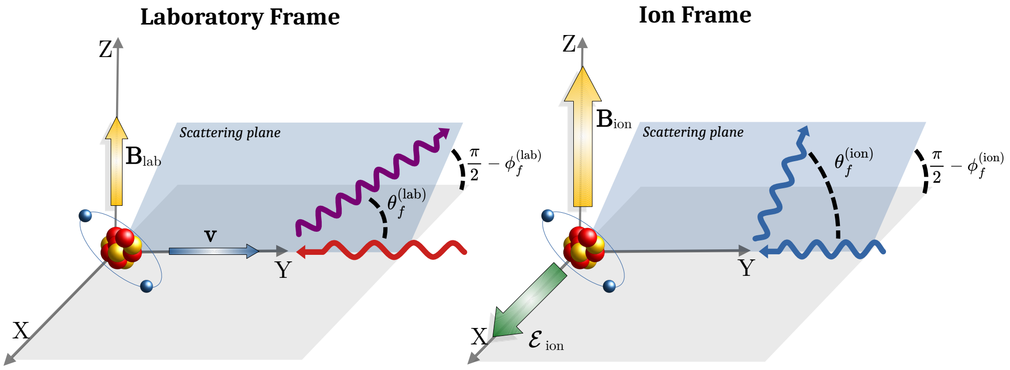

Figure 3.13: The considered geometry of the Gamma Factory setup. The ion propagates in Y-direction while the laser photons move in the opposite direction. A magnet, which is placed in the collision zone, generates a magnetic field, which defines the quantization Z-axis in the laboratory frame. Due to the Lorentz transformation, the magnetic field is enhanced in the ion rest frame and an electric field arises in X-direction. The emission direction of the scattered photons is described by the angles θ_f and ϕ_f. Figure taken from Ref. [Ric5]

photons is described by the polar angle θ_f relative to the Y-axis and the azimuthal angle ϕ_f relative to the Y-Z-plane.

In the following sections, we will perform the calculations of the scattering process in the rest frame of the ion. However, the measurements are always performed in the laboratory frame. Therefore, we have to Lorentz transform our results using the following relations [261]

$$\cos\theta_f^{(\text{ion})} = \frac{\cos\theta_f^{(\text{lab})} - v}{1 - v\cos\theta_f^{(\text{lab})}}, \tag{3.47a}$$

$$\frac{\mathrm{d}\Omega^{(\text{ion})}}{\mathrm{d}\Omega^{(\text{lab})}} = \frac{1-v^2}{\left(1 - v\cos\theta_f^{(\text{lab})}\right)^2}. \tag{3.47b}$$

The Lorentz transformation between the laboratory and ion frame not only affects the scattering angles, but also the external electromagnetic fields. We consider the scenario in which a dipole magnet is placed in the collision zone, introducing a static

	$\gamma_L = 15$	$\gamma_L = 100$	$\gamma_L = 3000$
B_{ion} in T	15	100	3000
$\mathcal{E}_{\text{ion}}$ in V m^{-1}	4×10^9	3×10^{10}	9×10^{11}

Table 3.1: The electric and magnetic field strengths in the ion frame, resulting from the Lorentz transformation (3.48) for a laboratory magnetic field strength of $B_{\text{lab}} =$ 1 T and different Lorentz factors γ_L. Table taken from Ref. [Ric5]

and homogeneous magnetic field along the quantization-Z-axis in the laboratory frame. The Lorentz transformation to the ion frame is given by

$$\boldsymbol{B}_{\text{ion}} = \gamma_L \boldsymbol{B}_{\text{lab}}, \tag{3.48a}$$

$$\boldsymbol{\mathcal{E}}_{\text{ion}} = \gamma_L \left(\boldsymbol{v} \times \boldsymbol{B}_{\text{lab}} \right). \tag{3.48b}$$

Consequently, the magnetic field strength gets enhanced by a factor γ_L, while its direction is unchanged. In addition, an electric field proportional to γ_L is introduced along the X-axis in the ion rest frame. In Tab. 3.1, we show B_{ion} and $\mathcal{E}_{\text{ion}}$ for Lorentz factors achievable at the SPS and LHC [12] and a laboratory magnetic field strengths of $B_{\text{lab}} = 1\,\text{T}$. Even though the resulting electric and magnetic fields can reach quite high values, we can treat them perturbatively for medium- and high-Z HCIs. For example, the boosted electric field is more than three orders of magnitude weaker than the Coulomb field in H-like calcium, see Fig. 1.2. Moreover, we can compare the fine-structure splitting in H-like calcium, $\Delta E_{2p_{1/2}2p_{3/2}} \approx 7\,\text{eV}$, with the resulting Zeeman shift for $B_{\text{lab}} = 1\,\text{T}$ and $\gamma_L = 3000$, which is only $\Delta E_Z \approx 0.2\,\text{eV}$ [Ric5].

In the following sections, we analyze the effects of the external electric and magnetic fields on the scattering process. For this purpose, we focus on resonant photon scattering via the transition from the $1s^2\ {}^1S_0$ ground state to the excited $1s2p\ {}^1P_1$ state in He-like calcium ions. As in Ref. [265], we consider initial laser photons with the energy $\omega_{\text{lab}} \approx 0.815\,\text{eV}$ and a Lorentz factor of $\gamma_L \approx 2395$, such that the photons in the ion rest frame fulfill the resonance condition for the transition energy $\Delta E \left({}^1S_0 \to {}^1 P_1 \right) \approx 3902\,\text{eV}$

3.5.2 *Stark and Zeeman shifts in He-like Ca*

Before we can explore the effects on the cross section, angular distribution and polarization of the scattered photons, we have to discuss the impact of the external fields on the electronic structure of the ions through the Stark and Zeeman shifts.

	$\alpha_0\left({}^1S_0\right)$ in a.u.	$\alpha_0\left({}^1P_1\right)$ in a.u.	$\alpha_2\left({}^1P_1\right)$ in a.u.	$\tau_\nu\left({}^1P_1\right)$ in s
He	1.36	-5.99×10^{1}	2.23×10^{2}	5.57×10^{-10}
	1.38 [267]	-6.00×10^{1} [268]	2.24×10^{2} [269]	5.51×10^{-10} [270]
Ca^{18+}	5.67×10^{-5}	-2.27×10^{-2}	2.38×10^{-2}	6.11×10^{-15}
				6.09×10^{-15} [271]

Table 3.2: The scalar and tensor polarizabilities (in atomic units) and the lifetimes $\tau_\nu = 1/\Gamma_\nu$ of the ${}^1S_0$ and ${}^1P_1$ states for neutral He and He-like Ca. Our results where obtained by using the AMBiT code [203] and are in good agreement with reference data from Refs. [267–271]. Table taken from Ref. [Ric5].

Using the general equations of the Zeeman and Stark shifts, as well as the Lorentz transformation of the external fields, we can write the total energy shift $\Delta E_{\mathrm{tot}} = \Delta E_Z + \Delta E_S$ of the ${}^1S_0$ and ${}^1P_1$ states as

$$\Delta E_{\mathrm{tot}}\left({}^1S_0\right) = -\frac{1}{2}\alpha_0\left({}^1S_0\right)\gamma_L^2 v^2 B_{\mathrm{lab}}^2, \tag{3.49a}$$

$$\begin{aligned}\Delta E_{\mathrm{tot}}\left({}^1P_1\right) = &\left(-\frac{1}{2}\alpha_0\left({}^1P_1\right) + \frac{3M_\nu^2-2}{4}\alpha_2\left({}^1\mathrm{P}_1\right)\right)\gamma_L^2 v^2 B_{\mathrm{lab}}^2 \\ &+ M_\nu g \mu_B \gamma_L B_{\mathrm{lab}},\end{aligned} \tag{3.49b}$$

Here, the second-order Zeeman effect is neglected, since for $B_{\mathrm{lab}} = 1\,\mathrm{T}$ and the considered Lorentz factor of $\gamma_L = 2395$, it is only about $\Delta E_Z^{(2)} \approx 10^{-5}\,\mathrm{eV}$ and thus multiple orders of magnitude smaller than the first-order Zeeman shift [Ric5], see Tab. 3.3. To evaluate ΔE_{tot}, we need the g-factor and the polarizabilities of the involved states. While the g-factor of the ${}^1S_0$ state is zero, the g-factor of the ${}^1P_1$ state is $g \approx 1$ [266]. The scalar and tensor polarizabilities are evaluated by using Eq. (3.27), where the reduced electric dipole matrix elements are obtained with the AMBiT code, see Section 2.3.1. The polarizabilities and the lifetimes of the excited ${}^1P_1$ state are listed in Tab. 3.2. The resulting Zeeman and Stark shifts of the $\left|{}^1P_1, M_\nu\right\rangle$ sublevels for $B_{\mathrm{lab}} = 1\,\mathrm{T}$ are presented in Tab. 3.3. The shifts of the ${}^1S_0$ ground state are much smaller and are not shown in this table. For the chosen parameters, the Stark shift is the dominant contribution. This shift leads to a splitting of the excited state into a $\left|{}^1P_1, M_\nu = 0\right\rangle$ and a $\left|{}^1P_1, M_\nu = \pm1\right\rangle$ sublevel. Moreover, the Zeeman shift splits the $\left|{}^1P_1, M_\nu = +1\right\rangle$ and $\left|{}^1P_1, M_\nu = -1\right\rangle$ sublevels. This structure of the magnetic sublevels is illustrated in Fig. 3.14.

M_J	ΔE_S in eV	$\Delta E_Z^{(1)}$ in eV	ΔE_{tot} in eV
0	-2.9×10^{-2}	0	-2.9×10^{-2}
1	9.2×10^{-1}	1.4×10^{-1}	10.6×10^{-1}
−1	9.2×10^{-1}	-1.4×10^{-1}	7.8×10^{-1}

Table 3.3: Calculated Zeeman and Stark shifts of the excited $\left|{}^1P_1, M_\nu\right\rangle$ sublevels in He-like Ca for a laboratory magnetic field strength of $B_{\text{lab}} = 1$ T and a Lorentz factor of $\gamma_L = 2395$. Table taken from Ref. [Ric5]

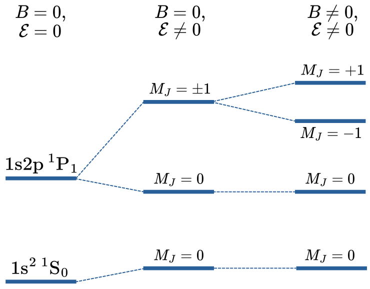

Figure 3.14: Illustration of the Zeeman and Stark shifts of the $1s^2\ {}^1S_0$ ground state and the excited $1s2p\ {}^1P_1$ state. Figure taken from Ref. [Ric5].

3.5.3 *External field effects on resonant scattering at the Gamma Factory*

Having analyzed the Stark and Zeeman shifts of the involved ionic states, we turn now to the investigation of their impact on the properties of the ${}^1S_0 \to {}^1P_1 \to {}^1S_0$ resonant scattering process. In particular, we explore the effect on the scattering rate as well as on the angular distribution and polarization properties of the emitted photons. We restrict this study to the case of circularly polarized incident radiation. This case is of particular interest for the GF project, for example, in studies of atomic parity violation [Ric1] or for the generation of circularly polarized γ-rays, which are needed for the production of longitudinally polarized lepton beams [253].

Scattering rate

We begin the discussion of the scattering process by exploring the effect of the external fields on the scattering rate. As we will see later, when we discuss the angular distribution, the emitted photons are strongly focused in the propagation direction of the ion beam, such that most photons are scattered within an opening angle of $\theta_f^{(\text{lab})} \leq 1\,\text{mrad}$. In the following, we investigate the effect of the external fields on the photon rate, observed with a detector covering the corresponding solid angle. For this purpose, we integrate the angle-differential cross section over the detector size [Ric5]

$$\sigma_{\text{det}}\left(\omega_i, B_{\text{lab}}\right) = \int_{\Omega_{\text{det}}} \frac{\mathrm{d}\sigma}{\mathrm{d}\Omega_f}\left(\theta_f, \phi_f, \omega_i, B_{\text{lab}}\right) \mathrm{d}\Omega_f, \tag{3.50}$$

For zero detuning, the integrated cross section for the field-free case can be estimated as $\sigma_{\text{det}}(\omega_i = E_\nu - E_i, B_{\text{lab}} = 0) \approx 4 \times 10^8$ barn.

Furthermore, we have to include the momentum spread of the ion beam, as it leads to a Doppler broadening of the incident laser radiation, which we treat as monochromatic in the laboratory frame. Similar to Eq. (3.38), we average the cross section over a Gaussian frequency distribution

$$\tilde{\sigma}_{\text{det}}\left(B_{\text{lab}}\right) = \int \sigma_{\text{det}}\left(\omega_i, B_{\text{lab}}\right) \frac{1}{\sqrt{2\pi\Gamma_\omega^2}} e^{-\frac{(\omega_i - \omega_{\text{ion}})^2}{2\Gamma_\omega^2}} \mathrm{d}\omega_i, \tag{3.51}$$

where the width Γ_ω reflects the momentum spread of the ion beam as $\Gamma_\omega/\omega_{\text{ion}} = \Delta p/p$. Here, the center of the frequency distribution in the ion frame is defined by the Lorentz factor of the ion beam and the laser frequency in the laboratory frame as $\omega_{\text{ion}} = 2\gamma_L\omega_{\text{lab}}$. The projected relative momentum spread for the GF setup is $\Delta p/p \approx 2 \times 10^{-4}$ [12,256]. In the following, we will refer to this case as the uncooled beam scenario. Moreover, we consider additional beam cooling, which reduces the momentum spread to $\Delta p/p \approx 1 \times 10^{-5}$ and refer to this case as the cooled beam scenario [262–264]. The corresponding results of $\tilde{\sigma}_{\text{det}}\left(B_{\text{lab}}\right)$ normalized to the result for $B_{\text{lab}} = 0$ are shown by the solid and dashed lines in the left panel of Fig. 3.15.

These results reveal that the photon rate is highly sensitive to the laboratory magnetic field. For the cooled beam, the rate drops to $\tilde{\sigma}_{\text{det}}(B_{\text{lab}})/\tilde{\sigma}_{\text{det}}(0) \approx 0.15$ as B_{lab} increases from zero to 2 T. In the uncooled case, the rate also decreases, however the decline is slower and the rate stabilizes around $\tilde{\sigma}_{\text{det}}(B_{\text{lab}})/\tilde{\sigma}_{\text{det}}(0) \approx 0.5$ for $B_{\text{lab}} > 1.5$ T.

To understand this behavior, it will prove helpful to analyze the separate contributions of the different $\left|{}^1P_1, M_\nu\right\rangle$ sublevels. By employing the multipole expansion of the photon absorption operator (3.14) and making use of some angular momentum algebra, one can obtain the photo-excitation rate from the ground state $\left|{}^1S_0, M_i = 0\right\rangle$ to one excited sublevel $\left|{}^1P_1, M_\nu\right\rangle$, which is proportional to the squared small Wigner-d matrix [Ric5, 272, 273]

$$W_{{}^1\mathrm{S}_0, M_i=0 \to {}^1\mathrm{P}_1, M_\nu} \propto \left| d^1_{M_\nu\lambda}\left(\theta_i - \frac{\pi}{2}\right)\right|^2 \left|\langle {}^1P_1 || \hat{a}_{E1} || {}^1S_0 \rangle\right|^2, \tag{3.52}$$

where $\theta_i - \pi/2 = \pi/2$ is the angle between the photon propagation direction and the quantization Z-axis. From this expression follows that the $M_\nu = \pm 1$ sublevels

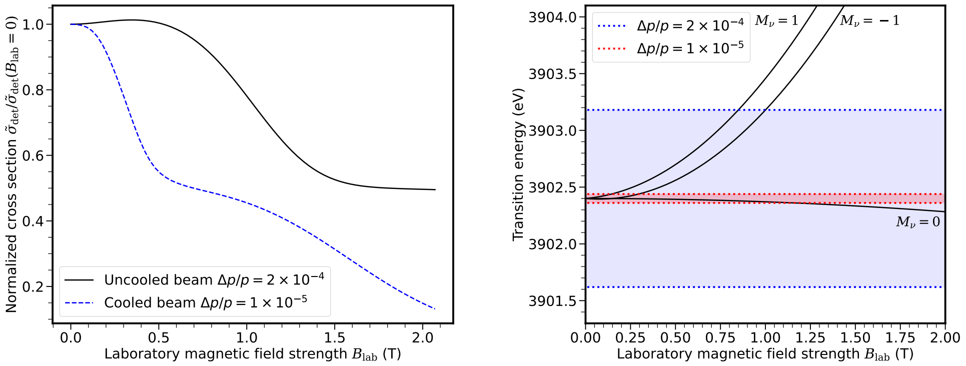

Figure 3.15: The left panel shows the cross section for the scattering via the ${}^1S_0 \to {}^1P_1$ transition in He-like Calcium of photons emitted in the propagation direction of the ion beam within an opening angle of $\theta_f^{(\rm lab)} \leq 1\,\rm mrad$ in the laboratory frame. The cross section is shown as a function of the magnetic field strength in the laboratory frame and is normalized by the result for the field-free case, $B_{\rm lab} = 0$. The calculations were performed for the uncooled beam scenario (black solid line), $\Delta p/p = 2\times10^{-4}$, and for the cooled beam scenario (blue dotted line), $\Delta p/p = 1\times10^{-5}$.
The right panel shows the transition energies between the ground state and the different excited $\left|{}^1P_1, M_\nu\right\rangle$ sublevels as a function of $B_{\rm lab}$. Moreover, the Doppler broadening of the incoming radiation is shown by the red and blue dotted lines for the scenarios of uncooled (blue) and cooled (red) ion beams. The natural line width $\Gamma_\nu = 1/\tau_\nu$ of the excited state is omitted in this illustration. Both figures taken from Ref. [Ric5]

each contribute 25% of the total excitation rate, while the $M_\nu = 0$ sublevel accounts for the remaining 50%.

By combining this knowledge with the right panel of Fig. 3.15, one can understand the dependence of the photon rate on $B_{\rm lab}$. This figure shows the transition energies from the ground state $\left|{}^1S_0\right\rangle$ to the different excited sublevels $\left|{}^1P_1, M_\nu\right\rangle$ as a function of $B_{\rm lab}$ and compares them with the Doppler broadening Γ_ω. The $M_\nu = \pm1$ sublevels get quickly shifted out of resonance in the cooled beam scenario, and for a stronger magnetic field also in the uncooled beam scenario. In this case, these sublevels do not longer contribute to the scattering process, which explains the initial decrease of the photon rate. However, while the $M_\nu = 0$ sublevel is also shifted out of resonance for higher $B_{\rm lab}$ values in the cooled beam scenario, it remains in resonance for the uncooled beam because of the larger Doppler broadening. For this reason the photon rate stabilizes at $\tilde{\sigma}_{\rm det}(B_{\rm lab})/\tilde{\sigma}_{\rm det}(0) \approx 0.5$.

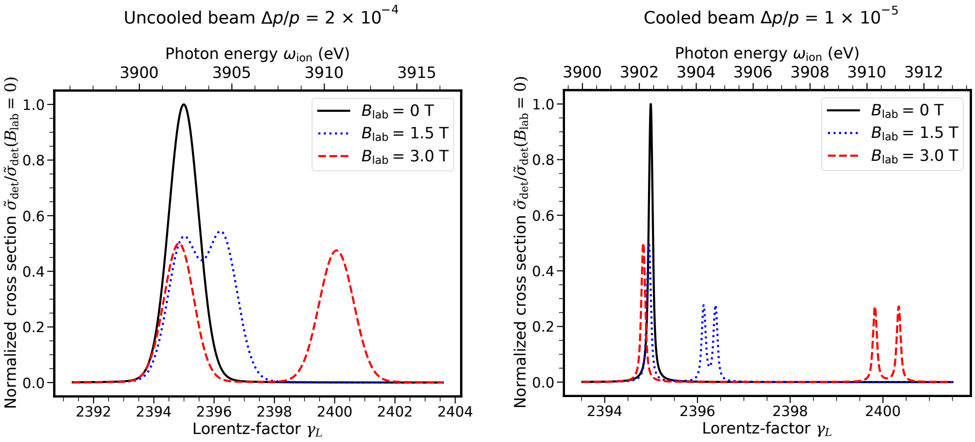

Figure 3.16: The cross section for the scattering via the $^1S_0 \rightarrow {}^1P_1$ transition in He-like Calcium of photons emitted in the propagation direction of the ion beam within an opening angle of $\theta_f^{(\mathrm{lab})} \leq 1\,\mathrm{mrad}$ in the laboratory frame. The cross section is normalized by the result for the field-free case, $B_{\mathrm{lab}} = 0$ and is shown as a function of the Lorentz factor γ_L and the resulting photon energy in the ion frame. The calculations were performed for the uncooled beam scenario (left panel), $\Delta p/p = 2 \times 10^{-4}$, and for the cooled beam scenario (right panel), $\Delta p/p = 1 \times 10^{-5}$. Figure taken from Ref. [Ric5].

Finally, we also analyze the GF scenario, in which the photon energy in the ion frame can be tuned by varying the Lorentz factor of the ion beam. In our formalism, this is realized by adjusting $\omega_{\mathrm{ion}} = 2\gamma_L\omega_{\mathrm{lab}}$ in Eq. (3.51). In Fig. 3.16 we show the normalized cross section $\tilde{\sigma}_{\mathrm{det}}$ as a function of γ_L for the uncooled and cooled beam scenarios. As seen from this figure, in both cases the Stark splitting for $B_{\mathrm{lab}} = 3\,\mathrm{T}$ between the $\left|{}^1P_1, M_\nu = 0\right\rangle$ and $\left|{}^1P_1, M_\nu = \pm1\right\rangle$ sublevels is resolved, which offers multiple applications for the GF, as we will further discuss in Section 3.5.4. The additional Zeeman splitting of the $\left|{}^1P_1, M_\nu = \pm1\right\rangle$ sublevels, however, only becomes visible for the cooled beam. The height of the peaks again reflects the relative contribution of the different excited sublevels to the scattering process.

Angular Distribution

As we have already discussed in Section 3.4, an external magnetic field has an impact on the angular distribution of the emitted photons. In the following, we explore this effect for the considered GF setup.

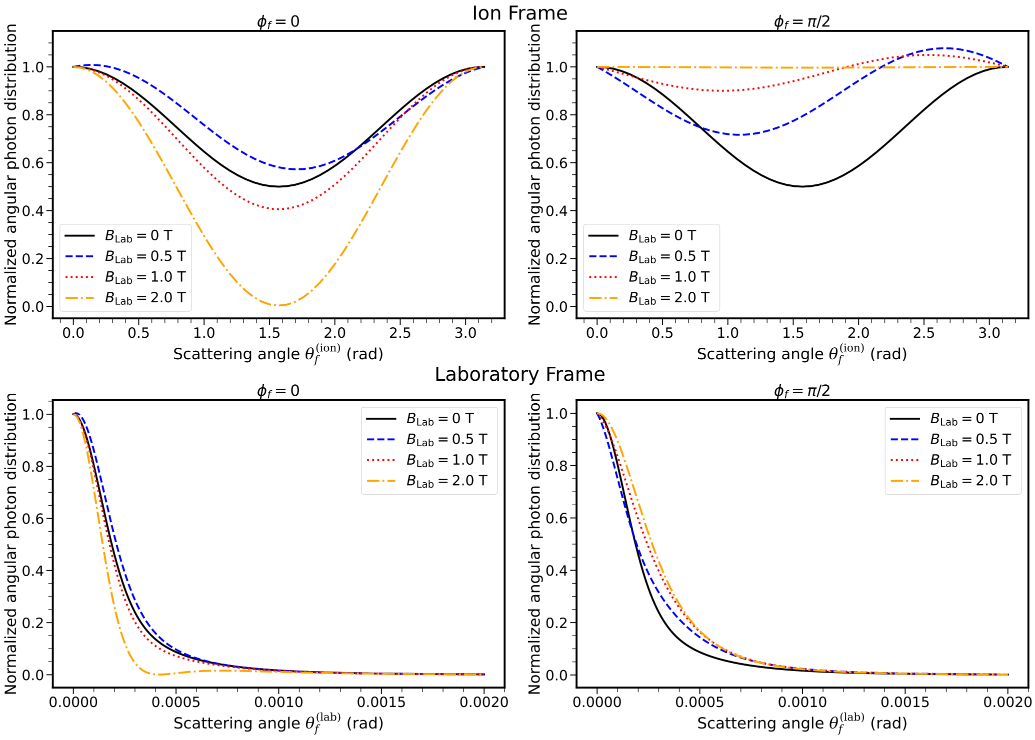

Figure 3.17: The emission patterns of the scattered photons in the ion frame and the laboratory frame for different values of B_{lab}. Each angular distribution is normalized by its value for $\theta_f = 0$. Calculations were performed for the scattering via the $1s^2\ {}^1S_0 \to 1s2p\ {}^1P_1$ transition in a He-like Ca ion and for a Lorentz factor of the ion beam of $\gamma_L = 2395$. Figure taken from Ref. [Ric5].

We start again with the angular distribution in the field-free case, $B_{\mathrm{lab}} = 0$. For the considered case of circularly polarized incident radiation, the angle-differential cross section in the ion rest frame is given by [223]

$$\frac{\mathrm{d}\sigma}{\mathrm{d}\Omega}\left(\theta_f^{(\mathrm{ion})}, \phi_f^{(\mathrm{ion})}, \omega_i\right) = \sigma_0\left(\omega_i\right)\left(3 + \cos 2\theta_f^{(\mathrm{ion})}\right). \tag{3.53}$$

As before, we account for the momentum spread of the ion beam and the resulting Doppler broadening by averaging over the Gaussian frequency distribution. However, since for the field-free case (3.53) all magnetic sublevels are degenerate and the energy dependence only appears in the prefactor σ_0, the emission pattern is not affected by this Doppler broadening. As shown by the solid black line in the upper panels of Fig. 3.17, the angular distribution in the ion frame for $B_{\mathrm{lab}} = 0$ is symmetric with respect to $\theta_f^{(\mathrm{ion})} = \pi/2$ and does not depend on the azimuthal angle $\phi_f^{(\mathrm{ion})}$. Moreover, we show in this figure calculations for nonzero magnetic field strengths in the uncooled beam scenario. These results reveal a strong sensitivity of the emission pattern on the laboratory magnetic field strength already for $B_{\mathrm{lab}} \approx 0.5\,\mathrm{T}$. In particular, we observe that the azimuthal symmetry as well as the symmetry with respect to $\theta_f^{(\mathrm{ion})} = \pi/2$ are broken due to the external magnetic and electric field in the ion frame.

One of the reasons for this variation of the angular distribution with the laboratory magnetic field is the Hanle effect, discussed earlier. However, the behavior is not uniform, as weak and strong fields lead to qualitatively different outcomes. For instance, Fig. 3.17 shows that the emission pattern for $\phi_f = 0$ becomes more isotropic for $B_{\mathrm{lab}} = 0.5\,\mathrm{T}$, while for $B_{\mathrm{lab}} \geq 1\,\mathrm{T}$ we observe the opposite effect. For small B_{lab}, the Zeeman and Stark shifts are still much smaller than the Doppler broadening but comparable to the natural width Γ_ν, such that the angular distribution is altered due to the Hanle effect. At higher fields, a different effect plays a role. As shown in the right panel of Fig. 3.15, for $B_{\mathrm{lab}} > 1\,\mathrm{T}$ the $\left|{}^1P_1, M_\nu = \pm 1\right\rangle$ sublevels are shifted out of resonance. In this case, the angular distribution is determined mainly by the contribution of the $\left|{}^1P_1, M_\nu = 0\right\rangle$ sublevel.

Finally, to relate our calculations to measurements, which are performed in the laboratory frame, we have to Lorentz transform the results by using Eq. (3.47). The emission patterns of scattered photons in the laboratory frame are shown in the lower panels of Fig. 3.17. First of all, this figure reveals the expected focusing of the scattered photons in the direction of the ion beam propagation. As stated earlier, most of the photons are emitted within an opening angle of $\theta_f^{(\mathrm{lab})} \leq 1\,\mathrm{mrad}$.

Interestingly, the influence of the laboratory magnetic field persists despite the strong focusing and shows opposite trends for $\phi_f^{(\mathrm{lab})} = 0$ and $\phi_f^{(\mathrm{lab})} = \pi/2$. For $\phi_f^{(\mathrm{lab})} = 0$, a field of $B_{\mathrm{lab}} = 2\,\mathrm{T}$ enhances the forward focusing of the photons along the ion beam compared to the field-free case. In contrast, at $\phi_f^{(\mathrm{lab})} = \pi/2$, the magnetic field leads to a slight broadening of the angular distribution. The effect is particularly pronounced in the interval $0.3\,\mathrm{mrad} \leq \theta_f^{(\mathrm{lab})} \leq 0.6\,\mathrm{mrad}$, where the deviation from the field-free scenario becomes significant.

Polarization

As already discovered in the early Hanle effect experiments, an external magnetic or electric field can have a notable impact on the polarization of scattered photons. To analyze this effect in the GF framework, we again start with the field-free case. For

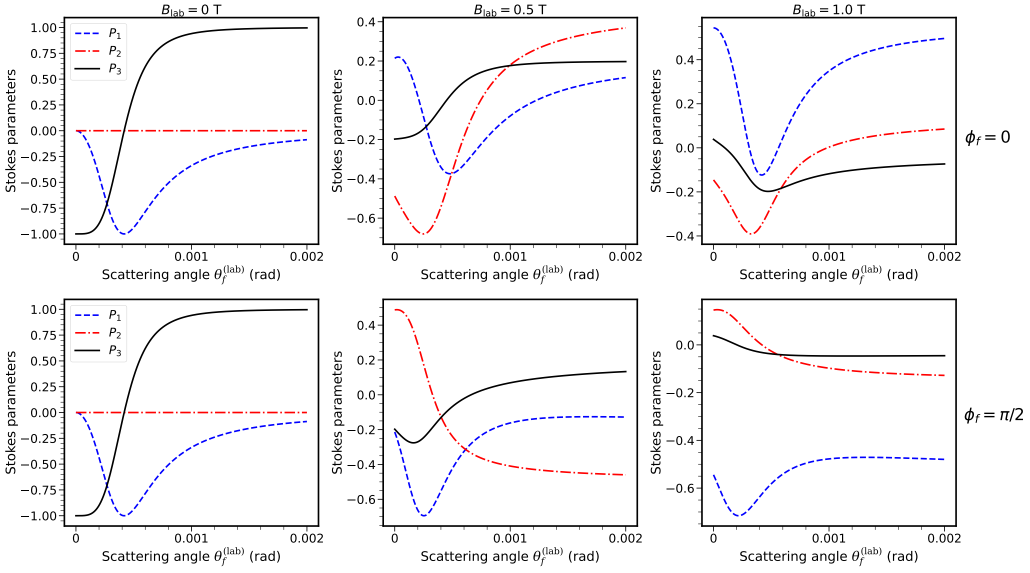

Figure 3.18: The polarization of the emitted photons characterized by the three Stokes parameters $P_i^{(f)}$ in the laboratory frame for different laboratory magnetic field strengths. Calculations were performed for the scattering via the $1s^2\ {}^1S_0 \to 1s2p\ {}^1P_1$ transition in a He-like Ca ion and for circularly polarized incoming light and a Lorentz factor of the ion beam of $\gamma_L = 2395$. Figure taken from Ref. [Ric5]

$B_{\mathrm{lab}} = 0$ and circularly polarized incident radiation, the Stokes parameters of the emitted photons in the ion frame can be written as [223]:

$$P_1^{(f),(\mathrm{ion})}\left(\theta_f^{(\mathrm{ion})}, \phi_f^{(\mathrm{ion})}\right) = \frac{-2\sin^2\theta_f^{(\mathrm{ion})}}{3 + \cos 2\theta_f^{(\mathrm{ion})}}, \tag{3.54a}$$

$$P_2^{(f),(\mathrm{ion})}\left(\theta_f^{(\mathrm{ion})}, \phi_f^{(\mathrm{ion})}\right) = 0, \tag{3.54b}$$

$$P_3^{(f),(\mathrm{ion})}\left(\theta_f^{(\mathrm{ion})}, \phi_f^{(\mathrm{ion})}\right) = \frac{-4\cos\theta_f^{(\mathrm{ion})}}{3 + \cos 2\theta_f^{(\mathrm{ion})}}. \tag{3.54c}$$

In this case, the Lorentz transformation to the laboratory frame is given by the simple relation

$$P_{1,2,3}^{(f),(\mathrm{ion})}\left(\theta_f^{(\mathrm{ion})}, \phi_f^{(\mathrm{ion})}\right) = P_{1,2,3}^{(f),(\mathrm{lab})}\left(\theta_f^{(\mathrm{lab})}, \phi_f^{(\mathrm{lab})}\right), \tag{3.55}$$

We again average the cross section over the frequency distribution for the uncooled beam and calculate the resulting Stokes parameters in the laboratory frame as a function of the scattering angle and for different B_{lab} values. The results, shown in Fig. 3.18, reveal a strong sensitivity of the Stokes parameters on the laboratory magnetic field strength. For instance, the degree of circular polarization, characterized by $P_3^{(f)}$, is reduced by the external electric and magnetic fields. In contrast, the Stokes parameter $P_2^{(f)}$, which is zero for all scattering angles in the field-free case, becomes nonzero in the presence of external fields.

To highlight the effect of an increasing laboratory magnetic field strength, we show in Fig. 3.19 the Stokes parameters $P_i^{(f)}$ for photons scattered in the direction of the ion beam propagation, $\theta_f^{(\text{ion})} = \theta_f^{(\text{lab})} = 0$, as a function of B_{lab}. In the field-free case, the emitted photons exhibit full circular polarization for the considered scenario of circularly polarized incident radiation. This conversion of circularly polarized laser photons to circularly polarized γ-rays is particularly interesting for the GF project, as such polarized γ-rays can serve as a source of longitudinally polarized lepton beams [253]. However, an increasing laboratory magnetic field strength reduces the degree of circular polarization, while in turn the degree of linear polarization is enhanced. In the cooled beam scenario, already for $B_{\text{lab}} \geq 0.5\,\text{T}$, the outgoing photons are almost fully linearly polarized.

In the next section, we will discuss some applications of the observed sensitivity of the scattering process to the laboratory magnetic field for the GF project.

3.5.4 *Applications for the Gamma Factory*

In the previous sections, we investigated the impact of external electric and magnetic fields on the scattering rate, the angular distribution and the polarization of emitted photons. In particular, we considered a scenario in which a magnet is placed in the collision zone of laser photons and the ion beam within the GF setup. This magnet would lead to strong electric and magnetic fields in the rest frame of the ions due to the Lorentz transformation. The inclusion of such fields into the GF setup would be important, for example, for atomic parity violation studies or for the determination of polarizabilities of HCIs [Ric1,12]. In the following, we briefly discuss some possible additional applications of the sensitivity of the scattering process to the laboratory magnetic field, which was observed in the present work.

Resonance condition tuning

One application of the laboratory magnetic field is a possible simplification of the search for the resonance peak. The current uncertainty of γ_L for beams at the SPS is about 0.02 % and grows up to 0.1 % for the highest beam energies at the LHC [Ric5]. The usual procedure to find the γ_L value, which fulfills the resonance condition,

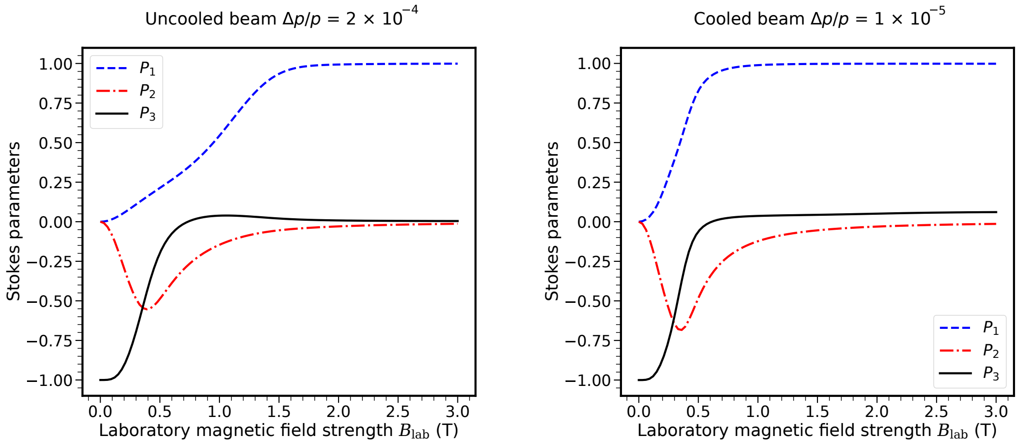

Figure 3.19: The three Stokes parameters $P_i^{(f)}$ of photons scattered in the direction of the ion beam propagation, $\theta_f^{(\mathrm{lab})} = \phi_f^{(\mathrm{lab})} = 0$, as a function of the laboratory magnetic field strength. Calculations were performed for the scattering via the $1s^2\ {}^1S_0 \rightarrow 1s2p\ {}^1P_1$ transition in a He-like Ca ion and for circularly polarized incoming light and a Lorentz factor of the ion beam of $\gamma_L = 2395$. Figure taken from Ref. [Ric5]

requires a dedicated scan of the ion beam energy. For each γ_L step in this scan, the beam optics along the entire storage ring would need to be adjusted. The results of this work show that this demanding procedure can be simplified by introducing a magnet to the collision zone in the GF setup. In particular, we observed that the Stark splitting of the $\left|{}^1P_1, M_\nu = 0\right\rangle$ and $\left|{}^1P_1, M_\nu = \pm 1\right\rangle$ sublevels is clearly resolved, see Fig. 3.16, and for $B_{\mathrm{lab}} = 3\,\mathrm{T}$ about two times larger than the uncertainty in γ_L. Consequently, the initial γ_L value can be chosen in between the resonances for the $\left|{}^1P_1, M_\nu = 0\right\rangle$ and $\left|{}^1P_1, M_\nu = \pm 1\right\rangle$ sublevels. Afterwards, the laboratory magnetic field strength can be reduced, such that the Stark splitting is reduced and the $\left|{}^1P_1, M_\nu = \pm 1\right\rangle$ sublevel is shifted into resonance. This replacement of the variation of γ_L with a scan over B_{lab} provides an easier method to find the resonance peak. In this case, only the correction magnets close to the collision zone, which account for the perturbation of the beam trajectory due to B_{lab}, need to be adjusted.

Ion beam cooling

Besides the simplified resonance condition tuning, the variation of B_{lab} can also be used for ion beam cooling. The idea of laser beam cooling is to excite only the fastest ions and consequently reduce their velocity and the longitudinal velocity spread of the ion beam [262–264]. This can be achieved by tuning γ_L just below the resonance condition, such that only the fastest ions are in resonance and get excited. Afterwards, γ_L can be increased step by step to excite also slower ions. As above, this variation of γ_L can be replaced by a scan over B_{lab}. Again, the initial value of γ_L can be set between the resonances of the $\left|{}^1P_1, M_\nu = 0\right\rangle$ and $\left|{}^1P_1, M_\nu = \pm 1\right\rangle$ sublevels for $B_{\text{lab}} = 3\,\text{T}$, such that only the fastest ions are excited to the $\left|{}^1P_1, M_\nu = \pm 1\right\rangle$ sublevels. Then B_{lab} can be decreased to excite also slower ions. However, we have to note that this cooling procedure would be slower by a factor of two, since in this case the cooling proceeds only via the $\left|{}^1P_1, M_\nu = \pm 1\right\rangle$ sublevels, which contribute about $50\,\%$ to the scattering, see Fig. 3.16.

Moreover, the small Zeeman splitting of the $\left|{}^1P_1, M_\nu = +1\right\rangle$ and $\left|{}^1P_1, M_\nu = -1\right\rangle$ sublevels can be used as a criterion to estimate the achieved degree of beam cooling. As seen from Fig. 3.16, the Zeeman splitting can not be resolved for the uncooled beam scenario and only becomes visible for a reduced momentum spread.

Polarization control

Finally, we turn to the polarization of the outgoing γ-ray photons. As different applications of the generated γ-rays demand different polarization states, precise and flexible control of photon polarization is essential for the GF project. For example, the production of longitudinally polarized lepton beams relies on circularly polarized photons, while linearly polarized light is particularly relevant for studies of Delbrück scattering or vacuum birefringence [220, 250]. As shown in Fig. 3.19, in the field-free case and with circularly polarized incident radiation, the backscattered photons ($\theta_f = \phi_f = 0$) also remain circularly polarized. When the laboratory magnetic field strength increases, the degree of linear polarization of the outgoing photons is enhanced and even complete linear polarization can be achieved. Consequently, the laboratory magnetic field provides an effective tool to adapt the photon polarization to different experimental scenarios.

4

CONCLUSION AND OUTLOOK

In this thesis, we investigated a wide range of HCI physics and their importance across multiple fields such as atomic, nuclear, plasma and particle physics. In our studies, we explored methods to improve the understanding of the structure and dynamics of HCIs themselves and demonstrated their use as a tool for studying fundamental physics, especially in the search for physics beyond the Standard Model. In particular, we investigated experimental scenarios across different energy regimes, ranging from isotope-shift spectroscopy of optical transitions to the interaction of x-ray photons with HCIs confined in EBITs and the spectroscopy of HCIs stored in the LHC.

In the first part, we reviewed the basic theory of isotope shifts in atoms and ions, including the two leading-order contributions, the first-order mass and field shift, as well as additional contributions like nuclear polarization, nuclear deformation or a new boson coupling to electrons and neutrons. Moreover, we provided an overview of the King plot analysis and its generalized forms to extract constraints on new physics from experimental isotope shift data. Using these methods, we analyzed new isotope shift data in singly charged and highly charged calcium.

In the second part, we turned to higher transition energies and focused on the interaction of HCIs with x-ray photons. In this context, we reviewed the theory of resonant photon scattering on atoms and ions, with special emphasis on the influence of external electric and magnetic fields. First, we investigated how an external magnetic field can be used to determine lifetimes of excited states in He-like and Li-like ions through the Hanle effect. Afterwards, we explored the impact of combined external electric and magnetic fields on the scattering process within the framework of the Gamma Factory project.

In the following, we provide a more detailed summary of the most important results of the different parts and discuss additional considerations for future work.

King plot analysis

In Section 2, we analyzed newly measured isotope shift data of the ν_{729}: ${}^2S_{1/2} \rightarrow {}^2D_{5/2}$ transition in Ca^{+} and the ν_{570}: ${}^3P_0 \rightarrow {}^3P_1$ transition in Ca^{14+}, combined with new measurements of nuclear mass ratios for the even calcium isotopes with $40 \leq A \leq 48$. As a result of these new precise measurements, we found a King nonlinearity of approximately $10^3\sigma$. Using the decomposition plot analysis, we showed that this observed nonlinearity cannot solely be attributed to the existence of a new boson. Indeed, the decomposition plot revealed that the nonlinearity is compatible with the most dominant Standard Model contributions, which are in this case the second-order mass shift and nuclear polarization. We accounted for the second-order mass shift by subtracting its theoretical prediction from the experimental data and eliminated one additional nonlinear term by including existing data of the ν_{DD}: ${}^2D_{3/2} \rightarrow {}^2D_{5/2}$ transition in Ca^+ within a generalized King plot analysis. Through this procedure, we reduced the residual nonlinearity significance to approximately 0.6σ. Therefore, we were able to set constraints on a new boson coupling to electrons and neutrons, resulting in the most stringent King-plot-based bounds to date for most of the considered mass range. The bounds from the most recent King plot analysis in ytterbium remain stronger for boson masses between 10^3 and 10^4 keV.

Future studies may further improve the bounds on new physics and help to deepen the understanding of the nuclear polarization effect. The current constraints are limited mainly by the experimental uncertainty in the ν_{DD} transition as well as by the theoretical uncertainty of the second-order mass shift coefficients $K_i^{(2)}$ in Ca^+. A reduction of these uncertainties in future work could lead to an improvement of the bounds on α_{NP}. To quantify this improvement, we calculated $\sigma\left[\alpha_{\mathrm{NP}}\right]$ for a reduced experimental uncertainty of $\sigma\left[\nu_{DD}\right] = 0.1\,\mathrm{Hz}$ and a relative uncertainty in the $K_i^{(2)}$ of 10%. Moreover, we assume that the generalized King plot after the subtraction of the second-order mass shift stays linear, $V_{\mathrm{exp}}/\sigma\left[V_{\mathrm{exp}}\right] \leq 1$, such that we can set the central value as $|\alpha_{\mathrm{NP}}| = \sigma\left[\alpha_{\mathrm{NP}}\right]$. The resulting 2σ-bounds are depicted by the red dashed line in Fig. 4.1. This figure shows that such an improvement could generate bounds, which are stronger than the constraints from $(g-2)_e$ and neutron scattering in the mass range $10^3 \leq m_\phi \leq 10^5$. Moreover, the reduced uncertainty in the ν_{DD} transition could allow to resolve King nonlinearities in a minimal King plot combined with either the ν_{729} or the ν_{570} transition. In this case, we could place an additional precise data point in the decomposition plot, which could help to understand the residual nonlinearity. In particular, if the mass shift corrected points would lie on a common line through the origin of the decomposition plot, it would be a hint that the nuclear polarization shift is dominated by a single factorizable nonlinear term.

Further advancements would be possible with additional isotope shift data in more transitions and isotope pairs. There is ongoing process of isotope shift measurements of the transitions in neutral Ca, which, however, has not yet reached competative precision [274, 275]. Moreover, multiple suitable transitions in different highly charged calcium ions have been proposed in Ref. [152]. Precise isotope shift data in additional transitions would allow for a more sophisticated decomposition analysis to find nuclear dependencies of the nonlinear terms, as it was demonstrated in the

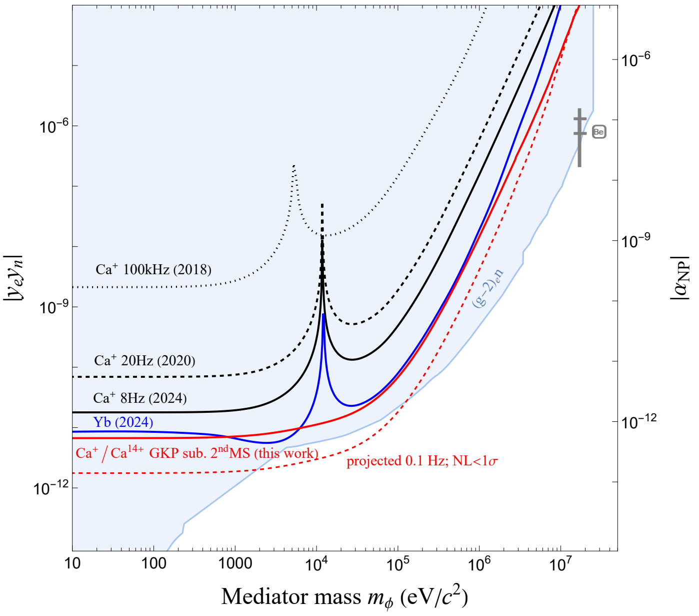

Figure 4.1: Additional to the bounds shown in Fig. 2.11 the red dashed line shows a projection of future King-plot based bounds with improved experimental and theoretical uncertainty. These bounds are calculated for a reduced experimental uncertainty of the ν_{DD} transition of 0.1 Hz and a theoretical uncertainty of the $K_i^{(2)}$ coefficients in Ca$^+$ of 10%. Moreover, we assumed that there is no significant nonlinearity, $V_{\mathrm{exp}}/\sigma\,[V_{\mathrm{exp}}] \leq 1$. If however the reduction of the uncertainty leads to the resolution of additional nonlinearities, the resulting constraints will be weaker. Figure adapted from Ref. [Ric4]

isotope shift studies with ytterbium. Even if more precise calculations of nuclear polarization are not possible from first principles, such a decomposition analysis might help to gain an empirical understanding of this effect. If, in addition, measurements are performed in more isotopes, one could perform higher dimensional generalized King plot analyses to account for more nonlinear terms. Since measurements in odd isotope pairs might introduce additional nonlinearities due to the second-order hyperfine shift [187], heavy unstable even isotopes might be more promising, which are however experimentally challenging because of short lifetimes. In fact, even without the measurement of an additional transition, data in one more calcium isotope would enable us to account for the second-order mass shift without any theory input. In this case, we can combine the generalized King plot and the nuclear-input King plot and write

$$\tilde{\boldsymbol{\nu}}_{\mathbf{3}} = K_{321} + F_{321}\tilde{\boldsymbol{\nu}}_{\mathbf{1}} + G_{321}\tilde{\boldsymbol{\nu}}_{\mathbf{2}} + K^{(2)}_{321}\tilde{\boldsymbol{\delta}}^{\mathbf{(2)}}_{\boldsymbol{M}} + \alpha_{\mathrm{NP}} X_{321}\tilde{\boldsymbol{\gamma}}\,. \tag{4.1}$$

Having data for three transitions in five isotope pairs, we solve for α_{NP} and obtain

$$\alpha_{\mathrm{NP}} = \frac{\det\left(\tilde{\boldsymbol{\nu}}_1, \tilde{\boldsymbol{\nu}}_2, \tilde{\boldsymbol{\nu}}_3, \tilde{\boldsymbol{\delta}}^{(\mathbf{2})}_{\boldsymbol{M}}, \mathbf{1}\right)}{\frac{1}{2}\varepsilon_{i_1,i_2,i_3} \det\left(X_{i_1}\tilde{\gamma}, \tilde{\boldsymbol{\nu}}_{\boldsymbol{i_2}}, \tilde{\boldsymbol{\nu}}_{\boldsymbol{i_3}}, \tilde{\boldsymbol{\delta}}^{(\mathbf{2})}_{\boldsymbol{M}}, \mathbf{1}\right)} \tag{4.2}$$

This allows us to account for the second-order mass shift and one additional nonlinear term solely through the use of experimental data.

Another promising development is the “kifit” code, introduced in Ref. [Ric6], which presents a first step towards a global analysis of isotope shift data across different elements. Such systematic, simultaneous analysis of isotope shift data in different elements might become a powerful tool once more precise measurements are available. Experiments in other elements with at least four stable even isotopes have been performed, for example, in Zn [276], Sn [277], Ba [278] and Cd [279], although the precision is not yet sufficient for Standard Model tests [Ric6].

Hanle effect for lifetime determination

In Section 3.4, we explored the use of the Hanle effect to extract lifetimes of excited states in HCIs. In particular, we performed calculations of resonant photon scattering by ions exposed to the static magnetic field of an EBIT. Our calculations of the angular distribution of emitted photons agree with experimental results for the scattering via excited $^1P_1$ states in He-like N ions, allowing the extraction of lifetimes of the excited states. Moreover, we analyzed the prospects of this method for Li-like ions. While it is not applicable for the scattering via excited $^2P_{1/2}$ states, it can be used to extract lifetimes of $^2P_{3/2}$ states. In particular, the magnetic field of the PolarX-EBIT would allow measurements of the $1s^2 3p\ ^2P_{3/2}$ states in Li-like ions with $9 \leq Z \leq 16$.

Some aspects were not included in our present treatment, which should be considered in future work depending on the experimental setup and precision. First, the scattering approach discussed in this thesis assumes light intensities, where spontaneous decay occurs faster than the absorption of photons. Performing similar experiments with high-intensity light sources might introduce additional effects [226]. Second, hyperfine structure effects were not taken into account and might have an influence on the angular distribution. Although the theoretical predictions for He-like N match the experimental data at the current precision, such effects might be important for future improvements or other systems. Finally, in our analysis of scattering via $^2P_{3/2}$ states in Li-like ions, we considered only the electric dipole transition channel. This was justified by the expected smallness of the additional magnetic quadrupole contribution, given that our goal was only to estimate a suitable Z range for future lifetime measurements. Nevertheless, depending on the desired experimental precision, magnetic quadrupole effects should be included in subsequent work.

External fields in the Gamma Factory setup

Finally, we explored resonant photon scattering in the framework of the Gamma Factory project, which offers a wide range of applications for fundamental physics, as outlined in Section 3.5. In particular, we considered a setup in which a dipole magnet is placed in the collision zone of the laser photons and the HCI beam, which leads to strong combined electric and magnetic fields in the ion rest frame. We found that these external fields can have significant effects on the cross section, the angular distribution, and the polarization of the scattered photons. The resulting Stark splitting offers a potential simplification of the resonant condition tuning and beam cooling schemes. Moreover, the external fields can be used for flexible polarization control of the emitted radiation.

Future work should address additional experimental aspects. For instance, the present analysis did not account for the spectral width of the incident laser radiation. Moreover, small deviations from the idealized field geometry, as well as field inhomogeneities, could also produce additional effects and should be examined in more detail. Furthermore, while we have shown that the magnetic field can be used to control the polarization of the outgoing beam, characterizing the full polarization of the resulting γ-rays requires integration over a small solid angle in the laboratory frame. This is straightforward for circular polarization but more involved for linear polarization, and could be addressed in future studies.

The inclusion of external fields in the Gamma Factory setup is particularly relevant for experiments probing fundamental symmetries, such as searches for atomic parity violation. Prospects for parity violation experiments with H-like and Li-like ions using the Stark interference method have already been investigated in Ref. [Ric1]. These studies could be extended to other ionic species. Since interpreting atomic parity violation measurements requires precise atomic theory input, experiments with HCIs are especially promising due to their comparatively simple electronic structure. In addition, the tunability of the photon energy at the Gamma Factory over a wide range would allow experiments with multiple ions along the same isoelectronic sequence. Such Z-scaling studies could provide valuable insight and may help in probing possible additional long-range parity-violating potentials, as discussed in Refs. [280, 281]. In this context, highly excited states may also be of particular interest as in such states, the usual parity-violating effects from Z-boson exchange between the nucleus and bound electrons are strongly suppressed, while long-range contributions might still have a significant effect.

ACKNOWLEDGEMENTS

There are many people who helped me during my years as a PhD student. First of all, I want to express how grateful I am to have had two incredible supervisors: Elina Fuchs and Andrey Surzhykov. They gave me the opportunity to be part of two different groups and to learn a lot about both atomic and particle physics, which was often challenging but equally rewarding. Their guidance helped me tremendously, and they were always available whenever I faced a problem.

I also want to thank Dmitry Budker, who kindly agreed to be a referee for this thesis. In fact, he was already involved in my Master's project, which resulted in my very first publication, and I hope to have the chance for more collaborations in the future. Moreover, I am very grateful to Ernst Maria Rasel, who agreed on short notice to take the role of head of my PhD committee.

During these years, I was involved in many fruitful collaborations, making it impossible to acknowledge everyone who contributed here. Therefore, I will only name my main collaborators for each project which were Agnese Mariotti for the King plot analysis, Moto Togawa, who performed the Hanle experiment in He-like N, and Mieczyslaw Witold Krasny, who provided valuable input regarding the Gamma Factory.

I am extremely happy to have been part of two groups, at LUH and PTB, both full of incredibly kind people. In particular, I would like to mention Agnese and Marco, my PhD siblings. Our first meeting at CERN was an unforgettable experience, especially as I lost all faith in probability theory because of you... I am also very thankful to Agnese, since fighting with indices was much more bearable together. I want to thank all the members of the FPM for making everyday work life so enjoyable and for the many memorable moments we shared at various conferences or group activities. I also owe thanks to Sophia for reading parts of this thesis and, above all, for her mental support during the last weeks before submission.

Moreover, I am grateful to have a family I can always rely on. Finally, I want to thank the Achtgroschenbande and the Braunschweig Badgers for reminding me that sometimes it is important not to think about work.

PUBLICATIONS BY THE AUTHOR

- [Ric1] J. Richter, A. V. Maiorova, A. V. Viatkina, D. Budker, and A. Surzhykov, *Parity-Violation Studies with Partially Stripped Ions* Annalen der Physik **534**, 2100561 (2022)
- [Ric2] M. Togawa, J. Richter, C. Shah, Chintan M. Botz, J. Nenninger, J. Danisch, J. Goes, S. Kühn, P. Amaro, A. Mohamed, Y. Amano, S. Orlando, R. Totani, M. de Simone, S. Fritzsche, T. Pfeifer, M. Coreno, A. Surzhykov, and J. R. Crespo López-Urrutia, **Hanle Effect for Lifetime Determinations in the Soft X-Ray Regime** Physical Review Letters **133**, 163202 (2024)
- [Ric3] J. Richter, M. Togawa, J. R. Crespo López-Urrutia, and A. Surzhykov **Hanle effect for lifetime analysis: Li-like ions** Journal of Instrumentation **20**, C03003 (2025)
- [Ric4] A. Wilzewski, L. I. Huber, M. Door, J. Richter, A. Mariotti, L. J. Spieß, M. Wehrheim, S. Chen, S. A. King, P. Micke, M. Filzinger, M. R. Steinel, N. Huntemann, E. Benkler, P. O. Schmidt, J. Flannery, R. Matt, M. Stadler, R. Oswald, F. Schmid, D. Kienzler, J. Home, D. P. L. Aude Craik, S. Eliseev, P. Filianin, J. Herkenhoff, K. Kromer, K. Blaum, V. A. Yerokhin, I. A. Valuev, N. S. Oreshkina, C. Lyu, S. Banerjee, C. H. Keitel, Z. Harman, J. C. Berengut, A. Viatkina, J. Gilles, A. Surzhykov, M. K. Rosner, J. R. Crespo López-Urrutia, and E. Fuchs, **Nonlinear calcium King plot constrains new bosons and nuclear properties** Physical Review Letters **134**, 233002 (2025)
- [Ric5] J. Richter, M. W. Krasny, J. Gilles, and A. Surzhykov, **Resonant photon scattering in the presence of external fields and its applications for the Gamma Factory** Physical Review A **111**, 062820 (2025)
- [Ric6] E. Fuchs, F. Kirk, A. Mariotti, J. Richter, and M. Robbiati, **Towards a Global Search for New Physics with Isotope Shifts** arXiv:2506.07303 [physics.atom-ph] (2025)

All publications that constitute results, which are presented in this thesis, have titles written in **bold face**.

Author contributions

The experimental work in Ref. [Ric4], was mainly performed by A. Wilzewski, L. I. Huber and M. Door and does not present a result of this thesis. Similarly, the calculations of the electronic coefficients of the second-order mass shift and the nuclear polarization do not present results of this thesis. The mass shift calculations were performed by V. A. Yerokhin and A. Surzhykov and the nuclear polarization calculations by I. A. Valuev and N. S. Oreshkina. The contributions for this thesis are the calculation and analysis of the electronic new physics coefficients, the analysis of the mass dependence, the decomposition analysis as well as the generalized King plot analysis including the subtraction of the second-order mass shift. These investigations have been performed in collaboration with A. Mariotti. The exclusion plots of Ref. [Ric4], which are shown in a modified version in this thesis, were originally produced by A. Mariotti.

The contributions from Ref. [Ric6] for this thesis are the overview of the different King plot methods, from a collaboration with A. Mariotti and F. Kirk, as well as the development of the nuclear-input King plot. The development of the global King plot fit “kifit”, which is presented in Ref. [Ric6], is not a result of this thesis.

The experimental work as well as the extraction of lifetimes through the fit to experimental data of Ref. [Ric2] was mainly performed by M. Togawa and does not present a result of this thesis. The Figures 3.10 and 3.11 from Ref. [Ric2] were originally created by M. Togawa. The contribution from Refs. [Ric2] and [Ric3], is the theoretical analysis of the influence of the external magnetic field on the angular distribution in He-like and Li-like ions.

All theoretical analysis from Ref. [Ric5] presents a result of this thesis, except for the estimation of the quadratic Zeeman shift, which has been performed by J. Gilles.

BIBLIOGRAPHY

[1] M. G. Kozlov, M. S. Safronova, J. R. Crespo López-Urrutia and P. O. Schmidt, *Highly charged ions: Optical clocks and applications in fundamental physics* Reviews of Modern Physics **90**, 045005 (2018)

[2] W. Grotian, *Zur Frage der Deutung der Linien im Spektrum der Sonnenkorona* Naturwissenschaften **27**, 214 (1939).

[3] B. Edlén, *Die Deutung der Emissionslinien im Spektrum der Sonnenkorona*, Zeitschrift für Astrophysik **22**, 30 (1943)

[4] J. D. Gillaspy, *Higly charged ions*, Journal of Physics B: Atomic, Molecular and Optical Physics **34**, R93 (2001)

[5] S. A. King, L. J. Spieß, P. Micke et al., *An optical atomic clock based on a highly charged ion*, Nature **611**, 43–47 (2022)

[6] O. O. Versolato, *Physics of laser-driven tin plasma sources of EUV radiation for nanolithography*, Plasma Sources Science and Technology **28**, 083001 (2019)

[7] Y. Ralchenko, I. N. Draganić, D. Osin et al., *Spectroscopy of diagnostically important magnetic-dipole lines in highly charged* $3d^n$ *ions of tungsten*, Physical Review A **83**, 032517 (2011)

[8] J. Rzadkiewicz, Y. Yang, K. Kozioł et al., *High-resolution tungsten spectroscopy relevant to the diagnostic of high-temperature tokamak plasmas*, Physical Review A **97**, 052501 (2018)

[9] J. Morgner, B. Tu, C. M. König et al., *Stringent test of QED with hydrogen-like tin*, Nature **622**, 53-57 (2023)

[10] M. S. Safronova, V. A. Dzuba, V. V. Flambaum et al., *Highly Charged Ions for Atomic Clocks, Quantum Information, and Search for* α *variation*, Physical Review Letters **113**, 030801 (2014)

[11] M. W. Krasny, *The gamma factory proposal for CERN*, arXiv:1511.07794 [hep-ex]

[12] D. Budker, J. R. Crespo López-Urrutia, A. Derevianko et al., *Atomic Physics Studies at the Gamma Factory at CERN*, Annalen der Physik **532**, 2000204 (2020)

[13] D. Budker, J. C. Berengut, V. V. Flambaum et al., *Expanding Nuclear Physics Horizons with the Gamma Factory*, Annalen der Physik **534**, 2100284 (2022)

[14] R. Balkin, M. W. Krasny, T. Ma et al., *Probing Axion-Like-Particles at the CERN Gamma Factory* Annalen der Physik **534**, 2100222 (2022)

[15] S. Chakraborti, J. L. Feng, J. K. Koga and M. Valli, *Gamma factory searches for extremely weakly interacting particles*, Physical Review D **104**, 055023 (2021)

[16] F. B. S. Paerels and S. M. Kahn, *High-Resolution X-Ray Spectroscopy with Chandra and XMM-Newton* Annual Review of Astronomy and Astrophysics **41**, 291-342 (2003)

[17] M. Hirsch, N. Hell, V. Grinberg et al., *Chandra X-ray spectroscopy of the focused wind in the Cygnus X-1 system - III. Dipping in the low/hard state*, Astronomy & Astrophysics **626**, A64 (2019)

[18] M. T. Tashiro, *XRISM: X-ray imaging and spectroscopy mission* International Journal of Modern Physics D **31**, 02 (2022)

[19] K. Blaum, S. Eliseev and S. Sturm, *Perspectives on testing fundamental physics with highly charged ions in Penning traps*, Quantum Science and Technology **6**, 014002 (2021)

[20] A. J. Gonzáles Martínez, J. R. Crespo López-Urrutia, D. Fischer et al., *The Heidelberg EBIT: Present Results and Future Perspectives* Journal of Physics: Conference Series **72**, 012001 (2007)

[21] P. Micke, S. Kühn, L. Buchauer et al., *The Heidelberg compact electron beam ion traps*, Review of Scientific Instruments **89**, 063109 (2018)

[22] S. Sturm, I. Arapoglou, A. Egl et al., *the ALPHATRAP experiment*, European Physical Journal Special Topics **227**, 1425-1491 (2019)

[23] M. Schwarz, O. O. Versolato, A. Windberger et al., *Cryogenic linear Paul trap for cold highly charged ion experiments*, Review of Scientific Instruments **83**, 083115 (2012)

[24] G. Werth, *The g-factor of the bound electron as a test of quantum electrodynamics* Physica Scripta **89**, 098004 (2014)

[25] J. Morgner, B. Tu, M. Moretti et al., *g Factor of Boronlike Tin*, Physical Review Letters **134**, 123201 (2025)

[26] R. Loetzsch, H. F. Beyer, L. Duval et al., *Testing quantum electrodynamics in extreme fields using helium-like uranium*, Nature **625**, 673-678 (2024)

[27] Z. Sun, I. A. Valuev and N. S. Oreshkina, *Nuclear deformation effects in the spectra of highly charged ions*, Physical Review Research **6**, 023327 (2024)

[28] C. Brandau, C. Kozhuharov, Z. Harman et al., *Isotope Shift in the Dielectronic Recombination of Three-Electron* $^{A}\mathrm{Nd}^{57+}$, Physical Review Letters **100**, 073201 (2008)

[29] V. A. Yerokhin and V. M. Shabaev, *Lamb Shift of* $n = 1$ *and* $n = 2$ *States of Hydrogen-like Atoms,* $1 \leq Z \leq 110$, Journal of Physical and Chemical Reference Data **44**, 033103 (2015)

[30] W. Decking, S. Abeghyan, P. Abramian et al., *A MHz-repetition-rate hard X-ray free electron laser driven by a superconducting linear accelerator*, Nature Photonics **14**, 391-397 (2020)

[31] C. G. Schroer, H.-C. Wille, O. H. Wille et al., *The synchrotron radiation source PETRA III and its future ultra-low-emittance upgrade PETRA IV*, European Physical Journal Plus **137**, 1312 (2022)

[32] J. C. Berengut, V. A. Dzuba, V. V. Flambaum and A. Ong, *Highly charged ions with* $E1$*,* $M1$*, and* $E2$ *transitions within laser range*, Physical Review A **86**, 022517 (2012)

[33] C. Lyu, C. H. Keitel and Z. Harman, *Periodic table of highly charged ions*, arXiv:2504.11237 [physics.atom-ph]

[34] C. Lyu, C. H. Keitel and Z. Harman, *Ultrastable and ultra-accurate clock transition in open-shell highly charged ions*, Communications Physics **8**, 3 (2025)

[35] A. Kramida, Y. Ralchenko, J. Reader and NIST ASD Team, NIST Atomic Spectra Database (ver. 5.12) (2024), [Online, 2025, September 2]

[36] ATLAS Collaboration, G. Aad, T. Abajyan, B. Abbott et al., *Observation of a new particle in the search for the Standard Model Higgs boson with the ATLAS detector at the LHC*, Physics Letters B **716**, 1, 1-29 (2012)

[37] CMS Collaboration, S. Chatrchyan, V. Khachatryan, A. M. Sirunyan et al., *Observation of a new boson at a mass of 125 GeV with the CMS experiment at the LHC*, Physics Letters B **716**, 1, 30-61 (2012)

[38] M. D. Schwartz, *Qunatum Field Theory and the Standard Model*, Cambridge University Press (2014)

[39] F. Quevedo and A. Schachner, *Cambridge Lectures on The Standard Model*, arXiv:2409.09211 [hep-th] (2024)

[40] L. Álvarez-Gaumé and M. Á. Vázquez-Mozo, *Lectures on Field Theory and the Standard Model: A Symmetry-Oriented Approach*, arXiv:2306.08097 [hep-th] (2023)

[41] D. Tong, *The Standard Model* Lecture Notes, University of Cambridge, `https://www.damtp.cam.ac.uk/user/tong/standardmodel.html`

[42] B. Grinstein, *TASI-2013 Lectures on Flavor Physics*, arXiv:1501.05283 [hep-ph] (2015)

[43] Y. Grossman, P. Tanedo, *Just a Taste: Lectures on Flavor Physics*, arXiv:1711.03624 [hep-ph] (2017)

[44] A. Kostelecky, *The Status of CPT*, arXiv:hep-ph/9810365 (1998)

[45] R. Lehnert, *CPT Symmetry and Its Violation*, Symmetry **8**, 11, 114 (2016)

[46] X. Fan, T. G. Myers, B. A. D. Sukra and G. Gabrielse, *Measurement of the Electron Magnetic Moment*, Physical Review Letters **130**, 071801 (2023)

[47] A. Hook, *New Solutions to the Gauge Hierarchy Problem* Annual Review of Nuclear and Particle Science **73**, 23-39 (2023)

[48] M. E. Peskin, *What is the Hierarchy Problem*, arXiv:2505.00694 [hep-ph]

[49] M. Pospelov and A. Ritz, *Theta vacua, QCD sum rules, and the neutron electric dipole moment*, Nuclear Physics B **573**, 177-200 (2000)

[50] S. Dar, *The Neutron EDM in the SM: A Review*, arXiv:hep-ph/0008248

[51] K.-F. Liu, *Lattice QCD and the Neutron Electric Dipole Moment*, arXiv:2411.15198 [hep-lat]

[52] F. Zwicky, *Die Rotverschiebung von extragalaktischen Nebeln*, Helvetica Physica Acta **6**, 110–127 (1933)

[53] V. C. Rubin and W. K. Ford Jr., *Rotation of the Andromeda Nebula from a Spectroscopic Survey of Emission Regions*, The Astrophysical Journal **159**, 379 (1970)

[54] S. Vegetti, S. Birrer, G. Despali, C. D. Fassnacht, D. Gilman, Y. Hezaveh, L. Perreault Levasseur, J. P. McKean, D. M. Powell, C. M. O'Riordan and G. Vernardos, *Strong Gravitational Lensing as a Probe of Dark Matter*, Space Science Reviews **220**, 58 (2024)

[55] A. J. Shajib, G. Vernardos, T. E. Collett, V. Motta, D. Sluse, L. L. R. Williams, P. Saha, S. Birrer, C. Spiniello and T. Treu, *Strong Lensing by Galaxies*, Space Science Reviews **220**, 87 (2024)

[56] T. Treu and L. V. E. Koopmans, *Massive Dark Matter Halos and Evolution of Early-Type Galaxies to $z \approx 1$*, The Astrophysical Journal **611**, 739 (2004)

[57] D. Clowe, M. Bradač, A. H. Gonzales, M. Markevitch, S. W. Randall, C. Jones and D. Zaritsky, *A Direct Empirical Proof of the Existence of Dark Matter*, The Astrophysical Journal **648** L109 (2006)

[58] M. Kamionkowski and A. Kosowsky, *The Cosmic Microwave Background and Particle Physics*, Annual Review of Nuclear and Particle Science **49**, 77-123 (1999)

[59] C. M. O'Riordan, L. J. Oldham, A. Nersesian et al., *Euclid: A complete Einstein ring in NGC 6505*, Astronomy & Astrophysics **694**, A145 (2025)

[60] A. D. Sakharov, *Violation of CP invariance, C asymmetry, and baryon asymmetry of the universe* Soviet Physics Uspekhi **34**, 392 (1991)

[61] A. Riotto and M. Trodden, *Recent Progress in Baryogenesis* Annual Review of Nuclear and Particle Science **49**, 35-75 (1999)

[62] M. Dine and M. Kusenko, *Origin of the matter-antimatter asymmetry* Reviews of Modern Physics **76**, 1 (2003)

[63] L. Canetti, M. Drewes and M. Shaposhnikov, *Matter and antimatter in the universe*, New Journal of Physics **14**, 095012 (2012)

[64] Y. Gouttenoire, *Beyond the Standard Model Cocktail*, arXiv:2207.01633 [hep-ph] (2022)

[65] R. Davis, D. S. Harmer and K. C. Hoffman, *Search for Neutrinos from the Sun* Physical Review Letters **20**, 1205 (1968)

[66] Super-Kamiokande Collaboration, S. Fukuda et al., *Solar* ^{8}B *and hep Neutrino Measurements from 1258 Days of Super-Kamiokande Data*, Physical Review Letters **86**, 5651 (2001)

[67] SNO Collaboration, Q. R. Ahmad et al., *Measuremnts of the Rate of* $\nu_e + d \to p + p + e^-$ *Interactions Produced by* ^{8}B *Solar Neutrinos at the Sudbury Neutrino Observatory*, Physical Review Letters **87**, 071301 (2001)

[68] SNO Collaboration, Q. R. Ahmad et al., *Direct Evidence for Neutrino Flavor Transformation from Neutral-Current Interactions in the Sudbury Neutrino Observatory* Physical Review Letters **89**, 011301 (2002)

[69] A. Y. Smirnov, *Neutrino mass and New physics*, Journal of Physics: Conference Series **53**, 44 (2006)

[70] E. Kh. Akhmedov, G. C. Branco and M. N. Rebelo, *Seesaw mechanism and structure of neutrino mass matrix*, Physics Letters B **478**, 1-3, 215-223 (2000)

[71] T. Lin, *TASI lectures on dark matter models and direct detection* arXiv:1904.07915 [hep-ph]

[72] R. D. Peccei and H. R. Quinn, *CP Conservation in the Presence of Pseudoparticles*, Physical Review Letters **38**, 1440 (1977)

[73] S. Weinberg, *A New Light Boson?*, Physical Review Letters **40**, 223 (1978)

[74] F. Wilczek, *Problem of Strong and Invariance in the Presence of Instantons*, Physical Review Letters **40**, 279 (1978)

[75] R. D. Peccei, *The Strong CP Problem and Axions*, arXiv:hep-ph/0607268

[76] P. W. Graham, D. E. Kaplan and S. Rajendran, *Cosmological Relaxation of the Electroweak Scale*, Physical Review Letters **115**, 221801 (2015)

[77] N. Fonseca and E. Morgante *Relaxion Dark Matter*, Physical Review D **100**, 055010 (2019)

[78] A. Banerjee, H. Kim and G. Perez, *Coherent relaxion dark matter*, Physical Review D **100**, 115026 (2019)

[79] A. Chatrchyan and G. Servant, *Relaxion dark matter from stochastic misalignment*, Journal of Cosmology and Astroparticle Physics **06**, 036 (2023)

[80] S. Knapen, T. Lin and K. M. Zurek, *Light dark matter: Models and constraints* Physical Review D **96**, 115021 (2017)

[81] J. Heeck, *Unbroken B–L symmetry*, Physics Letters B **739**, 256-262 (2014)

[82] N. Okada and S. Okada, Z'_{BL} *portal dark matter and LHC Run-2 results*, Physical Review D **93**, 075003 (2016)

[83] J. Alexander, M. Battaglieri, B. Echenard et al., *Dark Sectors 2016 Workshop: Community Report*, arXiv:1608.08632 [hep-ph] (2016)

[84] M. Battaglieri, A. Belloni, A. Chou et al., *US Cosmic Visions: New Ideas in Dark Matter 2017: Community Report*, arXiv:1707.04591 [hep-ph] (2017)

[85] G. Lanfranchi, M. Pospelov and P. Schuster, *The Search for Feebly Interacting Particles*, Annual Review of Nuclear and Particle Science **71**, 279-313 (2021)

[86] M. Fabbrichesi, E. Gabrielli and G. Lanfranchi, *The Dark Photon*, arXiv:2005.01515 [hep-ph] (2020)

[87] M. S. Safronova, D. Budker, D. DeMille, D. F. J. Kimball, A. Derevianko and C. W. Clark, *Search for new physics with atoms and molecules*, Reviews of Modern Physics **90**, 025008 (2018)

[88] T. D. Lee and C. N. Yang, *Question of Parity Conservation in Weak Interactions*, Physical Review **104**, 254 (1956)

[89] C. S. Wu, E. Ambler, R. W. Hayward, D. D. Hoppes and R. P. Hudson, *Experimental Test of Parity Conservation in Beta Decay* Physical Review **105**, 1413 (1957)

[90] Y. B. Zeld'ovich, *Parity Nonconservation in the First Order in the Weak-Interaction Constant in Electron Scattering and Other Effects*, Journal of Experimental and Theoretical Physics **9**, 3, 682 (1959)

[91] L. M. Barkov, M. S. Zolotorev, *Parity violation in atomic bismuth*, Physics Letters B **85**, 2-3, 308-313 (1979)

[92] P. H. Bucksbaum, E. D. Commins and L. R. Hunter, *Observations of parity nonconservation in atomic thallium*, Physical Review D **24**, 1134 (1981)

[93] N. H. Edwards, S. J. Phipp, P. E. G. Baird and S. Nakayama, *Precise Measurement of Parity Nonconserving Optical Rotation in Atomic Thallium*, Physical Review Letters **74**, 2654 (1995)

[94] T. P. Emmons, J. M. Reeves and E. N. Fortson, *Parity-Nonconserving Optical Rotation in Atomic Lead* Physical Review Letters **51**, 2089 (1983)

[95] M. A. Bouchiat, J. Guena, L. Hunter and L. Pottier, *Observation of a parity violation in cesium*, Physics Letters B **117**, 5, 358-364 (1982)

[96] C. S. Wood, S. C. Bennett, D. Cho, B. P. Masterson, J. L. Roberts, C. E. Tanner and C. E. Wieman, *Measurement of Parity Nonconservation and an Anapole Moment in Cesium*, Science **275**, 5307, 1759-1763 (1997)

[97] D. Antypas, A. Fabricant, J. E. Stalnaker, K. Tsigutkin, V. V. Flambaum and D. Budker, *Isotopic variation of parity violation in atomic ytterbium*, Nature Physics **15**, 120-123 (2019)

[98] G. Gwinner and L. A. Orozco, *Studies of the weak interaction in atomic systems: towards measurements of atomic parity non-conservation in francium*, Quantum Science and Technology **7**, 024001 (2022)

[99] N. Fortson, *Possibility of measuring parity nonconservation with a single trapped atomic ion*, Physical Review Letters **70**, 2383 (1993)

[100] O. O. Versolato, L. W. Wansbeek, G. S. Giri et al., *Atomic parity violation in a single trapped radium ion*, Hyperfine Interactions **199**, 9-19 (2011)

[101] D. P. L. Aude Craik, *An entanglement protocol to measure atomic parity violation at sub* 0.1% *precision*, arXiv:2503.20003 [quant-ph]

[102] N. Leefer, L. Bougas, D. Antypas and D. Budker, *Towards a new measurement of parity violation in dysprosium*, arXiv:1412.1245 [physics.atom-ph]

[103] R. Berger and J. Stohner, *Parity violation*, WIREs Computational Molecular Science **9**, e1396 (2019)

[104] F. Wauters, A. Knecht on behalf of the muX collaboration, *The muX project*, SciPost Physics Proceedings **5**, 022 (2021)

[105] S. Kanda, *A search for atomic parity violation in muonic atoms using a high-intensity pulsed muon beam at J-PARC*, EPJ Web of Conferences **262**, 01010 (2022)

[106] M. Zolotorev and D. Budker, *Parity Nonconservation in Relativistic Hydrogenic Ions*, Physical Review Letters **78**, 25 (1997)

[107] L. Labzowsky and A. Prozorov, *Parity Nonconservation Effects in the Highly Charged Ions*, Journal of Physics: Conference Series **72**, 012010 (2007)

[108] L. N. Labzowsky, A. V. Nefiodov, G. Plunien et al., *Parity-violation effect in heliumlike gadolinium and europium*, Physical Review A **63**, 054105 (2001)

[109] A. J. Vargas, *Overview of the Phenomenology of Lorentz and CPT Violation in Atomic Systems*, Symmetry **11**, 12, 1433 (2019)

[110] L. Nowak, C. Malbrunot, M. C. Simon et al., *CPT and Lorentz symmetry tests with hydrogen using a novel in-beam hyperfine spectroscopy method applicable to antihydrogen experiments*, Physics Letters B **858**, 139012 (2024)

[111] R. Aaij, C. Abellán Beteta, B. Adeva et al., *Search for Violations of Lorentz Invariance and CPT Symmetry in* $B^0_{(s)}$ *Mixing*, Physical Review Letters **116**, 241601 (2016)

[112] T. E. Chupp, P. Fierlinger, M. J. Ramsey-Musolf and J. T. Singh, *Electric dipole moments of atoms, molecules, nulcei, and particles*, Reviews of Modern Physics **91**, 015001 (2019)

[113] ACME Collaboration, *Improved limit on the electric dipole moment of the electron*, Nature **562**, 355–360 (2018)

[114] W. B. Cairncross, D. N. Gresh, M. Grau†et al., *Precision Measurement of the Electron's Electric Dipole Moment Using Trapped Molecular Ions*, Physical Review Letters **119**, 153001 (2017)

[115] T. S. Roussy, L. Caldwell, T. Wright et al., *An improved bound on the electron's electric dipole moment*, Science **381**, 6653, 46-50 (2023)

[116] R. F. Garcia Ruiz, R. Berger, J. Billowes et al., *Spectroscopy of short-lived radioactive molecules*, Nature **581**, 396–400 (2020)

[117] A. Bondarevskaya, A. Prozorov, L. Labzowsky et al., *Theory of the polrization of highly charged ions in storage rings: Production, preservation, observation and application to the search for violation of the fundamental symmetries* Physics Reports **507**, 1-42 (2011)

[118] J. L. Ouellet, C. P. Salemi, J. W. Foster et al., *First Results from ABRACADABRA-10 cm: A search for Sub-μeV Axion Dark Matter*, Physical Review Letters **122**, 121802 (2019

[119] C. P. Salemi, J. W. Foster, J. L. Ouellet et al., Physical Review Letters **127**, 081801 (2021)

[120] L. Zhong, S. Al Kenany, K. M. Backes et al., *Results from phase 1 of the HAYSTAC microwave cavity axion experiment*, Physical Review D **97**, 092001 (2018)

[121] M. J. Jewell, A. F. Leder, K. M. Backes et al., *New results from HAYSTAC's phase II operation with a squeezed state receiver* Physical Review D **107**, 072007 (2023)

[122] J. Redondo and A. Ringwald, *Light shining through walls*, Contemporary Physics **52**, 3, 211–236 (2011)

[123] D. Salnikov, P. Satunin, M. Fitkevich et al., *Light-Shining-Through-Wall Cavity Setups for Probing Axion-Like Particles*, JETP Letters **117**, 889–897 (2023)

[124] P. W. Graham and S. Rajendran, *New observables for direct detection of axion dark matter*, Physical Review D **88**, 035023 (2013)

[125] D. Budker, P. W. Graham, M. Ledbetter et al., *Proposal for a Cosmic Axion Spin Precession Experiment (CASPEr)*, Physical Review X **4**, 021030 (2014)

[126] T. Wu, J. W. Blanchard, G. P. Centers et al., *Search for Axionlike Dark Matter with a Liquid-State Nuclear Spin Comagnetometer*, Physical Review Letters **122**, 191302 (2019)

[127] A. Garcon, J. W. Blanchard, G. P. Centers et al., *Constraints on bosonic dark matter from ultralow-field nuclear magnetic resonance*, Science Advances **5**, eaax4539 (2019)

[128] D. Aybas, J. Adam, E. Blumenthal et al., *Search for Axionlike Dark Matter Using Solid-State Nuclear Magnetic Resonance*, Physical Review Letters **126**, 141802 (2021)

[129] A. Aeppli, K. Kim, W. Warfield et al., *Clock with* 8×10^{19} *Systematic Uncertainty*, Physical Review Letters **133**, 023401 (2024)

[130] M. S. Safronova, *The Search for Variation of Fundamental Constants with Clocks*, Annalen der Physik **531**, 1800364 (2019)

[131] N. Huntemann, B. Lipphardt, C. Tamm et al., *Improved Limit on a Temporal Variation of* m_p/m_e *from Comparisons of* Yb^+ *and* Cs *Atomic Clocks*, Physical Review Letters **113**, 210802 (2014)

[132] M. Filzinger, A. R. Caddell, D. Jani et al., *Ultralight Dark Matter Search with Space-Time Separated Atomic Clocks and Cavities*, Physical Review Letters **134**, 031001 (2025)

[133] J. Tiedau, M. V. Okhapkin, K. Zhang et al., *Laser Excitation of the* Th-*229 Nucleus*, Physical Review Letters **132**, 182501 (2024)

[134] R. Elwell, C. Schneider, J. Jeet et al., *Laser Excitation of the* ^{229}Th *Nuclear Isomeric Transition in a Solid-State Host*, Physical Review Letters **133**, 013201 (2024)

[135] T. Ooi, J. F. Doyle, C. Zhang et al., *Frequency reproducibility of solid-state* Th-*229 nuclear clocks*, arXiv:2507.01180 [physics.atom-ph] (2025)

[136] C. Zhang, T. Ooi, J. S. Higgins et al., *Frequency ratio of the* ^{229m}Th *nuclear isomeric transition and the* ^{87}Sr *atomic clock*, Nature **633**, 63–70 (2024)

[137] V. A. Dzuba, V. V. Flambaum and E. Peik, *Nuclear clock based on the* Th *V ion*, Physical Review A **112**, 023103 (2025)

[138] I. Angeli and K. P. Marinova *Table of experimental nuclear ground state charge radii: An update* Atomic Data and Nuclear Data Tables **99**, 69-95 (2013)

[139] R. Silwal, A. Lapierre, J. D. Gillaspy et al., *Measuring the difference in nuclear charge radius of* Xe *isotopes by EUV spectroscopy of highly charged* Na-*like ions*, Physical Review A **98**, 052502 (2018)

[140] G. W. F. Drake, W. Nörtershäuser and Z.-C. Yan, *Isotope shifts and nuclear radius measurements for helium and lithium*, Canadian Journal of Physics **83**, 4 (2005)

[141] K. Heilig and A. Steudel, *Changes in mean-square nuclear charge radii from optical isotope shifts*, Atomic Data and Nuclear Data Tables **14**, 5-6, 613-638 (1974)

[142] C. Delaunay, R. Ozeri, G. Perez, et al., *Probing Atomic Higgs-like Forces at the Precision Frontier* Physical Review D **96**, 093001 (2017)

[143] J. C. Berengut, D. Budker, C. Delaunay et al., *Probing New Long-Range Interactions by Isotope Shift Spectroscopy*, Physical Review Letters **120**, 091801 (2018)

[144] F. W. Knollmann, A. N. Patel and S. Charles Doret, *Part-per-billion measurement of the $4^2S_{1/2} \rightarrow 3\ ^2D_{5/2}$ electric quadrupole transition isotope shifts between* $^{42,44,48}\mathrm{Ca}^+$ *and* $^{40}\mathrm{Ca}^+$, Physical Review A **100**, 022514 (2019)

[145] C. Solaro, S. Meyer, K. Fisher et al., *Improved isotope-shift-based bounds on bosons beyond the Standard Model through measurements of the $^2D_{3/2}{}^2D5/2$ interval in* Ca^+, Physical Review Letters **125**, 123003 (2020)

[146] T. T. Chang, B. B. Awazi, J. C. Berengut et al., *Systematic-free limit on new light scalar bosons via isotope-shift spectroscopy in* Ca^+, Physical Review A **110**, L030801 (2024)

[147] N. L. Figueroa, J. C. Berengut, V. A. Dzuba, et al., *Precision Determination of Isotope Shifts in Ytterbium and Implications for New Physics*, Physical Review Letters **128**, 073001 (2022)

[148] I. Counts, J. Hur, D. P. L. Aude Craik, et al., *Evidence for Nonlinear Isotope Shift in* Yb^+ *Search for New Boson*, Physical Review Letters **125**, 123002 (2020)

[149] J. Hur, D. P. L. Aude Craik, I. Counts et al., *Evidence of Two-Source King Plot Nonlinearity in Spectroscopic Search for New Boson*, Physical Review Letters **128**, 163201 (2022)

[150] M. Door, C.-H. Yeh, M. Heinz et al., *Probing New Bosons and Nuclear Structure with Ytterbium Isotope Shifts*, Physical Review Letters **134**, 063002 (2025)

[151] K. Ono, Y. Saito, T. Ishiyama et al., *Observation of Nonlinearity of Generalized King Plot in the Search for New Boson*, Physical Review X **12**, 021033 (2012)

[152] N.-H. Rehbehn, M. K. Rosner, H. Bekker et al., *Sensitivity to new physics of isotope-shift studies using the coronal lines of highly charged calcium ions*, Physical Review A **103**, L040801 (2021)

[153] J. C. Berengut and C. Delaunay, *Precision isotope-shift spectroscopy for new physics searches and nuclear insights*, Nature Reviews Physics **7**, 119–125 (2025)

[154] K. Pachucki, V. Patkóš and V. A. Yerokhin, *Testing fundamental interactions on the helium atom*, Physical Review A **95**, 062510 (2017)

[155] V. A. Yerokhin, K. Pachucki and V. Patkóš *Theory of the Lamb Shift in Hydrogen and Light Hydrogen-Like Ions*, Annalen der Physik **531**, 1800324 (2019)

[156] C. Frugiuele, E. Fuchs, G. Perez and M. Schlaffer, *Constraining new physics models with isotope shift spectroscopy*, Physical Review D **96**, 015011 (2017)

[157] A. J. Krasznahorkay, M. Csatlós, L. Csige et al., *Observation of Anomalous Internal Pair Creation in* ^{8}Be*: A Possible Indication of a Light, Neutral Boson*, Physical Review Letters **116**, 042501 (2016)

[158] J. L. Feng, B. Fornal, I. Galon et al., *Protophobic Fifth-Force Interpretation of the Observed Anomaly in Nuclear Transitions*, Physical Review Letters **117**, 071803 (2016)

[159] J. L. Feng, B. Fornal, I. Galon et al., *Particle physics models for the 17 MeV anomaly in beryllium nuclear decays*, Physical Review D **95**, 035017 (2017)

[160] A. J. Krasznahorkay, M. Csatlós, L. Csige et al., *New anomaly observed in* ^{4}He *supports the existence of the hypothetical X17 particle*, Physical Review C **104**, 044003 (2021)

[161] A. J. Krasznahorkay, A. Krasznahorkay, M. Begala et al., *New anomaly observed in* ^{12}C *supports the existence and the vector character of the hypothetical X17 boson*, Physical Review C **106**, L061601 (2022)

[162] The MEG II collaboration: K. Afanaciev, A. M. Baldini, S. Ban et al., *Search for the X17 particle in* $^7\mathrm{Li}(p, e^+ e)^8\mathrm{Be}$ *processes with the MEG II detector*, arXiv:2411.07994 [nucl-ex] (2024)

[163] F. Bossi, R. De Sangro, C. Di Giulio et al., *Search for a new 17 MeV resonance via* $e^+ e$ *annihilation with the PADME Experiment*, arXiv:2505.24797 [hep-ex] (2025)

[164] A. V. Viatkina, V. A. Yerokhin and A. Surzhykov, *Calculation of isotope shifts and King-plot nonlinearities in* Ca^+, Physical Review A **108**, 022802 (2023)

[165] I. I. Tupitsyn, V. M. Shabaev, J. R. Crespo López-Urrutia et al., *Relativistic calculations of isotope shifts in highly charged ions*, Physical Review A **68**, 022511 (2003)

[166] W. R. Johnson, *Atomic Structure Theory - Lectures on Atomic Physics* Springer Science & Business Media (2007)

[167] B. H. Bransden and C. J. Joachain, *Physics of Atoms and Molecules*, Longman Scientific Technical (1983)

[168] H. A. Bethe and E. E. Salpeter, *Quantum Mechanics of One- and Two-Electron Atoms*, Academic Press (1957)

[169] R. D. Cowan, *The Theory of Atomic Structure and Spectra*, University of California Press (1981)

[170] A. M. Frolov and D. M. Wardlaw, *Accurate evaluations of the field shift and lowest-order QED correction for the ground 1^1S-states of some light two-electron ions* Journal of Chemical Physics **141**, 104318 (2014)

[171] C. W. P. Palmer, *Reformulation of the theory of the mass shift*, Journal of Physics B: Atomic, Molecular and Optical Physics **20**, 5987–5996 (1987)

[172] V. M. Shabaev, *QED theory of the nuclear recoil effect in atoms*, Physical Review A **57**, 59 (1998)

[173] F. A. Parpia and A. K. Mohanty, *Relativistic basis-set calculations for atoms with Fermi nuclei*, Physical Review A **46**, 3735 (1992)

[174] E. Lindroth and A.-M. Mårtensson-Pendrill *Calculation of isotope shift in Na*, Zeitschrift für Physik A **309**, 277-284 (1983)

[175] M. S. Safronova and W. R. Johnson, *Third-order isotope-shift constants for alkali-metal atoms and ions*, Physical Review A **64**, 052501 (2001)

[176] V. A. Yerokhin, R. A. Müller, A. Surzhykov et al., *Nonlinear isotope-shift effetcs in* Be-*like,* B-*like, and* C-*like argon*, Physical Review A **101**, 012502 (2020)

[177] Z. Sun, I. A. Valuev and N. S. Oreshkina, *Nuclear deformation effects in the spectra of highly charged ions*, Physical Review Research **6**, 023327 (2024)

[178] J. Zatorski1, N. S. Oreshkina, C. H. Keitel and Z. Harman, *Nuclear Shape Effect on the g Factor of Hydrogenlike Ions*, Physical Review Letters **108**, 063005 (2012)

[179] Y. S. Kozhedub, O. V. Andreev, V. M. Shabaev et al., *Nuclear deformation effect on the binding energies in heavy ions*, Physical Review A **77**, 032501 (2008)

[180] S. O. Allehabi, V. A. Dzuba, V. V. Flambaum and A. V. Afanasjev, *Nuclear deformation as a source of the nonlinearity of the King plot in the* Yb^+ *ion*, Physical Review A **103**, L030801 (2021)

[181] A. Haga, Y. Horikawa and Y. Tanaka, *Nuclear polarization in hydrogenlike* ${}^{208}_{82}\mathrm{Pb}^{81+}$, Physical Review A **65**, 052509(2002)

[182] A. Haga, Y. Horikawa and Y. Tanaka, *Nuclear polarization in muonic* ${}^{208}\mathrm{Pb}$ Physical Review A **66**, 034501 (2002)

[183] B. Hoffmann, G. Baur and J. Speth, *Effects of nuclear polarizability on isotope shifts in electronic atoms*, Zeitschrift für Physik A **315**, 57-63 (1984)

[184] L. N. Labzowsky, A. N. Nefiodov, G. Plunien et al., *Vacuum polarization - nuclear polarization corrections to the Lamb shift in heavy atoms*, Journal of Physics B: Atomic, Molecular and Optical Physics **29**, 3841 (1996)

[185] I. A. Valuev and N. S. Oreshkina, *Full leading-order nuclear polarization in highly charged ions*, Physical Review A **109**, 042811 (2024)

[186] H. Miyake, N. C. Pisenti, P. K. Elgee et al., *Isotope-shift spectroscopy of the* ${}^1S_0 \to {}^3P_1$ *and* ${}^1S_0 \to {}^3P_0$ *transition in strontium*, Physical Review Research **1**, 033113 (2019)

[187] J. C. Berengut and N. S. Oreshkina, *Second-order hyperfine structure and its impact on new physics searches using isotope shift spectroscopy*, arXiv:2409.01530 [physics.atom-ph] (2025)

[188] M. E. Peskin and D. V. Schroeder *An Introduction to Quantum Field Theory*, Westview Press (1995)

[189] W. H. King, *Comments on the Article "Peculiarities of the Isotope Shift in the Samarium Spectrum"* , Journal of the Optical Society of America **53**, 638-639 (1963)

[190] J. C. Berengut, C. Delaunay, A. Geddes and Y. Soreq, *Generalized King linearity and new physics searches with isotope shifts*, Physical Review Research **2**, 043444 (2020)

[191] F. Gebert, Y. Wan, F. Wolf et al., *Precision Isotope Shift Measurements in Calcium Ions Using Quantum Logic Detection Schemes*, Physical Review Letters **115**, 053003 (2015)

[192] C. Delaunay, C. Frugiuele, E. Fuchs, and Y. Soreq, *Probing new spin-independent interactions through precision spectroscopy in atoms with few electrons*, Physical Review D **96**, 115002 (2017)

[193] R. M. Potvliege, *Spectroscopy of light atoms and bounds on physics beyond the standard model*, New Journal of Physics **27**, 045002 (2025)

[194] H. Leeb and J. Schmiedmayer *Constraint on hypothetical light interacting bosons from low-energy neutron experiments*, Physical Review Letters **68**, 1472 (1992)

[195] Y. N. Pokotilovski, *Constraints on new interactions from neutron scattering experiments*, Physics of Atomic Nuclei **69**, 924–931 (2006)

[196] V. V. Nesvizhevsky, G. Pignol and K. V. Protasov, *Neutron scattering and extra-short-range interactions*, Physical Review D **77**, 034020 (2008)

[197] G. Raffelt, *Limits on a CP-violating scalar axion-nucleon interaction* Physical Review D **86**, 015001 (2012)

[198] J. A. Grifols and E. Massó, *Constraints on finite-range baryonic and leptonic forces from stellar evolution*, Physics Letters B **173**, 237 (1986)

[199] C. A. J. O'Hare and E. Vitagliano, *Cornering the axion with CP-violating interactions*, Physical Review D **102**, 115026 (2020)

[200] M. Bordag, U. Mohideen and V. M. Mostepanenko, *New developments in the Casimir effect*, Physics Reports **353**, 1 (2001)

[201] M. Bordag, G. L. Klimchitskaya, U. Mohideen and V. M. Mostepanenko, *Advances in the Casimir Effect*, International Series of Monographs on Physics **145** (2009)

[202] J. Sugar and C. Corliss, *Atomic Energy Levels of the Iron-Period Elements: Potassium through Nickel*, Journal of Physical and Chemical Reference Data **14**, Suppl. 2, 1–664 (1985)

[203] E. V. Kahl and J. C. Berengut, *AMBiT: A programme for high-precision relativistic atomic structure calculations*, Computer Physics Communications **238**, 232-243 (2019)

[204] V. A. Dzuba, V. V. Flambaum and M. G. Kozlov, *Combination of the many-body perturbation theory with the configuration-interaction method*, Physical Review A **54**, 3948 (1996)

[205] M. G. Kozlov, S. G. Porsev, M. S. Safronova and I. I. Tupitsyn, *CI-MBPT: A package of programs for relativistic atomic calculations based on a method combining configuration interaction and many-body perturbation theory* Computer Physics Communications **195**, 199-213 (2015)

[206] J. C. Berengut, *Particle-hole configuration interaction and many-body perturbation theory: Application to* Hg$^+$*.*, Physical Review A **94**, 012502 (2016)

[207] H. Bachau, E. Cormier, P. Decleva et al., *Applications of B-splines in atomic and molecular physics*, Reports on Progress in Physics **64**, 1815 (2001)

[208] V. M. Shabaev, I. I. Tupitsyn, V. A. Yerokhin et al., *Dual Kinetic Balance Approach to Basis-Set Expansions for the Dirac Equation*, Physical Review Letters **93**, 130405 (2004)

[209] M. Wang, W. J. Huang, F. G. Kondev et al., *The AME 2020 atomic mass evaluation (II). Tables, graphs and references*, Chinese Physics C **45**, 030003 (2021)

[210] P. Kane, L. Kissel, R. Pratt, and S. Roy, *Elastic scattering of γ-rays and x-rays by atoms*, Physics Reports **140**, 2, 75—159 (1986)

[211] S. Strnat, V. A. Yerokhin, A. V. Volotka et al., *Polarization studies on Rayleigh scattering of hard x rays by closed-shell atoms*, Physical Review A **103**, 012801 (2021)

[212] S. Strnat, J. Sommerfeldt, V. Yerokhin et al., *Circular Polarimetry of Hard X-rays with Rayleigh Scattering* Atoms **10**, 4 (2022)

[213] W. Middents, G. Weber, A. Gumberidze et al., *Angle-differential cross sections for Rayleigh scattering of highly linearly polarized hard x rays on* Au *atoms*, Physical Review A **107**, 012805 (2023)

[214] P. W. Atkins and L. D. Barron, *Rayleigh scattering of polarized photons by molecules* Molecular Physics **16**, 5, 453–466 (1969)

[215] E. G. Fuller and E. Hayward, *Nuclear Elastic Scattering of Photons*, Physical Review **101**, 692 (1956)

[216] D. Drechsel, A. Russo, *Nucleon structure effects in photon scattering by nuclei*, Physics Letters B **137**, 5-6 (1984)

[217] J. Fink, E. Schierle, E. Weschke and J. Geck, *Resonant elastic soft x-ray scattering*, Reports on Progress in Physics **76**, 056502 (2013)

[218] J. Sommerfeldt, V. A. Yerokhin, R. A. Müller et al., *Calculations of Delbrück scattering to all orders in α*, Physical Review A **105**, 022804 (2022)

[219] J. Sommerfeldt, V. A. Yerokhin, Th. Stöhlker, and A. Surzhykov, *All-Order Coulomb Corrections to Delbrück Scattering above the Pair-Production Threshold* Physical Review Letters **131**, 061601 (2023)

[220] J. Sommerfeldt, S. Strnat, V. A. Yerokhin et al., *Low-energy tests of Delbrück scattering*, Physical Review A **108**, 042819 (2023)

[221] D. Samoilenko, A. V. Volotka, and S. Fritzsche, *Elastic photon scattering on hydrogenic atoms near resonances*, Atoms **8**, 2 (2020)

[222] V. G. Serbo, A. Surzhykov and A. Volotka, *Resonant scattering of plane-wave and twisted photons at the gamma factory* Annalen der Physik **534**, 2100199 (2022)

[223] A. Volotka, D. Samoilenko, S. Fritzsche et al., *Polarization of photons scattered by ultra-relativistic ion beams*, Annalen der Physik **534**, 2100252 (2022)

[224] S. Bernitt, G. V. Brown, J. K. Rudolph et al., *An unexpectedly low oscillator strength as the origin of the* Fe *XVII emission problem*, Nature **492**, 7428, 225–228 (2012)

[225] W. Hanle, *Über magnetische Beeinflussung der Polarisation der Resonanzfluoreszenz*, Zeitschrift für Physik **30**, 1, 93–105 (1924)

[226] P. Avan and C. Cohen-Tannoudji *Hanle effect for monochromatic excitation. Non perturbative calculation for a* $J = 0$ *to* $J = 1$ *transition* Journal de Physique Lettres **36**, 4, 85—88 (1975)

[227] V. M. Shabaev, *Two-time Green's function method in quantum electrodynamics of high-Z few-electron atoms*, Physics Reports **356**, 3, 119-228 (2002)

[228] O. Y. Andreev, L. N. Labzowsky, G. Plunien, D. A. Solovyev, *QED theory of the spectral line profile and its applications to atoms and ions*, Physics Reports **455**, 4-6 (2008)

[229] O. Y. Andreev, *QED theory of the spectral line profile for few-electron atoms and ions*, Journal of Physics: Conference Series **397**, 012001 (2012)

[230] A. I. Akhiezer and V. B. Berestetskii, *Quantum Electrodynamics*, John Wiley and Sons (1966)

[231] D. A. Varshalovich, A. N. Moskalev and V. K. Khersonskii, *Quantum Theory of Angular Momentum*, World Scientific (1988)

[232] K. Blum, *Density matrix theory and applications* 3rd ed. Springer series on atomic, optical, and plasma physics (2012)

[233] J. Gilles, S. Fritzsche, L. J. Spieß et al., *Quadratic Zeeman and electric quadrupole shifts in highly charged ions*, Physical Review A **110**, 052812 (2024)

[234] B. Lu, X. Lu, J. Li and H. Chang, *Theoretical calculation of the quadratic Zeeman shift coefficient of the* $^3P_0^o$ *clock state for strontium optical lattice clock*, Chinese Physics B **31**, 043101 (2022)

[235] J. R. P. Angel, P. G. H. Sandars and B. Bleaney, *The hyperfine structure Stark effect I. Theory*, Proceedings of the Royal Society of London. Series A. Mathematical and Physical Sciences **305**, 1480, 125–138 (1968)

[236] V. A. Yerokhin, S. Y. Buhmann, S. Fritzsche and A. Surzhykov, *Electric dipole polarizabilities of rydberg states of alkali-metal atoms*, Physical Review A **94**, 032503 (2016)

[237] G. Moruzzi, F. Strumia, *The Hanle Effect and Level-Crossing Spectroscopy*, Springer Science+Business, Physics of Atoms and Molecules (2013)

[238] R. W. Wood, *LXVII. Selective reflexion, scattering and absorption by resonating gas molecules*, The London, Edinburgh, and Dublin Philosophical Magazine and Journal of Science **23**, 137, 689–714 (1912)

[239] R. J. Strutt, *Polarisation of the light scattered by mercury vapour near the resonance periodicity* Proceedings of the Royal Society A **102**, 715, 190–196 (1922)

[240] R. W. Wood and A. Ellett, *On the influence of magnetic fields on the polarisation of resonance radiation*, Proceedings of the Royal Society A **103**, 722, 396–403 (1923)

[241] A. Lurio, R. L. deZafra and R. J. Goshen, *Lifetime of the First* $^1P_1$ *State of Zinc, Calcium, and Strontium*, Physical Review **134**, A1198 (1964)

[242] J. D. Feichtner, J. H. Gallagher and M. Mizushima, *Lifetime of the First Excited Atomic States of* Rb^{87}, Physical Review **164**, 44 (1967)

[243] D. Zimmermann, *Determination of the lifetime of the* $4p_{1/2}$*-state of potassium by Hanle-effect*, Zeitschrift für Physik A Atoms and Nuclei **275**, 5-10 (1975)

[244] G. W. Series, *The level-crossing effect in resonance fluorescence stimulated by monochromatic light*, Proceedings of the Physical Society **89**, 1017 (1966)

[245] H. Brand, W. Lange, J. Luther et al., *Level-crossing under nearly monochromatic excitation by a narrow-band cw dye laser*, Optics Communications **13**, 3, 286-288 (1975)

[246] J. O. Stenflo, *Hanle-Zeeman scattering matrix*, Astronomy and Astrophysics **338**, 301-310 (1998)

[247] S. W. Epp, J. R. Crespo. López-Urrutia, M. C. Simon, *X-ray laser spectroscopy of highly charged ions at FLASH*, Journal of Physics B: Atomic, Molecular and Optical Physics **43**, 194008 (2010)

[248] J. Jaeckel, M. Lamont and C. Vallée, *The quest for new physics with the Physics Beyond Colliders programme*, Nature Physics **16**, 393-401 (2020)

[249] W. Middents, G. Weber, U. Spillmann et al., *Possible Polarization Measurements in Elastic Scattering at the Gamma Factory Utilizing a 2D Sensitive Strip Detector as Dedicated Compton Polarimeter*, Annalen der Physik **534**, 2100285 (2022)

[250] F. Karbstein, *Vacuum Birefringence at the Gamma Factory*, Annalen der Physik **534**, 2100137 (2022)

[251] C. Novotny, G. Huber, S. Karpuk et al., *Sub-Doppler laser spectroscopy on relativistic beams and tests of Lorentz invariance*, Physical Review A **80**, 022107 (2009)

[252] B. Botermann, D. Bing, C. Geppert et al., *Test of Time Dilation Using Stored* Li^+ *Ions as Clocks at Relativistic Speed*, Physical Review Letters **113**, 120405 (2014)

[253] A. Apyan, M. W. Krasny, and W. Placzek, *Gamma Factory high-intensity muon and positron source: Exploratory studies*, Physical Review Accelerator and Beams **26**, 083401 (2023)

[254] M. Schaumann, R. Alemany-Fernandez, H. Bartosik et al., *First Partially Stripped Ions in the LHC (*$^{208}\mathrm{Pb}^{81+}$*)*, Proceedings of the 10th International Particle Accelerator Conference (IPAC'19), 689-692 (2019)

[255] A. Gorzawski, A. Abramov, R. Bruce et al., *Collimation of partially stripped ions in the CERN Large Hadron Collider*, Physical Review Accelerator and Beams **23**, 101002 (2020)

[256] M. W. Krasny, A. Martens and Y. Dutheil, *Gamma Factory Proof-of-Principle experiment*, HAL 02999656 (2020)

[257] H. C. Bryant, B. D. Dieterle, J. Donahue et al., *Observation of resonances near 11 eV in the photodetachment cross section of the* H *ion*, Physical Review Letters **38**, 228 (1977)

[258] P. A. M. Gram, J. C. Pratt, M. A. Yates-Williams et al., *Effect of an Electric Field upon Resonances in the* H *Ion*, Physical Review Letters **40**, 107 (1978)

[259] P. G. Harris, H. C. Bryant, A. H. Mohagheghi et al., *Observation of doubly excited resonances in the* H *ion*, Physical Review A **42**, 6443 (1990)

[260] M. Halka, P. G. Harris, A. H. Mohagheghi et al., *Electric-field effects on* H *photodetachment partial cross sections above 13.4 eV*, Physical Review A **48**, 419 (1993)

[261] J. Eichler and W. Meyerhof, *Relativistic Atomic Collisions* Academic, New York, (1995)

[262] L. Eidam, O. Boine-Frankenheim and D. Winters, *Cooling rates and intensity limitations for laser-cooled ions at relativistic energies*, Nuclear Instruments and Methods in Physics Research Section A: Accelerators, Spectrometers, Detectors and Associated Equipment **887**, 102-113 (2018)

[263] M. W. Krasny, A. Petrenko and W. Płaczek, *High-luminosity Large Hadron Collider with laser-cooled isoscalar ion beams*, Progress in Particle and Nuclear Physics **114**, 103792 (2020)

[264] P. Kruyt, D. Gamba and G. Franchetti, *Simulation studies of laser cooling for the Gamma Factory proof-of-principle experiment at the CERN SPS*, Proceedings of the 15th International Particle Accelerator Conference (IPAC'24), 832-835 (2024)

[265] D. Nichita, D. L. Balabanski, P. Constantin et al., *Radioactive Ion Beam Production at the Gamma Factory*, Annalen der Physik **534**, 2100207 (2022)

[266] M. Puchalski and U. D. Jentschura, *Quantum electrodynamic corrections to the g factor of helium P states*, Physical Review A **86**, 022508 (2012)

[267] M. Puchalski, K. Piszczatowski, J. Komasa et al., *Theoretical determination of the polarizability dispersion and the refractive index of helium*, Physical Review A **93**, 032515 (2016)

[268] Z.-C. Yan, *Polarizabilities of the Rydberg states of helium*, Physical Review A **62**, 052502 (2000)

[269] N. D. Bhaskar and A. Lurio, *Tensor polarizability of the* $2\,^1P_1$ *state of* He^4 *by electric-field level crossing*, Physical Review A **10**, 1685 (1974)

[270] R. P. M. J. W. Notermans and W. Vassen, *Highprecision spectroscopy of the forbidden* $2\,^3S_1 \rightarrow 2\,^1P_1$ *transition in quantum degenerate metastable helium*, Physical Review Letters **112**, 253002 (2014)

[271] R. Si, X. L. Guo, K. Wang et al., *Energy levels and transition rates for helium-like ions with Z=10–36*, Astronomy & Astrophysics **592**, A141 (2016)

[272] M. Rose, *Elementary Theory of Angular Momentum*, Structure of matter series, Wiley (1957)

[273] V. V. Balashov, A. N. Grum-Grzhimailo and N. M. Kabachnik, *Polarization and correlation phenomena in atomic collisions: a practical theory course*, Springer Science Business Media (2013)

[274] A. Kramida, *Isotope shifts in neutral and singly-ionized calcium*, Atomic Data and Nuclear Data Tables **133-134**, 101322 (2020)

[275] D. Röser, L. Möller, H. Keßler and S. Stellmer, *Isotope-shift measurement of the 423-nm transition in neutral* Ca, Physical Review A **110**, 032809 (2024)

[276] D. Röser, J. Eduardo Padilla-Castillo, B. Ohayon et al., *Hyperfine structure and isotope shifts of the* $(4s^2)\ ^1S_0 \rightarrow (4s4p)\ ^{1P_1}$ *transition in atomic zinc*, Physical Review A **109**, 012806 (2024)

[277] A. T. Goble, J. D. Silver and D. N. Stacey, *Isotope shifts in the atomic spectrum of tin:* $^{112}\mathrm{Sn}$, $^{114}\mathrm{Sn}$ *and* $^{115}\mathrm{Sn}$, Journal of Physics B: Atomic and Molecular Physics **7** 26 (1974)

[278] J. Choi, E. Lee, D. Yum et al., *Direct measurement of isotope shifts in the barium* $6s^2\ ^1S_0$ - $5d6p\ ^3D_1^o$ *transition*, Physical Review A **110**, 032812 (2024)

[279] S. Hofsäss, J.. Eduardo Padilla-Castillo, S. C.. Wright et al., *High-resolution isotope-shift spectroscopy of* Cd *I*, Physical Review Research **5**, 013043 (2023)

[280] V. A. Dzuba, V. V. Flambaum and P. Munro-Laylim, *Long-range parity-nonconserving electron-nucleon interaction*, Physical Review A **106**, 012817 (2022)

[281] K. Gaul, L. Cong and D. Budker, *Constraints on new vector boson mediated electron-nucleus interactions from spectroscopy of polar diatomic molecules*, arXiv:2503.08210 [hep-ph] (2025)

CV

Jan Richter

E-Mail: jan.richter@ptb.de

EDUCATION

PhD Student (Physics) 2022-2025

Leibniz University Hannover and PTB Braunschweig, Germany

- *Thesis:* Highly Charged Ions as a Tool for Fundamental Physics and Tests of the Standard Model
- *Supervisors:* Elina Fuchs and Andrey Surzhykov

Master of Science (Physics) 2018-2021

TU Braunschweig, Germany

- *Thesis:* Parity Nonconservation in Hydrogenlike Ions
- *Supervisor:* Andrey Surzhykov

Bachelor of Science (Physics) 2015-2019

TU Braunschweig, Germany

- *Thesis:* Drift-Bounce Resonance in Earths Magnetosphere
- *Supervisor:* Karl-Heinz Glassmeier